AD-A126 640 THREE DIMENSIONAL STRUCTURE AND TIME DEVELOPMENT OF 1/2
RADIO EMISSION FROM S..(U) TUFTS UNIV MEDFORD MA DEPT
OF PHYSICS K R LANG 15 JAN 83 AFGL-TR-83-0018
UNCLASSIFIED F19628-80-C-0090 F/G 3/2 NL

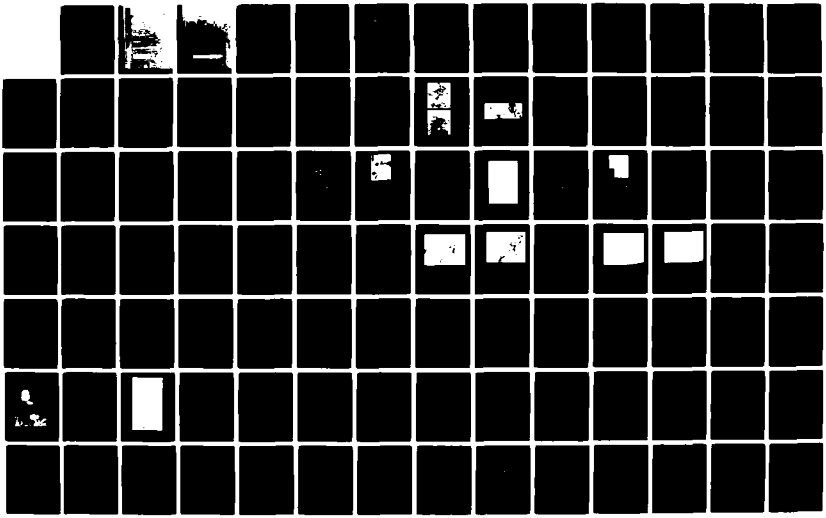

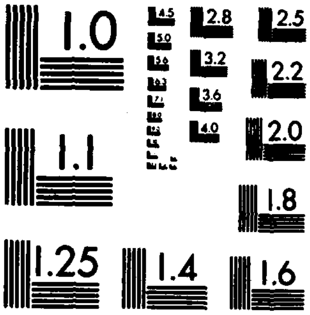

MICROCOPY RESOLUTION TEST CHART
NATIONAL BUREAU OF STANDARDS-1963-A

Unclassified
SECURITY CLASSIFICATION OF THIS PAGE (When Data Entered)

REPORT DOCUMENTATION PAGE		READ INSTRUCTIONS BEFORE COMPLETING FORM
1. REPORT NUMBER AFGL-TR-83-0018	2. GOVT ACCESSION NO. AD-A126640	3. RECIPIENT'S CATALOG NUMBER
4. TITLE (and Subtitle) THREE DIMENSIONAL STRUCTURE AND TIME DEVELOPMENT OF RADIO EMISSION FROM SOLAR ACTIVE REGIONS		5. TYPE OF REPORT & PERIOD COVERED Final Report 01 May 1980 - 31 Dec. 1982
		6. PERFORMING ORG. REPORT NUMBER
7. AUTHOR(s) Kenneth R. Lang		8. CONTRACT OR GRANT NUMBER(s) F 19628-80-C-0090
9. PERFORMING ORGANIZATION NAME AND ADDRESS Department of Physics Tufts University Medford, Massachusetts, 02155		10. PROGRAM ELEMENT, PROJECT, TASK AREA & WORK UNIT NUMBERS 62101F 2311/G3 BF
11. CONTROLLING OFFICE NAME AND ADDRESS Air Force Geophysics Laboratory Hanscom AFB, Massachusetts 01731 Contract Monitor: Edward Cliver/PHP		12. REPORT DATE 15 January 1983
		13. NUMBER OF PAGES 124
14. MONITORING AGENCY NAME & ADDRESS(if different from Controlling Office)		15. SECURITY CLASS. (of this report) Unclassified
		15a. DECLASSIFICATION/DOWNGRADING SCHEDULE
16. DISTRIBUTION STATEMENT (of this Report) Approved for public release - distribution unlimited		
17. DISTRIBUTION STATEMENT (of the abstract entered in Block 20, if different from Report)		
18. SUPPLEMENTARY NOTES		

19. KEY WORDS (Continue on reverse side if necessary and identify by block number)

Solar Radio Radiation, Active Regions, Brightness Temperature, Electron Temperature, Electron Density, Circular Polarization, Magnetic Field Strength, Bremsstrahlung, Gyroresonant Emission, Plage, Sunspot Umbrae, Penumbrae, Legs of Magnetic Dipoles, Coronal Loops, X-ray Emission, Solar Bursts, Snapshot Maps, Location of Energy Release, Burst Precursors, Preburst Heating, Magnetic Field Changes.

20. ABSTRACT (Continue on reverse side if necessary and identify by block number)

The three dimensional structure of quiescent active regions is determined by simultaneous multiple wavelength observations. Synthesis maps obtained with the Very Large Array (V.L.A.) at 2 cm, 6 cm and 20 cm wavelength are compared with Solar Maximum Mission satellite observations at X-ray and E.U.V. (extreme ultraviolet) wavelengths, Westerbork Synthesis Radio Telescope observations at 6 cm wavelength, and Hα and offband Hα observations at the Big Bear, Ottawa River and Meudon Observatories. The 6 cm radiation of solar active regions is due to plage-associated bremsstrahlung and sunspot-associated gyroemission. (Continued)

DD FORM 1 JAN 73 1473

20. (Continued)

The sunspot-associated component does not emit detectable X-ray radiation, whereas the plage-associated component does. The circularly polarized radiation at 6 cm specifies the strength and structure of the magnetic field in the low solar corona. Magnetic field strengths of $H_\ell \sim 600$ gauss and electron temperatures of $T_e \sim 10^6$ K are specified at altitudes $h \sim 4 \times 10^9$ cm above sunspot umbrae. The circularly polarized horseshoe structures which overlie sunspot penumbrae provide conclusive proof for gyroresonant absorption. The 6 cm radiation marks the legs of magnetic dipoles, whereas the 20 cm radiation delineates the ubiquitous coronal loops which have only been previously observed at X-ray wavelengths. Electron temperatures of $T_e \sim 2 \times 10^6$ K and electron densities of $N_e \sim 3 \times 10^9$ cm^{-3} are inferred for the 20 cm loops. At 2 cm wavelength small, highly polarized sources probably delineate the 10^5 K plumes seen at E.U.V. wavelengths. We also discuss V.L.A. observations of a total of fifteen solar bursts at 2 cm, 6 cm and 20 cm wavelength. The bursts were all resolved with angular sizes of $\phi = 5''$ to $30''$ and brightness temperatures of $T_e = 10^7$ K to 10^8 K. The burst energy is usually released at the apex of coronal loops. Multiple component bursts are emitted by a single small source with no detectable changes in source position or magnetic field. Snapshot maps made at 10 second intervals during solar bursts provide evidence for preburst heating and for magnetic changes before and during solar bursts.

CONTENTS

CONTENTS

ILLUSTRATIONS

ILLUSTRATIONS

TABLES

THREE DIMENSIONAL STRUCTURE AND TIME DEVELOPMENT OF RADIO EMISSION FROM SOLAR ACTIVE REGIONS

1. INTRODUCTION

Our understanding of solar active regions has been severely limited by single wavelength observations which refer to the two dimensional structure at only one height in the solar atmosphere. The large majority of solar observations have been made at optical wavelengths, for example, which refer to the thin photospheric slice of the solar atmosphere; whereas the less frequent observations at X-ray, ultraviolet and radio wavelengths are usually made at one wavelength which refers to some other height in the solar corona or transition region. Moreover, comparisons of single wavelength observations usually refer to different active regions taken at different times and these comparisons misleadingly assume that all active regions are the same, and that they do not change and evolve. In this scientific report we discuss simultaneous, multiple wavelength observations which have overcome the problems associated with previous observations at a single wavelength. We have used the Very Large Array (V.L.A.) to simultaneously observe solar active regions at two, six and twenty-one centimeters wavelength. We have also simultaneously observed the same active regions with the V.L.A. at twenty-one centimeters wavelength and with the Westerbork Synthesis Radio Telescope (W.S.R.T.) at six centimeters wavelength. Simultaneous observations at optical wavelengths were carried out at the Big Bear Solar Observatory, the Observatoire de Paris-Meudon, and the Ottawa River Solar Observatory. We have also simultaneously observed one active region

---

at E.U.V. and X-ray wavelengths using the Solar Maximum Mission satellite.

Our simultaneous, multiple wavelength observations in the radio and optical parts of the spectrum have enabled us to specify the three dimensional structure of solar active regions. Observations at any one given wavelength have been used to specify the two dimensional structure of the temperature, electron density, and magnetic field. (Longer wavelengths refer to higher levels in the solar atmosphere.) The two dimensional structures obtained at different wavelengths (or heights) have then been combined with height measurements to specify the three dimensional structure of solar active regions. In this way we have overcome the problem of comparing observations of different active regions taken at different times with different wavelengths. Moreover, by sampling at rapid time intervals of ten seconds, we have added the fourth time dimension, and thereby monitored the time development of solar active regions at a variety of heights in the solar atmosphere.

These studies of the three dimensional spatial properties and the time development of solar active regions have resolved uncertainties about the strength of the coronal magnetic field, the temperatures above sunspots, the nature of coronal loops and the radiation mechanisms in the coronal atmosphere above active regions. They have also led to a new understanding of the location of burst energy release, as well as the nature of burst precursors which manifest themselves by large increases in brightness and polarization.

In this final scientific report we present all of the published and unpublished work performed under this contract. The results are naturally divided into two main categories: the quiescent active region and solar bursts. The three dimensional structure of quiescent active regions is discussed in Section 2, while the solar bursts are discussed in Section 3. Section 2 begins with Subsection 2.1 which describes our observations of the slowly varying component of solar active regions at 6 cm wavelength. These results have been published by Lang[1] and Felli, Lang and Willson[2]. The polarized emission above sunspot penumbrae at 6 cm wavelength is presented in Subsection 2.2. This work will be (or has been) published by Lang and Willson[3,4]. Subsection 2.3 describes multiple wavelength observations of an

---

[1] Lang, K.R. (1982), Very large array observations of solar active regions, Proc. S.M.Y. Workshop - Crimean Ap. Obs. 1:39-56.

[2] Felli, M., Lang, K.R. and Willson, R.F.(1981), Very large array observations of solar active regions I. The slowly varying component, Ap. J. 247:325-337.

[3] Lang, K.R. and Willson, R.F. (1982), Polarized horseshoes around sunspots at 6 cm wavelength, Ap. J. Lett. 255:L111-L117.

[4] Lang, K.R. and Willson, R.F. (1983), Multiple wavelength observations of flaring active regions, to be published, Proc. XXIV COSPAR.

active region which has been published in a paper by Chiuderi-Drago et al.[5]. We next reproduce, in subsection 2.4, a paper which will be published by Lang, Willson and Gaizauskas[6]. This paper discusses multiple wavelength observations of solar active regions, while also introducing our discovery of the radio wavelength counterpart of the coronal loops observed at X-ray wavelengths. The 20 centimeter radio loops are discussed in greater detail in Subsection 2.5, which comes from papers by Lang, Willson and Rayrole[7] and Lang and Willson[4]. Section 3 on solar bursts begins with Subsection 3.1 describing multiple component bursts observed at 20 centimeter wavelength. These observations are described in greater detail in the paper by Lang, Willson and Felli[8]. We then end Section 3 with Subsection 3.2 which describes multiple wavelength observations of solar bursts in a paper which will be published by Willson[9].

---

[5] Chiuderi-Drago, F. et al., (1982), Multiple wavelength observations of a solar active region, Solar Phys. 80:71-85.

[6] Lang, K.R., Willson, R.F. and Gaizauskas, V. (1983), Very large array observations of solar active regions III. Multiple wavelength observations, to be published Ap. J., April 1983.

[7] Lang, K.R., Willson, R.F. and Rayrole, J. (1982), Very large array observations of coronal loops at 20 cm wavelength, Ap. J. 258:384-387.

[8] Lang, K.R., Willson, R.F. and Felli, M. (1981), Very large array observations of solar active regions II. Solar bursts, Ap. J. 247:338-347.

[9] Willson, R.F. (1983), High resolution observations of solar bursts at 2 cm, 6 cm and 20 cm wavelength, to be published, Solar Phys.

2. THREE DIMENSIONAL STRUCTURE OF RADIO EMISSION FROM SOLAR ACTIVE REGIONS

2.1 THE SLOWLY VARYING COMPONENT

2.1.1 Introduction

It has long been known that the slowly varying S component of solar radio emission, whose intensity is correlated with sunspot number and area, is connected with solar activity and has its origin in solar active regions. Early fan-beam observations with angular resolutions of a few arc-minutes, for example, led to the conclusion that the S component sources are located in the vicinity of both chromospheric plage and groups of sunspots, and because high brightness temperatures of $T_B \sim 10^6$K had been inferred for these sources, they were attributed to enhancements in the density or temperature of the coronal atmosphere overlying active regions. Waldmeier and Müller[10] and Waldmeier[11] suggested that the S component is due to coronal condensations with an abnormally high electron density of $N_e \sim 10^{10}$ cm^{-3}, while Piddington and Minnett[12] reasoned that the condensations may also be abnormally hot with electron temperatures of $T_e \sim 10^7$K. Newkirk[13] next used optical wavelength

---

[10] Waldmeier, M. and Müller, H. (1950), Die sonnenstrahlung im gebiet von λ = 10 cm, Zs. f. Ap. 27:58-72.

[11] Waldmeier, M. (1956), Analyse einer koronalen kondensation, Zs. f. Ap. 40: 221-235.

[12] Piddington, J.H. and Minnett, H.C. (1951), Solar radio-frequency emission from localized regions at very high temperatures, Austr. J. Sci. Res. A4:131-157.

[13] Newkirk, G. (1961), The solar corona in active regions and the thermal origin of the slowly varying component of solar radiation, Ap. J. 133:983-1013.

observations to derive a model for the enhanced electron density in the coronal regions above chromospheric plage and sunspot groups, and showed that this enhancement could account for the S component without modifying the coronal temperature from the value of $T_e \sim 2 \times 10^6$K which had been inferred from the Doppler broadening and the excitation of spectral lines. At this time the available data indicated that the S component was simply the thermal bremsstrahlung of the dense coronal condensations which overlie chromospheric plage or sunspot groups. A connection with intense magnetic fields had, of course, been suggested by the discovery that the radiation is circularly polarized[14], but this polarization could be easily interpreted in terms of propagation effects in which the extraordinary component of wave motion is enhanced in the presence of a magnetic field[15,16]. In fact, magnetic field strengths of $H \sim 300$ gauss could be inferred under the assumption that the thermal bremsstrahlung remains optically thin at a wavelength of about 5 cm where the circular polarization is about 30%[17]; while the low degree of circular polarization and the maximum brightness temperature of $T_B \sim 2 \times 10^6$K at the longer wavelength of $\lambda = 20$ cm could be explained by thermal bremsstrahlung which has become optically thick[18,19]. By the late 1950s, then, the centimeter-wavelength fan-beam observations of the slowly varying S component could be interpreted in terms of the bremsstrahlung of thermal electrons in dense "coronal condensations", provided that intense magnetic fields are also present, but only the larger S component sources with angular sizes of $\phi \sim 2'$-$5'$ had been resolved in only one direction, and an alternative opacity source involving the acceleration of thermal electrons by magnetic fields had been overlooked.

Stepanov[20] showed that the emission and absorption processes involving the

---

[14] Covington, A.E. (1949), Circularly polarized solar radiation at 10.7 cm, Proc. I.R.E. 37:407-410.

[15] Lehany, F.J. and Yabsley, D.E. (1949), Solar radiation at 1200 mc/s, 600 mc/s and 200 mc/s, Austr. J. Sci. Res. A2:48-62.

[16] Denisse, J.F. (1950), Contribution à l'étude des émissions radioelectriques solaires, Ann. d'Ap. 13:181-202.

[17] Gelfreikh, G., Korol'kov, D., Rishkov, N. and Soboleva, N. (1959), On the regions over sunspots as studied by polarization observations on centimeter wavelengths, Paris Symposium on Radio Astronomy, R.N. Bracewell, Ed., Stanford University Press, Stanford, pp.125-129.

[18] Christiansen, W.N. and Mathewson, D.S. (1959), The origin of the slowly varying component, Paris Symposium on Radio Astronomy, R.N. Bracewell, Ed., Stanford University Press, Stanford, pp.108-117.

[19] Christiansen, W.N. et al. (1960), A study of a solar active region using combined optical and radio techniques, Ann. d'Ap. 23:75-101.

[20] Stepanov, K.N. (1958), On the damping of electromagnetic waves in a plasma situated in a magnetic field, Soviet Phys.-JETP 8:195-196.

gyroresonant radiation of thermal electrons accelerated by magnetic fields may compete with the process involving the bremsstrahlung of thermal electrons accelerated in the electric fields of ions, and Ginzburg and Zheleznyakov[21] showed that the gyroresonant absorption of radio waves could be important in the solar corona. Zheleznyakov[22] then interpreted the slowly varying S component of solar radiation in terms of both thermal bremsstrahlung and gyroresonant radiation in a model involving gyroresonant absorption above sunspots and bremsstrahlung away from them. His core-halo model was based upon Kundu's[23,24] interferometric observations which showed that the S component sources at 3.2 centimeters contain an intense polarized core with an angular size $\phi \sim 1.8'$ surrounded by a weaker unpolarized halo whose angular extent ranges between 5' and 9'. The bright (10^6K) sunspot-associated cores, which were intepreted in terms of gyroradiation at the second and third harmonics of the gyrofrequency, were thought to play an important role in the emission of solar bursts, while the weaker (10^5K) halo emission was associated with the thermal bremsstrahlung of chromospheric plage. Additional support for this composite core-halo model with two radiation mechanisms was independently provided by Kakinuma and Swarup[25] who showed that gyroresonant absorption can explain the apparent peak in the spectrum of the S component at wavelengths $\lambda = 6$-12 cm, as well as the observed decrease in circular polarization with increasing wavelength. Detailed core-halo models involving dipole magnetic fields, thermal bremsstrahlung at $\lambda \leq 5$ cm and $\lambda \geq 15$ cm, and gyromagnetic processes at 5 cm $< \lambda <$ 15 cm were subsequently developed by Lantos[26], Zlotnik[27,28] and Zheleznyakov[29]. It soon

---

[21] Ginzburg, V.L. and Zheleznyakov, V.V. (1959), On the propagation of electromagnetic waves in the solar corona taking into account the influence of the magnetic field, Sov. Astr.-AJ 3:235-246.

[22] Zheleznyakov, V.V. (1962), The origin of the slowly varying component of solar radio emission, Sov. Astr. AJ 6:3-9.

[23] Kundu, M.R. (1959a),Structures et propriétés des sources d'activité solaire sur ondes centimètriques, Ann. d'Ap. 22:1-100.

[24] Kundu, M.R. (1959b), Étude interferometrique des sources d'activité solaire sur 3 cm de longueur d'onde, Paris Symposium on Radio Astronomy, R.N. Bracewell, Ed., Stanford University Press, Stanford, pp.222-236.

[25] Kakinuma, T. and Swarup, G. (1962), A model for the sources of slowly varying components of solar radiation, Ap. J. 136:975-994.

[26] Lantos, P. (1968), A model for thermal gyromagnetic radio emission from solar active regions, Ann. d'Ap. 31:105-113.

[27] Zlotnik, E. Ya. (1968a), Theory of the slowly changing component of solar radio emission I, Sov. Astr. AJ 12: 245-253.

[28] Zlotnik, E. Ya. (1968b), Theory of the slowly changing component of solar radio emission II, Sov. Astr. AJ 12:464-472.

[29] Zheleznyakov, V.V. (1970), Radio Emission from the Sun and Planets, Pergamon, New York.

became apparent, however, that the observations which had been used in support of these models could have led to misleading conclusions. The cores remained unresolved with only an upper limit to their angular size of ∿ 2'. This meant that the so-called cores could be composed of smaller, brighter sources which might be associated with either sunspots or bright plage. Moreover, the dilution effects of observing these smaller sources with large antenna beamwidths would produce an artificial reduction in circular polarization which is unrelated to the emission mechanism of the radiation.

By the 1970s, the development of high-resolution radio wavelength interferometers and synthesis arrays, as well as the development of space instruments which detect solar X-ray and ultraviolet emission with high spatial and spectral resolution, led to a renewed interest in the competing models for the structure of the coronal atmosphere above solar active regions. Lang[30], for example, used interferometric observations at a wavelength of $\lambda = 3.7$ cm with an effective angular resolution of 7" to show that the so-called core sources are actually composed of one or more bright sources with angular sizes $\phi \sim 20''$, brightness temperatures of $T_B \sim 10^6$K, and extraordinarily high circular polarizations of up to 100%. The presence of several bright components with angular sizes of about 20" and brightness temperatures ranging between 5×10^5 and 10^7K was confirmed by interferometric observations at 2.8 cm wavelength[31,32]. Kundu and Alissandrakis[33] next used the Westerbork Synthesis Radio Telescope (WSRT) at a wavelength of $\lambda = 6$ cm to resolve a solar active region into several discrete sources with brightness temperatures of $T_B \sim 10^6$K. They were able to show that the circular polarization of these smaller sources is as high as 90% and that maps of the circular polarization correlate well with magnetograms of the longitudinal magnetic field in the lower lying solar photosphere. Subsequent analysis of the data by Kundu et al.[34] suggested that the brightest components of the 6 cm emission are associated with sunspots. Alissandrakis, Kundu and Lantos[35] then used some of this data together with theoretical

---

[30] Lang, K.R. (1974a), High resolution interferometry of the sun at 3.7 cm wavelength, <u>Solar Phys</u>. <u>36</u>:351-367.

[31] Felli, M., Pampaloni, P. and Tofani, G. (1974), Fine structure of a very bright active region at a wavelength of 2.8 cm, <u>Solar Phys</u>. <u>37</u>:395-402.

[32] Felli, M., Tofani, G., Fürst, E. and Hirth, W. (1975), On the nature of some active regions in the microwave region, <u>Solar Phys</u>. <u>42</u>:377-390.

[33] Kundu, M.R. and Alissandrakis, C.E. (1975), Observations at 6 cm of the solar active region, <u>Nature</u> <u>257</u>:465-467.

[34] Kundu, M.R., Alissandrakis, C.E., Bregman, J.D. and Hin, A.C. (1978), Six centimeter observations of solar active regions with six arc second resolution, <u>Ap</u>. <u>J</u>. <u>213</u>:278-295.

[35] Alissandrakis, C.E. , Kundu, M.R. and Lantos, P. (1981), A model for sunspot associated emission at 6 cm wavelength, <u>Astr</u>. <u>Ap</u>. <u>82</u>:30-40.

models to show that the 6 cm emission above sunspots connot be solely due to thermal bremsstrahlung, for it would require density and/or temperature enhancements which are not observed at X-ray or E.U.V. wavelengths in the regions which overlie sunspots. Nevertheless, density enhancements are observed at X-ray wavelengths in regions which overlie the plage component of active regions, and Alissandrakis et al.[35] omitted discussion of their WSRT data which indicate that intense 6 cm emission with $T_B \sim 10^6$K is associated with chromospheric plage where no sunspots exist. In fact, the angular resolution of their radio wavelength data did not permit a definitive comparison with the bright plage and sunspots seen at Hα wavelengths, and they selected one example in which sunspot-associated radio emission appeared to support their contention that the 6 cm emission from solar active regions is predominantly due to the gyroresonant absorption process. Here we argue that the substantial part of the radio flux from active regions at 6 cm wavelength is actually due to bremsstrahlung from plage-associated sources, and that a two-component model is needed in which only the sunspot-associated component is due to gyroresonant processes. Such a two-component model has been previously suggested by Pallavicini et al.[36,37] on the basis of a comparison of 2.8 cm and X-ray observations, but the angular resolution of their radio wavelength data was barely adequate to distinguish between the plage and sunspot-associated components.

We next present V.L.A. synthesis maps of the active region AR 2032 at 6 cm wavelength and compare them with Hα photographs and magnetograms of the same region with comparable angular resolutions and second-of-arc positional accuracy. The synthesis maps given in Section 2.1.2 indicate that the radio emission is dominated by a small (∿ 30"), bright (∿ 10^6K), circularly polarized (∿ 30%) source whose morphological features are correlated with the chromospheric plage seen as bright regions on the Hα photographs. Two small (∿ 10"), bright (∿ 10^6K), circularly polarized (∿ 90%) sources which are associated with sunspots provide less than 5% of the radio wavelength flux of the active region. In Section 2.1.3 we provide a theoretical discussion in which we interpret the dominant plage-associated component at 6 cm wavelength in terms of the thermal bremsstrahlung of a hot (electron temperature $T_e \sim 2.5 \times 10^6$K), dense (emission measure ∿ 2×10^{29} cm^{-5} and electron density $N_e \sim 5 \times 10^9$ cm^{-3}) coronal condensation. The spatial configuration, emission measure, electron density, and temperature of the plage-associated component are all consistent with those inferred from X-ray observations of coronal condensations above

---

[36] Pallavicini, R., Vaiana, G.S., Tofani, G. and Felli, M. (1979), The coronal atmosphere above solar active regions: comparison of high spatial resolution soft X-ray and centimetric observations, Ap. J. 229:375-386.

[37] Pallavicini, R., Sakurai, T. and Vaiana, G.S. (1981), X-ray, e.u.v. and centimetric observations of solar active regions: an empirical model for bright radio sources, Astr. Ap. 98:316-327.

other active regions. In Section 2.1.3 we also interpret the circular polarization of the plage-associated component in terms of propagation effects in the presence of a magnetic field of strength H ∿ 250 gauss; while a similar interpretation of the higher polarization of the sunspot-associated component is used in support of an alternative gyroresonant radiation mechanism. The enhanced radio emission associated with sunspots is interpreted in terms of gyroresonant absorption processes which require unexpectedly high magnetic field strengths of H = 600-900 gauss at atmospheric levels where the temperature $\sim 10^6$K. In Section 2.1.4 we summarize our basic conclusions.

2.1.2 Observations of the Plage-Associated and Sunspot-Associated Components

We have used the Very Large Array (V.L.A.) to observe the active region AR 2032 on 1979 October 5 and 6. The position of AR 2032 on the Sun's surface was 17°N and 61°E at 13^h U.T. on October 5, and 16°N, 45°E at 13^h U.T. on October 6. The V.L.A. was divided into two subarrays to give nearly idential u-v coverage at two wavelengths $\lambda = 6$ and 20 cm, and hence identical beams. The $\lambda = 6$ cm subarray was composed of 10 antennae with distances from the array center ranging between 0.04 and 5.72 km. The $\lambda = 20$ cm subarray was composed of 9 antennae with distances from the array center ranging between 0.9 and 17.2 km. The individual antennae have a diameter of 25 m which provided respective beamwidths of 9' and 29' at $\lambda = 6$ cm and 21 cm. The average correlated flux of 45 interferometer pairs at $\lambda = 6$ cm and 36 interferometer paris at $\lambda = 20$ cm was sampled every 30 s for both the left-hand circularly polarized (LCP) signal, the right-hand circularly polarized (RCP) signal, and the two crossed polarized signals. These data were then calibrated, edited, and averaged to make synthesis maps of the total intensity I = (LCP+RCP)/2, and V = (LCP-RCP)/2.

The data were calibrated by observing 3C 273 for 5 min every 30 min, and by assuming that the flux density of 3C 273 is 35.14 and 20.5 Jy, respectively, at $\lambda = 6$ cm and 20 cm. The amplitude and phase of the observed data were calibrated according to the procedure described by Lang and Willson[38] together with a correction for a difference in the temperatures of the switched noise source of each polarization channel. Solar bursts, bad antennae, and interference were then edited from the data and the edited data were then used to make synthesis maps. Using a synthesis technique to make a map of a source whose intensity, position, and shape may vary with time and even undergo violent changes during bursts requires a careful handling of the data and some explanation of what the final maps mean. Fluctuations in

---

[38] Lang, K.R. and Willson, R.F. (1979), Very large array observations of solar active regions, Nature 278:24-28.

intensity can be produced by solar bursts, as well as by changes in the orientation and size of the fan beam with respect to the presumably stationary brightness distribution of the active region. We therefore only edited the obvious intense bursts, while stopping the burst editing when the amplitude fluctuations were less than 3 times the average value in a surrounding 1 hour interval. Any smaller changes in intensity, position, and size of the active region were assumed to be averaged out in the synthesis maps. This procedure resulted in good maps at $\lambda = 6$ cm where several hours of data taken at many different baselines and hour angles were used, and the u-v coverage remained good and uniform. Because the individual antennae beamwidths at $\lambda = 20$ cm included the entire Sun, however, the 20 cm data were contaminated by five solar flares lasting up to an hour each. Because of contamination by solar flares as well as calibration and confusion problems, we were unable to obtain accurate synthesis maps at $\lambda = 20$ cm; and for this reason we present the much more definitive results obtained at $\lambda = 6$ cm. The validity of our method is confirmed by the low sidelobe levels (< 10% of peak intensity) and the absence of definite fringe patterns in our 6 cm maps, as well as by the excellent correlation of the 6 cm total intensity map with Hα photographs of the same region. Moreover, because the editing was applied to all four correlators, this process will not introduce spurious polarization effects provided that the time changes in the polarized emission of the brightness structure follow the same pattern as the changes in the unpolarized emission, which is very likely.

The calibrated amplitude and phase of the 6 cm data for each polarization and every antenna pair were taken to be the amplitude and phase of the source visibility function; and the source intensity distribution was then obtained by Fourier transforming the calibrated data and using the new CLEAN procedure on roughly 10,000 u-v components for each day of observation. Due to the low declination of the Sun, the u-v coverage was not uniform, giving rise to an elongated synthesized beam of half-power width 2" x 15" tilted at a position angle of -33°. The effects of the elongated beam are clearly shown in the synthesis maps, as are the effects of the sidelobes of the synthesized beam. For a point source, the sidelobe level is 10% of the peak intensity, while in the presence of an extended source it is slightly larger. As is later shown, the close correlation of the individual radio-wavelength morphology with the Hα photographs of the same active region indicates that most of the features are real and not due to sidelobes, but there are residual sidelobe features of low intensity which have no clear optical counterpart. Because the dynamic range of 1-10 is retained in both the total intensity and the circular polarization maps, the polarization percentages quoted in this paper refer only to the most intense structures. The spurious instrumental circular polarization at the half-power level of each antenna beam (4.5' at 6 cm) is a maximum of 15% and because all of our maps refer to sources lying within the central 2' of each beam, we conclude that our uncertainties in estimated polarization are a maximum of ±10%.

The data obtained during the daylight observing hours on October 5 and 6 were used to obtain a synthesis map of the total intensity, I, for each day (Figure 1). Here the contours mark levels of equal brightness temperature corresponding to 0.1, 0.2,...0.9 times the maximum brightness temperature $T_B(\max)$; and the major and minor axis of the synthesized beam pattern are denoted by the cross marks in the upper left-hand corner of the figure. Assuming a constant brightness temperature distribution over the synthesized beam area, Ω_B, we have $T_B(\max) = 1.95 \times 10^6$K with $\Omega_B = 27.49$ square seconds of arc on October 6. This suggests that the brightest features of the enhanced radio emission have become optically thick with a brightness temperature equal to the electron temperature in the coronal atmosphere. Broad-band observations at X-ray wavelengths, as well as the observed Doppler broadening and excitation of spectral lines at optical wavelengths, indicate that the coronal condensations above active regions have electron temperatures of $T_e = 2\text{-}4 \times 10^6$K. An optically thick condition at the points of peak intensity is additionally supported by the fact that these points do not coincide with the points of maximum circular polarization. The vast majority of the enhanced radio emission comes from optically thin regions, however, with optical depths $\tau < 1$, where $T_B/T_e = [1 - \exp(-\tau)]$. For the total intensity map on October 6, for example, the contribution to the flux from regions with brightness temperatures of $T_B = 0.625$, 1.125, 1.625, 2.125, and 2.37×10^6K are, respectively, 50, 26, 19, 4 and 1%. Thus, assuming constant T_e throughout the active region, 50% of the flux comes from regions of optical depth $\tau \leq 0.3$ and 75% comes from regions with optical depths of $\tau \lesssim 0.6$.

The synthesis maps obtained on the two days are quite different, indicating that the 6 cm emission from solar active regions can undergo significant structural changes on a time scale of 1 day. The lifetimes of the so-called coronal condensations and the bright chromospheric plage can also be measured in days, suggesting an intimate connection between these features and the radiation at centimeter wavelengths. In fact, comparisons of our total intensity maps with Hα photographs of the same regions indicate a detailed correlation between the regions of enhanced radio emission and the chromospheric plage seen as bright regions on the Hα photographs. Part of the changes from day to day may be due to the rotation of the active region across the Sun rather than to intrinsic changes in the intensity structure of the source, but this affects both the Hα and the radio wavelength maps in the same way. The comparable angular resolutions and second-of-arc positional accuracy were in part due to accurate optical wavelength measurements of the sunspot positions which were made by Dr. Neidig during simultaneous observations at the Sacramento Peak Observatory. In order to get the best match of the radio contours with the Hα plage, we found that we had to move the radio map to the west by about 20" ± 5" with respect to the projected position of the Hα

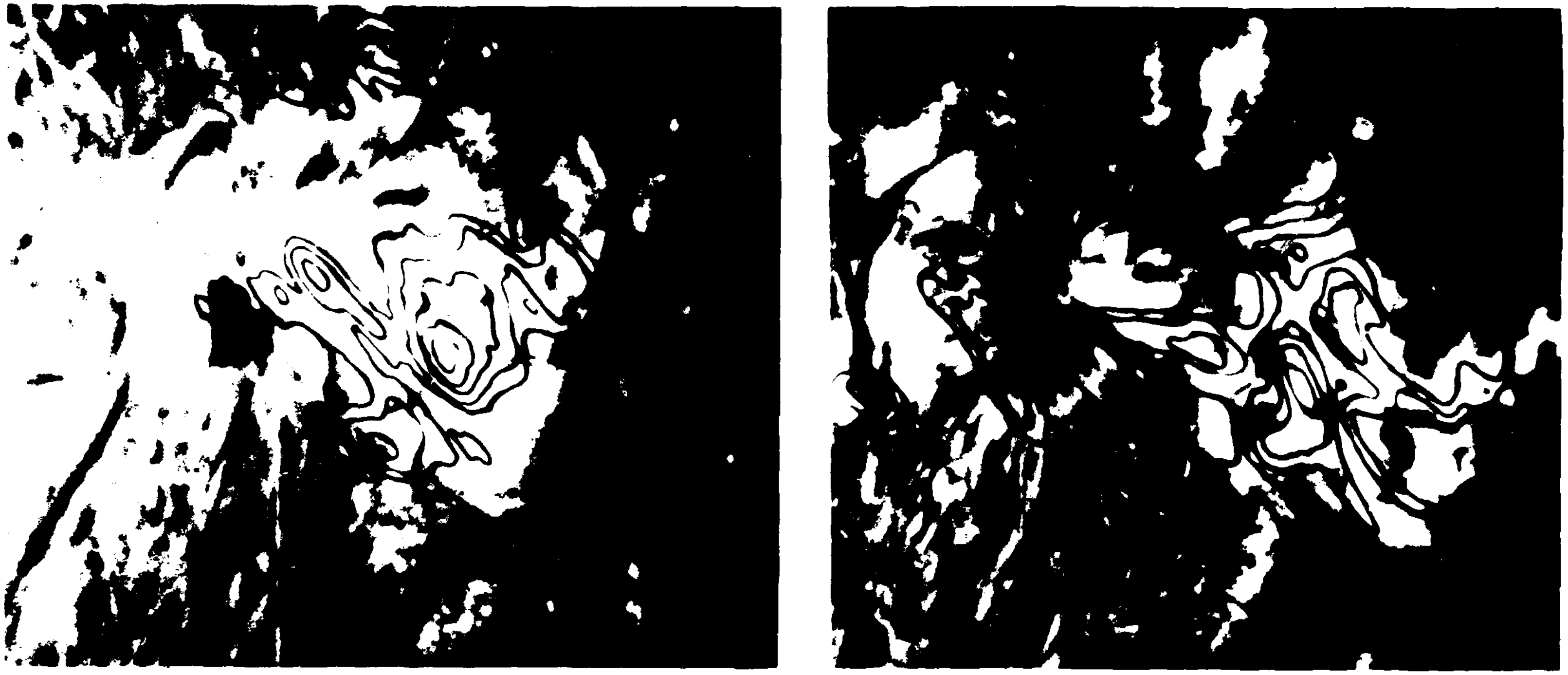

Figure 1. A comparison of V.L.A. synthesis maps of the total intensity, I, at $\lambda = 6$ cm (black contours) with Hα photographs of the same region AR 2032 taken on October 5, 1979 (left) and October 6, 1979 (right). Here North is up, and West is to the right. The black contours mark levels of equal brightness temperature corresponding to 0.2, 0.4, 0.6 and 0.8 times the maximum brightness temperature of 1.95×10^6 and 2.50×10^6 K, respectively. These comparisons illustrate the detailed correlation between the 6 cm emission and bright chromospheric plage, as well as plage-associated evolutionary changes on a time scale of one day. The large sunspot seen on October 6 also has some associated radio emission. The Hα photographs were taken at the 6563 Å Balmer line with a 10-inch evacuated refractor using S01 51 Kodak film. These photographs were taken by the U.S. Air Force as part of the SOON system, and they were kindly provided by Dr. Neidig of the Sacramento Peak Observatory. The angular scale of the V.L.A. map and the Hα photograph are the same, and it can be inferred from the extent of the radio emission of $\sim 1'$.

sunspot. This displacement is in the proper direction and of the right order of magnitude to compensate for the projection effect caused by the higher radio emission. For a height of 2 x 10^9 cm above the Hα level, the radio emission at 61° and 45°E would, respectively, be displaced by 22" and 18" to the east. We therefore conclude that our displacement of the radio map gives an order of magnitude estimate of its height and compensates for projection effects. The data shown in Figure 1 indicate that small regions of bright plage are associated with enhanced radio emission and that the structural changes seen at 6 cm wavelength are correlated with similar changes in the chromospheric plage. Not only is the radio emission dominated by a plage-associated component whose individual features are correlated with bright Hα emission; but there is also weak or undetectable radio emission from the regions which directly overlie sunspots. Two small (∿ 10"), bright (∿ 10^6K) radio sources were found on the outer edges of one sunspot (on October 6), however, and it is likely that these sources are related to the strongly curved magnetic field lines found at the outer edges of sunspots.

Figure 2. V.L.A. synthesis map of the circular polarization or Stokes parameter V, at λ = 6 cm for AR 2032 on October 6, 1979. Here the contours mark levels of equal brightness temperature corresponding to 0.2, 0.4, 0.6 and 0.8 times the maximum brightness temperature of 1.02 x 10^6 K. The ratio of the temperatures of the V and I maps indicate that the degree of circular polarization ρ_c = V/I is 30±10% throughout the bright plage-associated component of radio emission. The V map is compared with a Kitt Peak National Observatory (KPNO) magnetogram taken on the same day using Zeeman effect observations of the 8680 Å line of neutral iron. The circular polarization maps and the magnetograms respectively delineate the structure of the longitudinal component of the magnetic field in the corona and the photosphere. The magnetogram has been kindly provided by William Livingston of KPNO, and it has an angular scale which is the same as that of the drawing superimposed on it.

In Figure 2, we present the V.L.A. synthesis map of circular polarization, V, at 6 cm on October 6 and compare it to a magnetogram of the same region. No magnetogram was available for October 5. Here, dark magnetogram areas refer to regions of negative magnetic polarity and correspond to positive, left-handed circular polarization (solid lines); whereas light magnetogram areas refer to regions of positive magnetic polarity and negative, right-handed circular polarization (dashed lines). Although the active region is dipolar, the comparison indicates that the bright plage-associated radio source has one dominant magnetic polarity, and that its magnetic structure is correlated with the longitudinal magnetic field seen on magnetograms of the lower lying photosphere. This provides additional evidence that the 6 cm maps of circular polarization act as coronal magnetograms which delineate regions of intense longitudinal magnetic fields[38,39]. The observed sense of circular polarization corresponds to the extraordinary mode of wave propagation. The fact that the dominant plage-associated radio emission exhibits only one dominant magnetic polarity, which agrees with that of the longitudinal magnetic field in the regions away from the sunspots, indicates that radio emission at 6 cm wavelength is not, in this case at least, directly associated with the magnetic fields of sunspots. One small, intense, left circularly polarized radio source appears to overlie a positively polarized region. This could be the result of a changing magnetic field configuration with height, or it could be due to the ∿ 10" uncertainty in placing the radio contours on the magnetogram. An additional source of uncertainty is the comparison of the nearly instantaneous magnetogram with the synthesis map which takes up to 10 hours to produce. A careful comparison of the V map (Figure 2) and the I map (Figure 1) indicates that the peaks of the two maps do not coincide, and that the circular polarization varies thoughout the active region. Thus the most intense regions of radio emission come from the plage-associated component whose degree of circular polarization is everywhere $\rho_c = 30\pm10\%$. The peak of the V map, however, coincides with a small sunspot whose circular polarization is $\rho_c = 86\pm10\%$, while the larger sunspot exhibits radio emission which is, within the measurement uncertainties, 100% circularly polarized. As we show later, the high circular polarization of the sunspot-associated radio emission can be used in support of the gyroresonant absorption process, while the low circular polarization of the plage-associated radio emission can be explained by the propagation effects of bremsstrahlung in the presence of a moderately strong magnetic field.

2.1.3 Theoretical Explanation of the Plage-Associated and Sunspot-Associated Components

The brightest features of the 6 cm emission from active regions are most probably optically thick, since the brightness temperatures, T_B, are about equal to the electron temperature $T_e \sim 2.5 \times 10^6$K found in the coronal atmosphere above

---

39. Lang, K.R. and Willson, R.F.(1980), Very large array (V.L.A.) observations of solar active regions", I.A.U. Symposium No. 86: Radio Physics of the Sun, M.R. Kundu and T.E. Gergely, Eds., Reidel, Dordrecht.

active regions. However, the largest part of the radio emission comes from regions with lower brightness temperatures, and hence with optical depths $\tau < 1$. For example, 70% of the area of the plage-associated component has a brightness temperature $T_B \sim 0.625 \times 10^6$K and an optical depth $\tau = 0.28$, where $T_B/T_e = [1 - \exp(-\tau)]$. The same area contributes 50% of the total flux observed at $\lambda = 6$ cm, while regions with $T_B > 2 \times 10^6$K contribute only 5% of the total flux.

Both thermal bremsstrahlung and gyroresonance absorption can contribute to the radio wavelength opacity above active regions. We shall try to interpret the results of our observations in the light of these two processes. For bremsstrahlung at radio wavelengths and temperatures exceeding 3×10^5K, the optical depth, τ_B, is given by[40,41]:

$$\tau_B = \frac{9.786 \times 10^{-3} \int N_e^2 dl}{\nu^2 T_e^{3/2}} \ln [\, 4.7 \times 10^{10} \frac{T_e}{\nu} \,], \tag{1}$$

which, at our observing frequency $\nu = 5 \times 10^9$ Hz and, for a representative electron temperature,

$$T_e = 2.5 \times 10^6\text{K} \quad \text{becomes} \quad \tau_B \sim 1.68 \times 10^{-30} \int N_e^2 dl. \tag{2}$$

A representative vertical extent, L_B, for an atmosphere in hydrostatic equilibrium is one-half the scale height, or[41]

$$L_B \sim 1.5 \times 10^3 \, T_e = 3.8 \times 10^9 \text{ cm}, \tag{3}$$

for $T_e = 2.5 \times 10^6$ K. Gyroresonant absorption processes, on the other hand, occur in a localized region of the solar atmosphere, with a much smaller effective thickness, L_{GR}, given by[21,26]

$$L_{GR} = \left(\frac{2\pi}{3} \right)^{\frac{1}{2}} \beta \, L_H \cos \theta, \tag{4}$$

where $\beta = 2 \times 10^{-1} \, T_e^{\frac{1}{2}}$ is the ratio of the electron thermal velocity to the velocity of light, $L_H = H(dz/dH)$ is the scale length of the magnetic field in the vertical direction, and θ is the angle between the ray path and the direction of the field. For $\theta = 0$, $T_e = 2.5 \times 10^6$K, and $L_H \sim 10^9$ cm, we have $L_{GR} \sim 4.8 \times 10^7$ cm. The thermal electrons which emit bremsstrahlung will also emit gyroradiation at the Larmor frequency, $\nu_H = eH/(2\pi mc) \sim 2.8 \times 10^6 H$ Hz, and its harmonics as they spiral about the intense magnetic fields in active regions. The optical depth for the associated gyroresonance absorption, τ_{GR}, is therefore critically dependent on the magnetic field strength, H, and the angle θ between the line of sight and the direction of the magnetic field. For our observing frequency of $\nu = 5 \times 10^9$ Hz,

---

40. Lang, K.R. (1974b), Astrophysical Formulae, Springer Verlag, New York.

41. Lang, K.R. (1980), Astrophysical Formulae, 2nd Edition, Springer Verlag, New York.

the harmonics n = 1, 2, 3, and 4 respectively correspond to H = 1790, 895, 597 and 447 gauss, and for an electron temperature $T_e = 2.5 \times 10^6$K the simplified quasi-longitudinal expression for the optical depth becomes[27,28,29,30]:

$$\begin{aligned} \tau_{GR} &\sim 4.5 \times 10^{-6} N_e (1 \pm \cos\theta)^2 \times \sin^2\theta \text{ for } n = 2,\ H = 895 \text{ Gauss}, \\ \tau_{GR} &\sim 1.3 \times 10^{-8} N_e (1 \pm \cos\theta)^2 \times \sin^4\theta \text{ for } n = 3,\ H = 600 \text{ Gauss}, \\ \tau_{GR} &\sim 6.8 \times 10^{-11} N_e (1 \pm \cos\theta)^2 \times \sin^6\theta \text{ for } n = 4,\ H = 447 \text{ Gauss}, \end{aligned} \tag{5}$$

where we have assumed that $L_H = 10^9$ cm, and the + and - signs respectively refer to the extraordinary and ordinary components of wave motion. It follows from Eqs. (5) that gyroresonant absorption is not an effective opacity agent at n = 4 and H = 447 gauss for the electron densities $N_e = 10^8$-10^{10} cm^{-3} found in the coronal atmosphere above active regions, and that gyroresonance emission is everywhere optically thick at n = 2 and H = 895 gauss for any plausible value of electron density. We may conclude that optically thin emission is only possible if there are unexpectedly strong magnetic fields of H = 600-900 gauss at atmospheric levels where the temperatures reach a million degrees. We also note that the dependence is such that the differences in optical depth which give rise to circularly polarized radiation are only effective at large values of θ. These general conclusions may be confirmed by an examination of the more complicated expressions for τ_{GR} which are not limited to quasi-longitudinal propagation[25,26,27,28,42,43,44], and they are also confirmed by the detailed calculations of Alissandrakis, Kundu and Lantos[35]. These last authors have used models of the temperature, density, and magnetic field structure above sunspots to compute τ_B and τ_{GR} for different values of H, N_e, T_e, and θ. They conclude that gyroresonance emission can dominate bremsstrahlung for the sunspot-associated component of 6 cm emission when the magnetic fields are high (H = 600-900 gauss) and the value of θ is large. Their graphs also indicate that the second harmonic is optically thick to both the extraordinary and ordinary components of wave motion, and that circularly polarized emission can only be expected for the third harmonic (H ∼ 600 gauss) where the ordinary component becomes optically thin at large θ.

It follows from Eqs. (2) and (5) that the parameters which determine the dominant opacity mechanism are essentially the magnetic field strength H and the

---

[42] Ginzburg, V.L. (1961), Propagation of Electromagnetic Waves in Plasma, Gordon and Breach, New York.

[43] Ginzburg, V.L. (1967), Propagation of Electromagnetic Waves in Plasma, 2nd edition, Gordon and Breach, New York.

[44] Krüger, A. (1979), Introduction to Solar Radio Astronomy and Radio Physics, Reidel, Dordrecht.

electron density N_e. Let us first consider the dominant plage-associated radio emission with relatively low brightness temperatures of $T_B \sim 0.625 \times 10^6$K and optical depths $\tau \sim 0.28$. Using this optical depth in Eq.(2) for bremsstrahlung, we obtain an emission measure of

$$\int N_e^2 dl \sim 2 \times 10^{29} \text{ cm}^{-5}, \tag{6}$$

and an average electron density of

$$\bar{N}_e = \left[\frac{\int N_e^2 dl}{L_B}\right]^{\frac{1}{2}} \sim 5 \times 10^9 \text{ cm}^{-3}. \tag{7}$$

For the same electron density, Eq. (5) indicates that the optical depth due to gyroresonance absorption will be larger than unity only for $n = 2, 3$, i.e. $H = 895$ or 567 gauss. In other words, the gyroresonance absorption can only account for the plage-associated radio emission if the magnetic field strength $H \sim 600$ gauss. Because coronal magnetic field strengths are in general much weaker than this value, only bremsstrahlung can account for the observed emission. This conclusion is independently supported by Skylab X-ray observations of the hot,dense plasma distributed in coronal magnetic loops above active regions. The X-ray observations indicate $T_e \sim 2.5 \times 10^6$K and $\int N_e^2 dl \sim 2 \times 10^{29}$ cm^{-5} for the hot plasma trapped in magnetic arches above some other active regions[45,46,47,48].

A different explanation has to be found for the brightest emission and also for the regions associated with the sunspots. For the regions with $T_B > 2 \times 10^6$K, the bremsstrahlung explanation would require an increase in emission measure, provided that there are not local enhancements in electron temperature, and such an increase exceeds the average values inferred from X-ray measurements. Also, although the X-ray data indicate enhancements of electron density in the coronal atmosphere above active regions, both X-ray and E.U.V. observations indicate that the electron density and/or temperature have lower values directly above sunspots. The X-ray observations, for example, indicate that the emission measure above sunspots is substantially lower than that above the plage with sunspot-associated emission measures of $\int N_e^2 dl \sim 10^{27}$ cm^{-5},[36]. Moreover, comparisons of optical wavelength observations, radio observations at 2.8 cm wavelength and Skylab X-ray observations have shown the presence of bright components with T_B in the range 1-2 x 10^6K just above sunspots.[36] The presence of such bright components associated with sunspots

---

45. Landini, M., Monsignori Fossi, B.C., Krieger, A. and Vaiana, G.S. (1975), The coronal structure of active regions, Solar Phys. 44:69-82.

46. Vaiana, G.S. (1976), The X-ray corona from Skylab, Phil. Trans. Roy. Soc. London 281:365-374.

47. Vaiana, G.S., Krieger, A.S., Timothy, A.F. and Zombeck, M. (1976), ATM observations, X-ray results, Ap. Space Sci. 39:75-101.

48. Vaiana, G.S. and Rosner, R. (1978), Recent advances in coronal physics, Ann. Rev. Astron. Ap. 16:393-428.

has also been found for some regions at 6 cm wavelength by Alissandrakis et al.[35]. Clearly in these cases bremsstrahlung does not provide sufficient optical depth to explain the enhanced radio emission. The dominant opacity mechanism in these cases is gyroresonance absorption at the second and third harmonic. Unexpectedly high magnetic fields of H = 600-900 gauss are therefore inferred for regions above sunspots where temperatures reach 10^6 K.

The conclusion that thermal bremsstrahlung and relatively weak magnetic fields prevail in the plage-associated regions, while gyroresonance absorption and strong magnetic fields are inferred for sunspot-associated regions, is supported by our observations of circular polarization. Comparison of the I and V synthesis maps for October 6 (Figures 1 and 2) indicate that the degree of circular polarization is $\rho_c \sim 30 \pm 10\%$ throughout the plage-associated component of radio emission, while $\rho_c \sim 90 \pm 10\%$ for the sunspot-associated components. For the plage-associated emission we may retain the assumption that the dominant radiation mechanism is thermal bremsstrahlung and the observed circular polarization can be explained in terms of a propagation effect. An electromagnetic wave passing through a magnetoionic medium is split into two normal waves, the ordinary, o, and the extraordinary, e, waves. Under the assumption of quasi-longitudinal propagation, the degree of circular polarization, ρ_c, of the emergent radiation is given by[40,41,44,49]:

$$\rho_c = \frac{\exp(-\tau_o)-\exp(-\tau_e)}{2-[\exp(-\tau_e)+\exp(-\tau_o)]} \tag{8}$$

where τ_o and τ_e are the optical depths of the ordinary and extraordinary waves,

$$\tau_o = \frac{\tau_B}{[1+(\nu_H \cos /\nu)]^2} \tag{9}$$

and

$$\tau_e = \frac{\tau_B}{[1-(\nu_H \cos /\nu)]^2}, \tag{10}$$

with τ_B denoting the optical depth in the absence of an external magnetic field, the observing frequency is ν, and $\nu_H = 2.8 \times 10^6$ H Hz. For the optically thin case, we can infer from Eq. (8) and from an observed $\rho_c \sim 30\%$, a magnetic field intensity of H = 250 gauss. Thus the low circular polarization observed for the radio emission from the plage-associated component can be interpreted in terms of propagation effects of optically-thin, thermal bremsstrahlung in the presence of a magnetic field of strength H $\sim$ 250 gauss. The thermal bremsstrahlung hypothesis is, in fact, favored for the more extensive plage-associated radio emission because relatively low magnetic field strengths are inferred; whereas high field strengths of H = 600 gauss are needed if gyroresonance emission accounts for the observed circular polari-

---

49. Ratcliffe, J.A. (1962), The Magneto-Ionic Theory, Cambridge University Press, Cambridge.

zation. For the optically thick case with $\tau \overset{>}{\sim} 1$, which is the situation for the brightest peaks with $T_B > 2 \times 10^6$K, the circular polarization should be strongly reduced independent of the process of absorption. In fact, our observations indicate that the regions of greatest intensity do not coincide with the regions of highest circular polarization.

The high degree of circular polarization of $\rho_c = 90 \pm 10\%$ observed for the sunspot associated component of radio emission is consistent with the high magnetic field strengths required for intense gyroresonance emission. If $\rho_c = 90\%$ is due to propagation effects, then Eq. (8) indicates that a magnetic field strength of $H \sim 1{,}800$ gauss is required. Such a strong magnetic field would cause the regions to be everywhere optically thick to gyroresonant absorption, and $H \sim 1{,}800$ gauss is not expected at atmospheric levels where the temperatures $T \sim 10^6$K. Instead, the high circular polarization of the sunspot-associated emission favors gyroresonance emission which is itself circularly polarized for $H \sim 600$ gauss. In this case, gyroresonance absorption becomes optically thin for the ordinary wave, while remaining optically thick for the extraordinary wave and producing radiation that is circularly polarized in the sense of the extraordinary wave. The observed circular polarization is therefore consistent with the bremsstrahlung interpretation of the plage-associated radio emission where moderate magnetic field strengths of $H \sim 250$ gauss are inferred, but the observed polarization is probably inconsistent with this interpretation for the sunspot-associated component where gyroresonance absorption and more intense magnetic field strengths of $H \sim 600$ gauss are required at atmospheric levels in which the temperature $T \sim 10^6$K. Nevertheless, our observations indicate that the large majority of the radio flux from one solar active region is due to bremsstrahlung from coronal condensations overlying plage, and that less than 5% of the observed flux comes from the sunspot-associated component. This suggests that, in spite of its interesting properties, the gyroresonance process may not play the dominant role in the radio emission from active regions, at least in the sources we have observed.

2.1.4 Conclusions - The Two Components of the Slowly Varying Component

We have compared V.L.A. synthesis maps of the active region AR 2032 at 6 cm wavelength with Hα photographs and magnetograms with comparable angular resolutions and second-of-arc positional accuracy. The large majority of the observed flux comes from a small (∼ 30"), bright ($\sim 10^6$K), circularly polarized ($\rho_c \sim 30\%$) source which overlies the chromospheric plage seen as bright regions on Hα photographs. We interpret this plage-associated component of enhanced radio emission in terms of thermal bremsstrahlung. The bremsstrahlung interpretation is supported by:

1. The fact that the detailed morphological features of the 6 cm emission

are well correlated with the bright plage seen at Hα wavelengths. The Hα emission must be due to thermal processes, and it cannot be the result of gyroresonance absorption.

2. The agreement between the physical parameters (emission measure $\sim 2 \times 10^{29}$ cm^{-5}, electron density $\sim 5 \times 10^{9}$ cm^{-3}, electron temperature $\sim 2.5 \times 10^{6}K$) inferred from the bremsstrahlung hypothesis with those inferred from X-ray observations of the coronal atmosphere above active regions.

3. The fact that lower magnetic field strengths of $H \sim 250$ gauss are inferred from the observed degree of circular polarization ($\rho_c \sim 30\%$) and the bremsstrahlung hypothesis. Higher magnetic field strengths of H = 600-900 gauss would be required in extended coronal regions if gyroresonance emission is invoked.

Less than 5% of the observed flux at 6 cm wavelength comes from small ($\sim 10''$), bright ($\sim 10^{6}K$) regions which are strongly circularly polarized ($\rho_c \sim 90\%$), and which lie above or immediately adjacent to sunspots. This sunspot-associated component is interpreted in terms of gyroresonant emission, as has been previously done by Lang[30] and Alissandrakis, Kundu and Lantos[35]. This is supported by:

1. The distinction between the temperature and density structure of the coronal atmosphere above sunspots and plage as inferred from X-ray and EUV observations. Both Alissandrakis, Kundu and Lantos[35] and Pallavicini, Sakurai and Vaiana[37] have called attention to the fact that the low electron density above sunspots requires additional radio wavelength opacity due to gyroresonance absorption if radio emission with high brightness temperatures of $T_B \sim 10^{6}K$ are to be explained.

2. The high degree of circular polarization $\rho_c = 90 \pm 10\%$ observed for the sunspot-associated component of radio emission. This high polarization requires the high magnetic field strengths needed for gyroresonant emission ($H \sim 600$ gauss), and it actually favors this process which gives high polarization with weaker fields ($H \sim 600$ gauss) than those required if the polarization is due to propagation effects ($H \sim 1,800$ gauss).

3. The magnetic field strengths of $H \sim 600$ gauss needed for gyroresonance emission are more likely to occur near sunspots where the magnetic field is enhanced.

We therefore conclude that the 6 cm radio emission from active regions is represented by a two-component model in which coronal regions associated with sunspots have low electron densities ($N_e \leq 10^{8}$ cm^{-3}) and unexpectedly high magnetic field strengths (H = 600-900 gauss), and the more extensive coronal regions associated with bright plage have high electron densities ($N_e \sim 2 \times 10^{9}$ cm^{-3}) and relatively low magnetic field strengths ($H \leq 250$ gauss). The vast majority of the radio flux observed at 6 cm wavelength could come from the bremsstrahlung of these hot, dense coronal condensations. For $H \sim 250$ gauss, the magnetic energy density $H^2/8\pi \sim 3 \times 10^{3}$ ergs cm^{-3} vastly exceeds the equipartition value inferred from the virial theorem, for the thermal kinetic energy density of the coronal condensations is $3N_e kT_e \sim 5$ ergs cm^{-3}. Our observations therefore support the view that the hot, dense coronal condensations are shaped by intense magnetic fields. Our observations also open up the possibility that some of the previously unresolved core sources of the slowly varying S component are due to the thermal bremsstrahlung of the coronal condensations detected at X-ray wavelengths.

2.2 POLARIZED HORSESHOES AROUND SUNSPOTS

2.2.1 Introduction

High resolution observations of solar active regions at 6 cm wavelength with the Westerbork Synthesis Radio Telescope (W.S.R.T.) led to the discovery of sunspot-associated sources with small angular sizes $\phi \lesssim 0.5'$, high degrees of circular polarization $\rho_c = 50\%$ to 90%, and high brightness temperatures, $T_B \sim 10^6 K$,[34,35]. These compact sources were also observed by Lang and Willson[38,39] who used the Very Large Array (V.L.A.) at 6 cm wavelength to show that the sunspot-associated sources mark the feet of magnetic dipoles, and that the structure and sense of their circular polarization is well correlated with the longitudinal component of the magnetic field in the underlying photosphere. This sunspot-associated component of enhanced 6 cm emission has been attributed to the gyroresonance emission of thermal electrons spiralling in the intense magnetic fields of sunspots[22,25,30].

Plane parallel models of the temperature and density structure in the chromosphere-corona transition region have been used to predict the gyroresonance emission expected in the magnetic fields above sunspots [26,27,28]. The general conclusion of these theoretical models is that the total intensity of the 6 cm emission will be enhanced above sunspot umbrae where the strong, radial magnetic fields allow the detection of the third harmonic of the gyrofrequency at higher, hotter levels in the solar atmosphere where the temperature gradient is small. Because the penumbral magnetic fields are weaker and strongly curved within the lower lying, cooler material, however, the total intensity of the 6 cm emission is expected to exhibit a sharp gradient above sunspot penumbrae. As pointed out by Gel'freikh and Lubyshev[50], the theory of gyroresonant absorption indicates an entirely different behavior for the circularly polarized emission. Because of the strong magnetic fields above sunspot umbrae, both the extraordinary and ordinary modes of wave propagation are expected to become optically thick, and the circular polarization will drop to undetectable levels. Only the extraordinary mode becomes optically thick above the

---

[50] Gel'freikh, G.B. and Lubyshev, B.I. (1979), Structure of local sources of the S component of solar radio emission, Sov. Astr. AJ 23:316-322.

penumbra, however, and a circularly polarized ring is therefore predicted for a sunspot which is viewed centrally. Because of the different orientation of the penumbral magnetic field, these polarized rings will open into horseshoe shaped structures whenever the line of sight is not coincident with the radial axis of the sunspot. Alissandrakis, Kundu and Lantos[35] reported the first tentative experimental verification of these predictions when they detected a double-peaked structure in the circularly polarized emission above a sunspot at 6 cm wavelength. They reasoned that the predicted horseshoe would decompose into two peaks when convolved with the large, elongated synthesized beam. Alissandrakis, Kundu and Lantos also detected the predicted enhancement of total intensity above the sunspot umbra where the brightness temperatures exceed a million degrees.

Curiously enough, there has been more recent evidence that there are temperature depressions above some sunspot umbrae at 6 cm wavelength. Felli, Lang and Willson[2] showed, for example, that the sunspot-associated emission from one active region occurs at the outer edges of a sunspot where the magnetic field lines are strongly curved, and that the most intense 6 cm emission is correlated with bright chromospheric plage rather than with sunspots. Kundu, Schmahl and Rao[51] similarly found that the most intense 6 cm sources in other active regions are associated with filamentary structures and magnetic neutral lines, and that they are not located directly over sunspots. This was attributed to the existence of cool material above the sunspot umbrae. In fact, Foukal[52,53,54] has argued several times that the cool "plumes" observed at E.U.V. wavelengths indicate that the coolness of sunspots persists up into the corona. Considerable excitement has therefore been generated by Alissandrakis and Kundu's[55] dramatic discovery of a 6 cm ring around a sunspot. Their observations indicate that the total intensity of the 6 cm emission from one sunspot comes predominantly from a ring structure with a size between that of the umbra and the penumbra. Furthermore, the circularly polarized emission has the horseshoe shape which had been predicted from the theory of gyroresonant emission. The unexpected temperature depression above the sunspot umbra was interpreted as being due to low gyroresonant opacity when the umbra is viewed along its radial axis[29], or to cool material which lies above the umbra.

---

[51] Kundu, M.R., Schmahl, E.J. and Rao, A.P. (1981), V.L.A. observations of solar active regions at six cm wavelength, Astr. Ap. 94:72-79.

[52] Foukal, P.V. (1975), The temperature structure and pressure balance of magnetic loops in active regions, Solar Phys. 43:327-336.

[53] Foukal, P.V. (1976), The pressure and energy balance of the cool corona over sunspots, Ap. J. 210:575-581.

[54] Foukal, P.V. (1978), Magnetic loops, downflows, and convection in the solar corona, Ap. J. 223:1046-1050.

[55] Alissandrakis, C.E. and Kundu, M.R. (1981), Observations of ring structure in a sunspot associated source at six centimeter wavelength, Ap. J. Lett. 253: L49-L51.

Here, we report the related discovery of circularly polarized horseshoes which ring sunspot umbrae and lie above their penumbrae. In contrast with Alissandrakis and Kundu's result, however, we do not observe a temperature depression in the 6 cm emission above sunspot umbrae. The brightness temperatures are instead enhanced with values of $T_B \sim 10^6$K. In Section 2.2.2 we present the 6 cm synthesis maps of total intensity and circular polarization, and compare them with photospheric magnetograms, Hα photographs, and offband Hα photographs. In Section 2.2.3 we interpret our results in terms of the theory of gyroresonant emission. Here we also attempt to resolve the paradoxical reports of both cool and hot material in the coronal atmosphere above sunspot umbrae.

2.2.2 Observations of Polarized Horseshoes above Sunspot Penumbrae

We have used the Westerbork Synthesis Radio Telescope (W.S.R.T.) to observe the solar active regions AR 3159 and AR 3161 on June 14 and 16, 1981, respectively. The position of AR 3159 on the solar surface was 26°S and 31°E at 14^hU.T. on June 14, and the position of AR 3161 was 20°S and 34°E at 14^hU.T. on June 16. The active regions were observed for approximately eleven hours each day at a wavelength of 6.16 cm (or 4874 MHz) with a bandwidth of 10 MHz. Details of the observing procedure are given by Bregman[56]. The shortest and longest baselines were 54 m and 2718 m, and the baseline increment was 72 m. The average correlated flux of 40 interferometer pairs was sampled every 0.1 s for both total intensity, I, and circular polarization, V, but these data were time averaged over 10 s before constructing synthesis maps. The phase data were calibrated by observing 3C 147 for a few minutes every hour, and the amplitude data were calibrated by observing Cassiopeia A whose flux density at 6 cm wavelength was taken to be 745 Jy. Corrections for solar rotation were applied by assuming that the 6 cm emission lies at a height of 2×10^9 cm above the photosphere.

The synthesis maps of total intensity I and circular polarization V were obtained by Fourier transforming the calibrated data for roughly 10,000 u-v components obtained during the daylight hours. The synthesized beam pattern for each day had half power widths of 4.5" x 11.4" with the elongation in the north-south direction. The "dirty" or "uncleaned" synthesis maps for AR 3159 are shown in Figures 3 and 4. The contours of the I map (A) mark levels of brightness temperature corresponding to 0.1, 0.2...0.9 times the maximum brightness temperature of 2.2×10^6 K. The contours of the V map (B) mark levels of equal brightness temperature corresponding

---

[56] **Bregman, J.D. (1980), Netherlands Foundation for Radio Astronomy Report No. 330, Westerbork.**

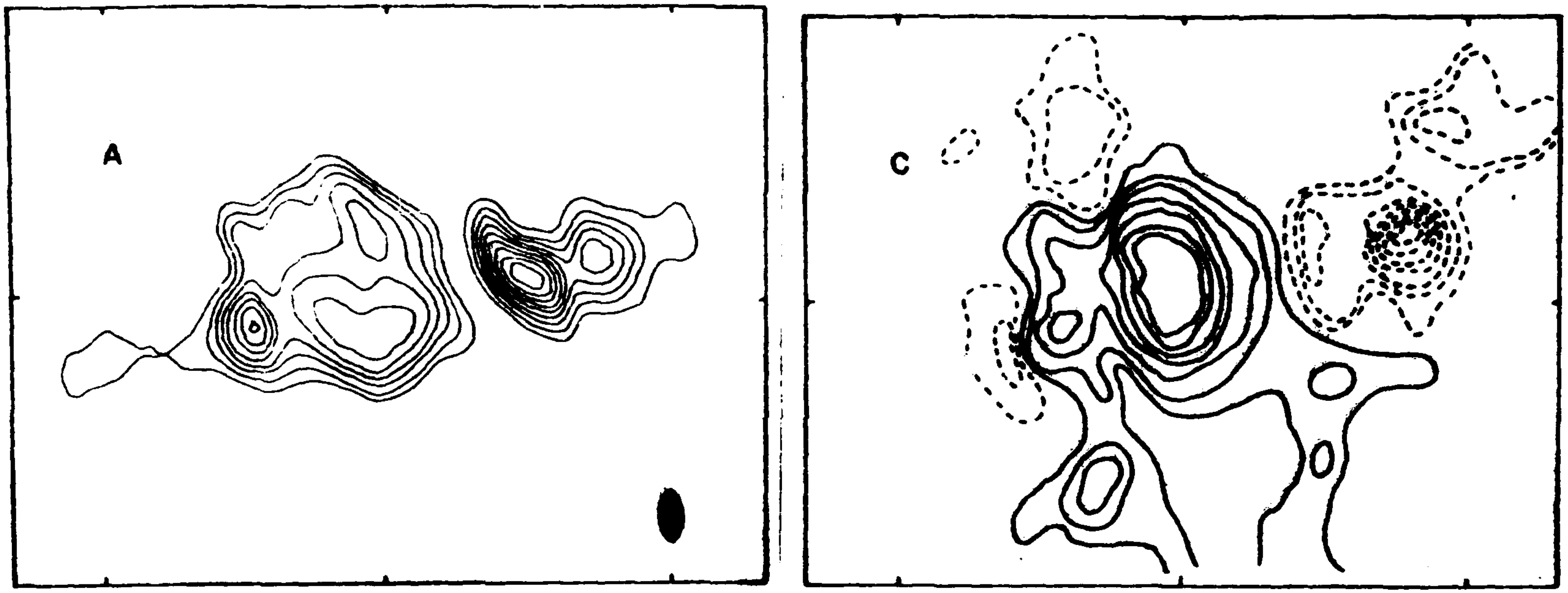

Figure 3. Synthesis map (A) of total intensity I at 6 cm wavelength, and map (C) of the longitudinal component of the photospheric magnetic field. Here, north is up and west is to the right. All of the data refer to the same active region AR 3159 observed on the same day, June 14, 1981, with identical fields of view and angular scales denoted by the 60" spacing between the fiducial marks on the axes. The synthesis map was obtained with the Westerbork Synthesis Radio Telescope and the magnetic field data were obtained by Jean Rayrole with the Meudon magnetogram. Notice that the total intensity of the 6 cm emission is well correlated with intense photospheric fields; that the 6 cm brightness temperature is $\sim 10^6$ K above sunspot umbrae; and that no detectable 6 cm emission bridges the regions of opposite magnetic polarity.

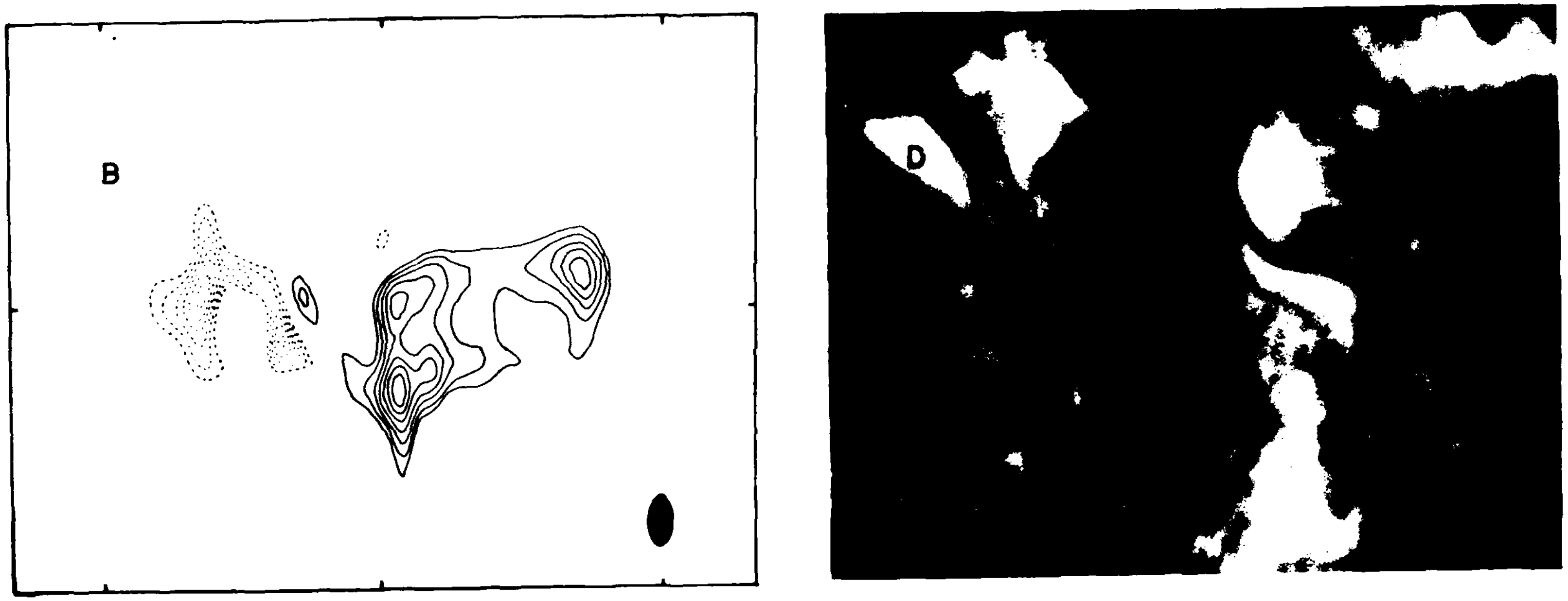

Figure 4. Synthesis map (B) of circular polarization V at 6 cm wavelength and an Hα photograph (D) showing the three sunspots which dominate the region. All of the data refer to the same active region AR 3159 observed on the same day, June 14, 1981, with identical fields of view and angular scales denoted by the 60" spacing between the fiducial marks on the axes. The synthesis map was obtained with the Westerbork Synthesis Radio Telescope and the Hα photograph was taken by the U.S. Air Force as part of the SOON system (courtesy Viola Miller).

to 0.3, 0.4,...0.9 times the maximum brightness temperatures of +3.0 x 10^5 K and -2.8 x 10^5 K. The solid contours of the V map refer to regions of positive, left-handed circular polarization and negative (south or black) magnetic polarity. The dashed contours of the V map correspond to negative, right-handed circular polarization and positive (north or white) magnetic polarity. The Meudon photospheric magnetogram (C) taken by Jean Rayrole on the same day at 13^h 59^m U.T. has solid contours corresponding to longitudinal magnetic field strengths of -200, -400, -600, -800, -1000, -1500 and -2000 gauss and dashed contours corresponding to longitudinal magnetic field strengths of +100, +200, +400, +600, +800 and +1000 gauss. The three main sunspots are also seen in the Hα photograph (D). The observed sense of the circular polarization of the 6 cm emission corresponds to the extraordinary mode of wave propagation.

A comparison of the various maps contained in Figures 3 and 4 indicates that the strongest emission peaks at 6 cm wavelength lie above sunspot umbrae where the longitudinal component of the photospheric magnetic field is most intense (+1000 to -2000 gauss). The high brightness temperatures of $T_B \sim 10^6$K indicate that hot rather than cool material is found in the solar atmosphere above these sunspot umbrae. The two main components of 6 cm emission mark the legs of a magnetic dipole, and there is no detectable 6 cm emission from low-lying coronal loops which might join the regions of opposite magnetic polarity. The degree of circular polarization becomes as high as 95% at the peaks of the features shown in the V map (B), but there is no detectable circular polarization ($\lesssim$ 15%) at the strongest emission peaks at 6 cm wavelength. The regions of strongest circular polarization occur where the longitudinal component of the photospheric magnetic field is relatively weak and has a sharp gradient coinciding with a similar gradient in the 6 cm emission.

Of special interest is the horseshoe shaped structure found in the circular polarization map (B). As illustrated in Figure 5, the horseshoe rings a sunspot umbra and lies above the penumbra where the magnetic fields are strongly curved. Similar horseshoes do not surround nearby sunspots which have more intense magnetic fields. Alissandrakis and Kundu[55] have recently reported their discovery of polarized horseshoes which ring sunspot umbrae; but their result differs from ours in finding a depression of total intensity (or temperature) above the sunspot umbrae.

The "dirty" or "unclean" maps for AR 3161 are shown in Figures 6 and 7. The contours of the I map (A) mark levels of equal brightness temperature corresponding to 0.1, 0.2,...0.9 times the maximum brightness temperature of 2.8 x 10^6 K. The contours of the V map (B) mark levels of equal brightness temperature corresponding to 0.3, 0.4...1.0 times the maximum brightness temperatures of +3.2 x 10^5 K and -4.6 x 10^5 K. The solid and dashed contours have the same meaning as those in Figures 3 and 4. The Meudon photospheric magnetogram (C) taken by Jean Rayrole on the same

Figure 5. The 6 cm synthesis map of circular polarization V (see Figure 4) is superimposed upon an offband Hα photograph of the same region AR 3159 taken on the same day. The angular scale is denoted by the 60" spacing between the fiducial marks on the axes. Notice that there is no detectable polarized emission above the sunspot umbrae where the magnetic fields are strong and nearly vertical, and that the polarized emission is concentrated above the penumbrae where the magnetic field lines are curved and the field strength is weaker and has a sharp gradient. The offband Hα photograph was taken at the Big Bear Solar Observatory (courtesy of Francis Tang).

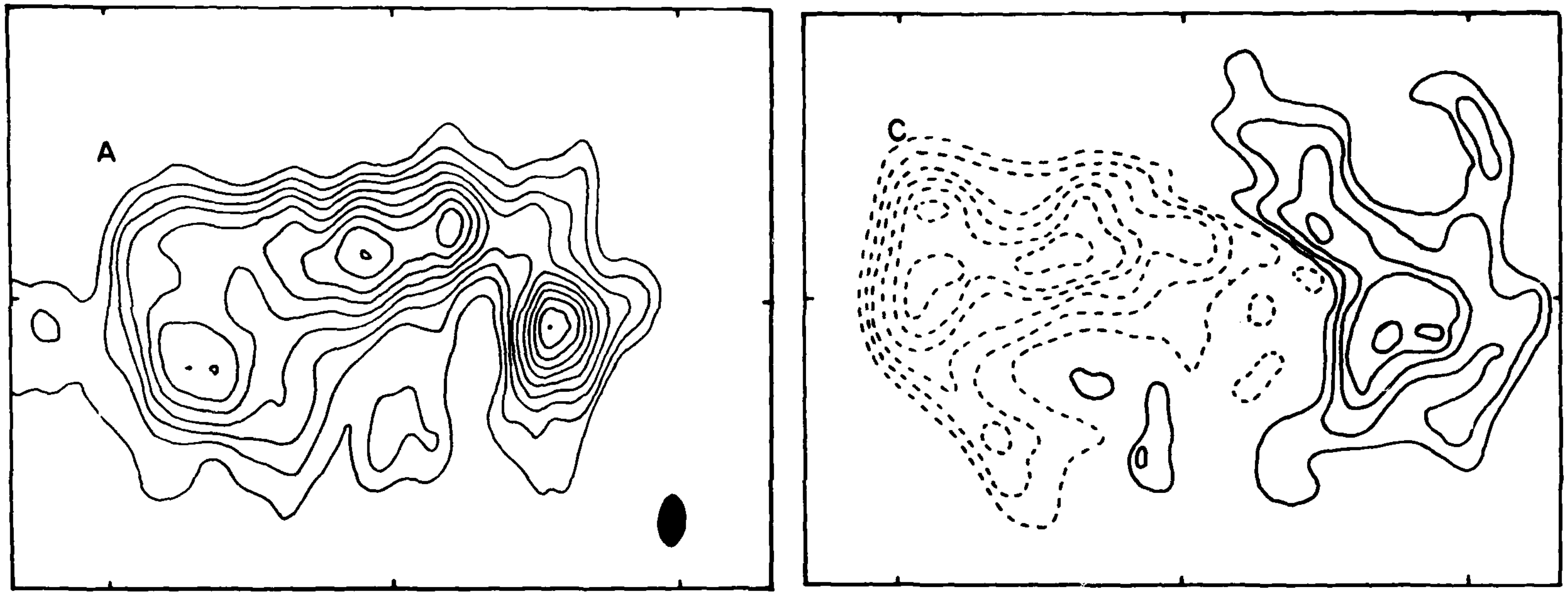

Figure 6. Synthesis map (A) of total intensity I at 6 cm wavelength, and map (C) of the longitudinal component of the photospheric magnetic field. Here, north is up, and west is to the right. All of the data refer to the same active region AR 3161 observed on the same day, June 16, 1981, with identical fields of view and angular scales denoted by the 60 " spacing between the fiducial marks on the axes. The synthesis map was obtained with the Westerbork Synthesis Radio Telescope and the magnetic field data were obtained by Jean Rayrole with the Meudon magnetogram. Notice that the total intensity of the 6 cm emission is well correlated with intense photospheric fields, and that in this case 6 cm emission bridges the regions of opposite magnetic polarity thereby mimicking a low-lying coronal loop.

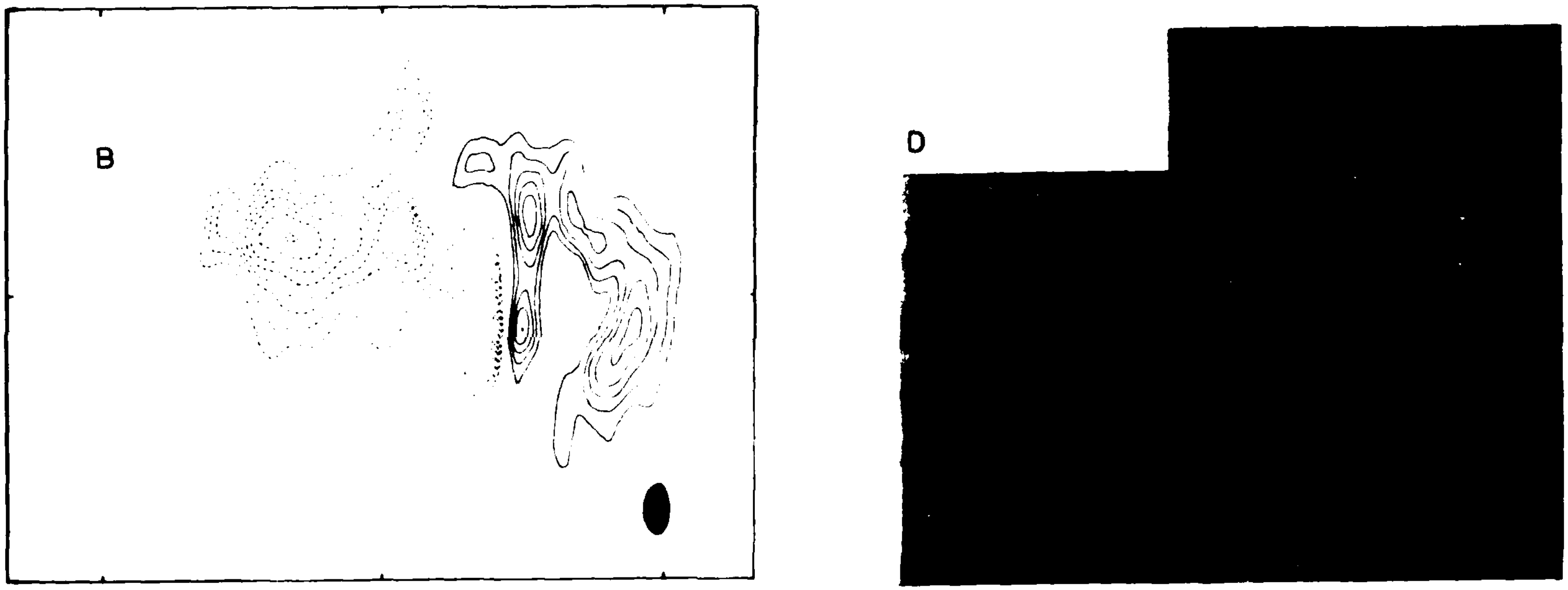

Figure 7. Synthesis map (B) of circular polarization and an offband Hα photograph (D) showing the complicated, curvilinear arrangement of the sunspots. Here, north is up and west is to the right. All of the data refer to the same active region AR 3161 observed on the same day, June 16, 1981, with identical fields of view and angular scales denoted by the 60" spacing between the fiducial marks on the axes. The synthesis map was obtained with the Westerbork Synthesis Radio Telescope, and the offband Hα photograph was taken at the Big Bear Solar Observatory (courtesy of Francis Tang). Notice that the horseshoe shaped polarized emission coincides with regions where the photospheric magnetic field strength is relatively weak and has a sharp gradient.

day at 15^h37^m U.T. has solid contours corresponding to longitudinal magnetic field strengths of −200, −400, −600, −800 and −1000 gauss and dashed contours corresponding to longitudinal magnetic field strengths of +200, +400, +600, +800, +1000 and +1500 gauss. The sunspot configuration is delineated in the offband $H\alpha$ photograph. The observed sense of the circular polarization of the 6 cm emission corresponds to the extraordinary mode of wave propagation.

A comparison of the various maps contained in Figures 6 and 7 again illustrates a remarkable correlation between strong emission at 6 cm wavelength (map A) and sunspot umbrae with intense photospheric magnetic fields (maps C and D). A hot million degree plasma is again found above sunspot umbrae, but in this case there is also strong 6 cm emission from sunspot penumbrae and the areas which bridge the gap between regions of opposite magnetic polarity. This radiation may be the optically thin bremsstrahlung of low-lying coronal loops which join the two main groups of sunspots. Here we again find a horseshoe shaped structure in the circular polarization map (B) which rings sunspot umbrae and coincides with penumbral regions where the magnetic fields are strongly curved. Most of the more intense emission peaks at 6 cm wavelength again contain no detectable circular polarization ($\leq$ 15%), and circular polarizations of up to 95% occur in regions where both the 6 cm emission and the longitudinal component of the photospheric magnetic field are relatively weak and exhibit sharp gradients.

2.2.3 Interpretation of the Polarized Horseshoes in terms of Gyroresonant Emission

We have detected intense emission peaks at 6 cm wavelength which exhibit a remarkable correlation with the longitudinal magnetic field in the underlying photosphere. The enhanced 6 cm emission above sunspots indicates the presence of hot, million degree material in the coronal atmosphere overlying sunspot umbrae. Alissandrakis, Kundu and Lantos[35] have shown that this is to be expected from the gyroresonant emission of thermal electrons in plausible configurations of sunspot magnetic fields; provided that the temperature and density of the transition region and low solar corona vary only in the direction perpendicular to the solar surface. Detectable gyroresonant emission is expected at the second and third harmonics of the gyrofrequency. This means that unexpectedly high longitudinal magnetic field strengths of H_ℓ = 600 to 900 gauss must be present in regions above sunspot umbrae which have temperatures of 10^6K. As suggested by Brombozcz <u>et al</u>.[57] this could be explained if there is a relatively thin transition zone above sunspots. A thin zone would allow a high temperature close to sunspots where the magnetic fields are stronger. This

---

[57] **Brombozcz, G. <u>et al</u>. (1981), Report to the Crimean solar maximum year workshop.**

cannot always be the case, however, for Lang, Willson and Gaizauskas[6] have used projection effects to infer a height of h $\sim$ 4 x 10^9 cm above the photosphere for the sunspot-associated components of 6 cm emission, and this is comparable to the height of the plage-associated component of 6 cm emission[2]. We feel that it is more likely that the intense magnetic fields of sunspot umbrae project radially upwards into the low solar corona with little loss of strength. This enables the third harmonic of the gyrofrequency to occur at higher, hotter levels of the solar atmosphere where the temperature gradient is small.

The situation is different for the curved magnetic fields of the sunspot penumbrae. In this case the resonance levels corresponding to the third harmonic occur in the lower-lying cooler regions of the solar atmosphere where the temperature gradients are large. The observed circular polarization requires resonance at the third harmonic (H_ℓ = 600 gauss) because the second harmonic is optically thick and gyroresonant absorption is an ineffective opacity agent at the fourth harmonic. The high degrees of circular polarization (ρ_c = 95%) of the peaks of our newly discovered horseshoe structures require gyroresonant emission. If this high polarization were due to propagation effects instead of a gyroresonance, a high longitudinal magnetic field strength of H_ℓ = 1800 gauss would be required. Such high field strengths are not even observed in the penumbral regions of the underlying photosphere (see magnetograms in Figures 3 and 6), and at any rate they would cause the regions to be everywhere optically thick to gyroresonant absorption. Furthermore, the gyroresonant interpretation is fully confirmed by the theoretical work of Gel'freikh and Lubyshev[50] and Alissandrakis, Kundu and Lantos[35] which predicted the existence of the circularly polarized horseshoes which we have observed. Here we should also point out that Alissandrakis and Kundu[55] also observed the circularly polarized horseshoe structures, and that only one of these had a brightness depression at its center. As Zheleznyakov[29] noticed, a depression might be observed when the line of sight coincides with the radial axis of the sunspot, and the negligible gyroresonant absorption allows the observation of the cool material underlying the corona.

Our observations show no evidence for a cool region above sunspot umbrae, contrary to the suggestions of Foukal[52,53,54] and the single observation of Alissandrakis and Kundu[55]. According to Foukal, cool "plumes" which are detected at E.U.V. wavelengths above sunspot umbrae, project upwards into the solar corona to form cool loops. One way of explaining our failure to detect these cool regions would be to suppose that both hot and cold material lie above different sunspots, and that we just happened to observe those which have hot material overlying them. Sheeley[58] has shown that the cool spikey structures which project upwards from sunspot umbrae

---

[58] Sheeley, N.R. (1980), Temporal variations of loop structures in the solar atmosphere, Solar Phys. 66:79-87.

evolve with rapid time scales of minutes to tens of minutes, however, and theoretical considerations indicate that static cool loops are unstable. Furthermore, Pallavicini, Sakurai and Vaiana[37] have shown that the cool "plumes" fill only a fraction (one third) of the umbral area, and that cool loops coexist with hot loops. They also showed that the cool loops are variably oriented and change considerably with time, while it is well-known that the hot coronal loops detected at X-ray wavelengths appear relatively unchanged for time scales of hours. Because the 6 cm synthesis maps refer to structures which are stable for several hours, they would not be expected to exhibit the radio wavelength counterparts of the cool "plumes" and loops; but they would be expected to show the counterparts of the hot X-ray loops. We argue that the hot 6 cm emission detected above sunspot umbrae marks the legs of hot coronal loops.

2.3 MULTIPLE WAVELENGTH OBSERVATIONS OF A SOLAR ACTIVE REGION

2.3.1 Introduction

The relatively recent development of synthesis telescopes has made it possible to map the solar surface in two dimensions at radio wavelengths with angular resolutions comparable to those obtainable at optical wavelengths, while instruments aboard the Skylab and Solar Maximum Mission satellites can delineate two dimensional structure at X-ray and ultraviolet wavelengths with similar angular resolutions. High resolution synthesis maps at 6 cm wavelength indicate intense emission which is associated with sunspots[35], with filamentary structure between sunspots[51], and with both bright Hα plage and sunspots[2]. Felli, Lang and Willson[2] provide a detailed history of previous related work, and argue that the plage-associated component of the 6 cm emission can be explained as the thermal bremsstrahlung of a plasma whose emission measure is comparable with those observed at X-ray wavelengths in regions which do not overlie sunspots. On the basis of a comparison of 2.8 cm and X-ray observations, Pallavicini <u>et al.</u>[36] and Pallavicini, Sakurai and Vaiana[37] have argued that high brightness temperature radio sources associated with sunspots must be explained by thermal gyroresonance absorption, while the plage-associated radio emission can be explained by thermal bremsstrahlung. All of this previous work has been carried out at only one radio wavelength at a time, however, and the comparisons with X-ray data were confused by the poor angular resolution of the 2.8 cm data.

Here, we provide multiple wavelength observations at soft X-ray wavelengths (the O VIII, Ne IX and Mg XI lines), ultra-violet wavelengths (the C IV line), optical wavelengths (Hα and offband Hα), and radio wavelengths (2 cm, 6 cm and 20 cm). These observations are presented in Section 2.3.2 where we also notice various correlations with Hα plage and determine heights for the radio emission. In Section

2.3.3 we interpret the observations in terms of a two component model in which one component is associated with bright Hα plage and the other component is associated with sunspots. We argue that the dominant radiation mechanism of the plage-associated component is bremsstrahlung and that gyroresonant absorption dominates the radio emission of the sunspot associated component; but that both emission mechanisms might be present in both components. The emission measure inferred from the X-ray radiation of the plage-associated component agrees, within the observational uncertainties, with that inferred from the 6 cm and 20 cm emission under the bremsstrahlung hypothesis. Estimates of the longitudinal magnetic field strengths, H_ℓ, are also given in Section 2.3.3 with $H_\ell \sim 100$ and $H_\ell \sim 1{,}000$ gauss, respectively, for the plage-associated and the sunspot-associated components at atmospheric levels where the temperatures reach a million degrees. The high magnetic field strengths above the sunspot-associated component might be attributed to a thin transition zone above sunspots. Section 2.3.4. provides a concise summary of our basic conclusions.

2.3.2 The Multiple Wavelength Observations

We have used the Sacramento Peak (Sac. Peak) Vacuum Tower Telescope, the Solar Maximum Mission (S.M.M.) satellite, the Very Large Array (V.L.A.) and the Westerbork Synthesis Radio Telescope (W.S.R.T.) to observe the active region AR 2490 on June 9 and 11, 1980. The position of AR 2490 on the Sun's surface was 10°S and 12°W at 13^h52^m U.T. on June 9 and 14°S and 39°W at 13^h00^m U.T. on June 11. The observing wavelengths, field of view and angular resolutions are given in Table 1. At Sac. Peak a set of three parallel filters were placed at the focus of the telescope: a Halle filter with a passband of 0.3 Å tuned at the center of the Ca II - K line, a Zeiss filter with a passband of 0.25 Å tuned along the Hα line, the Mg I-b1 line, the Na I-D2 line and the He I-D3 line. Variable exposure times between 0.005s and 0.4 s were used to assure a uniform exposure in all the frames, and a complete sequence of exposures was taken every 75 s. The Flat Crystal Spectrometer (F.C.S.) of the soft X-ray Polychromator (X.R.P.) aboard the S.M.M. satellite was used to sample seven channels every 0.256 s at different wavelengths between 1.4 Å and 22.4 Å corresponding to the resonance lines of the abundant elements at ionization stages corresponding to temperatures between 1.5 and 50 million degrees[59]. An average of eight samples was taken for each of the seven channels at each observing position, and a square raster of 4' in extent with 15" angular resolution was obtained in 19.66 min. Maps of good signal-to-noise were obtained in the three channels corres-

---

[59] Acton, L.W. et al. (1980), The soft X-ray polychromator for the solar maximum mission, Solar Phys. 65:53-71.

TABLE 1. Instrumental properties and the relevant layer of the solar atmosphere for multiple wavelength observations of AR 2490.

Wavelength (cm)	Instrument	Field of View	Angular Resolution	Atmospheric Layer
9.17×10^{-8}	S.M.M.-X.R.P.(Mg XI)	4'x 4'	10" to 15"	Corona
13.45×10^{-8}	S.M.M.-X.R.P.(Ne IX)	4'x 4'	10" to 15"	Corona
18.97×10^{-8}	S.M.M.-X.R.P.(O VIII)	4'x 4'	10" to 15"	Corona
15.48×10^{-6}	S.M.M.-U.V.S.P. (C IV)	4'x 4'	3"	Transition Region
63.63×10^{-6}	Sac. Peak (Hα - 2 Å)	3'x 4'	2"	Photosphere
65.63×10^{-6}	Sac. Peak (Hα)	3'x 4'	2"	Chromosphere
2.00	V.L.A.	3'x 3'	3" x 4"	Transition Region and Corona
6.15	W.S.R.T.	9'x 9'	4" x 9"	
20.53	V.L.A.	29'x 29'	4" x 5"	Corona

ponding to the O VIII, Ne IX and Mg XI lines as denoted in Table 1. The ultraviolet spectrometer (U.V.S.P.) aboard the S.M.M. was used to sample the intensity of the C IV line at a wavelength of 1548 Å every 0.127 s, and a square raster of 4' in extent with 3" angular resolution was obtained in 13.54 min.

The V.L.A. was divided into two sub-arrays to give nearly identical u-v coverage at two wavelengths λ = 2 and 20 cm on June 10, while on June 11 the entire array was switched between λ = 2 cm and λ = 20 cm every 15 min. On June 10 the λ = 2 cm sub-array was composed of 11 antennae with distances from the array center ranging between 0.08 and 10.5 km. The λ = 20 cm sub-array was composed of 12 antennae with distances from the array center ranging between 0.04 and 17.2 km. The average correlated flux of 55 interferometer pairs at λ = 2 cm and 66 interferometer pairs at λ = 20 cm was sampled every 10 s for both the left hand circularly polarized (L.C.P.) and the right hand circularly polarized (R.C.P.) signal, and these data were subsequently time averaged over 60 s before constructing synthesis maps. On June 11 the entire V.L.A. of 22 antennae was used and the average correlated flux of 242 interferometer pairs was sampled every 10 s at both polarizations for alternate 15 min periods at λ = 2 cm and λ = 20 cm, and these data were also time averaged over 60 s before constructing synthesis maps. On both June 10 and 11 the W.S.R.T. consisted of 14 antennae with distances from the array center ranging between 0.054 and 2.72 km. In this case the average correlated flux of 40 interferometer pairs at λ = 6 cm was sampled every 0.1 s for both the LCP and the RCP signals, but these data were time averaged over 120 s before constructing synthesis maps. For both the V.L.A. and the W.S.R.T., observations taken during the daylight hours were calibrated, edited and combined to make synthesis maps of the total intensity, I = (LCP+RCP)/2, and the Stokes parameter, V = (LCP-RCP)/2, which provides a measurement of circular polarization.

The V.L.A. data were calibrated by observing N.R.A.O. 150 for 5 min every 30 min, and by assuming that the flux density of N.R.A.O. 150 is 10.5 and 5.5 Jy, respectively, at λ = 2 and 20 cm. The amplitude and phase of the observed data were calibrated according to the procedures outlined by Lang and Willson[38,39] and Felli, Lang and Willson[2]. At each observing wavelength the calibrated amplitude and phase for each polarization and every antenna pair were taken to be the amplitude and phase of the source visibility function; and the source intensity distribution was then obtained by Fourier transforming the calibrated data and using the "clean" procedure on roughly 36,000 u-v components obtained during the daylight observing hours. The W.S.R.T. data were calibrated by observing Cassiopeia A and 3C 48 whose respective flux densities at λ = 6 cm were assumed to be 745 and 5.4 Jy. The source intensity distribution was then obtained by Fourier transforming the calibrated data for roughly 10,000 u-v components obtained during the daylight observing hours.

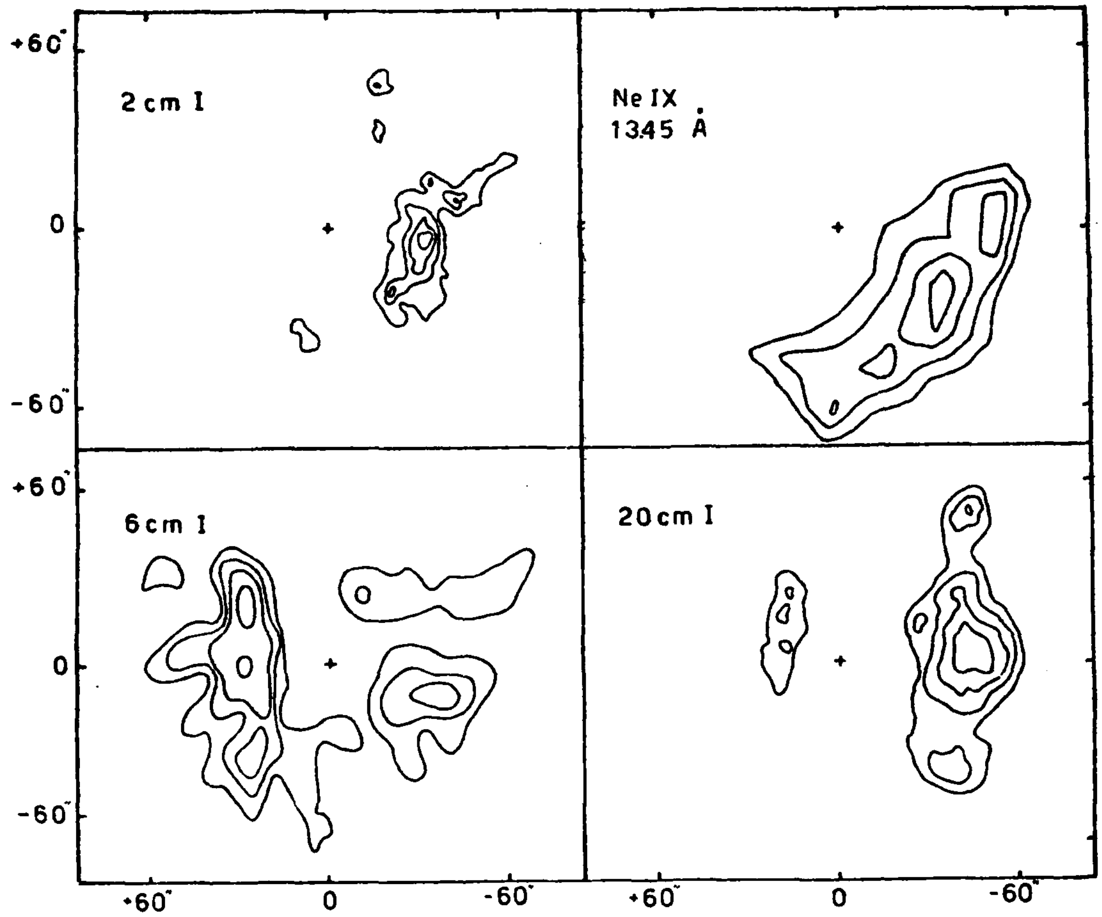

Figure 8. Radio wavelength synthesis maps of the total intensity, I, for AR 2490 at wavelengths of 2 cm (V.L.A.) 6 cm (W.S.R.T.) and 20 cm (V.L.A.) on June 10, 1980 together with an X.R.P. map at the Ne IX line (13.45 Å) taken on the same day. Notice that one component is visible at all wavelengths while the other component is visible only at 6 cm and 20 cm. Here, north is up, west is to the right, and all maps have the same center denoted by a cross mark.

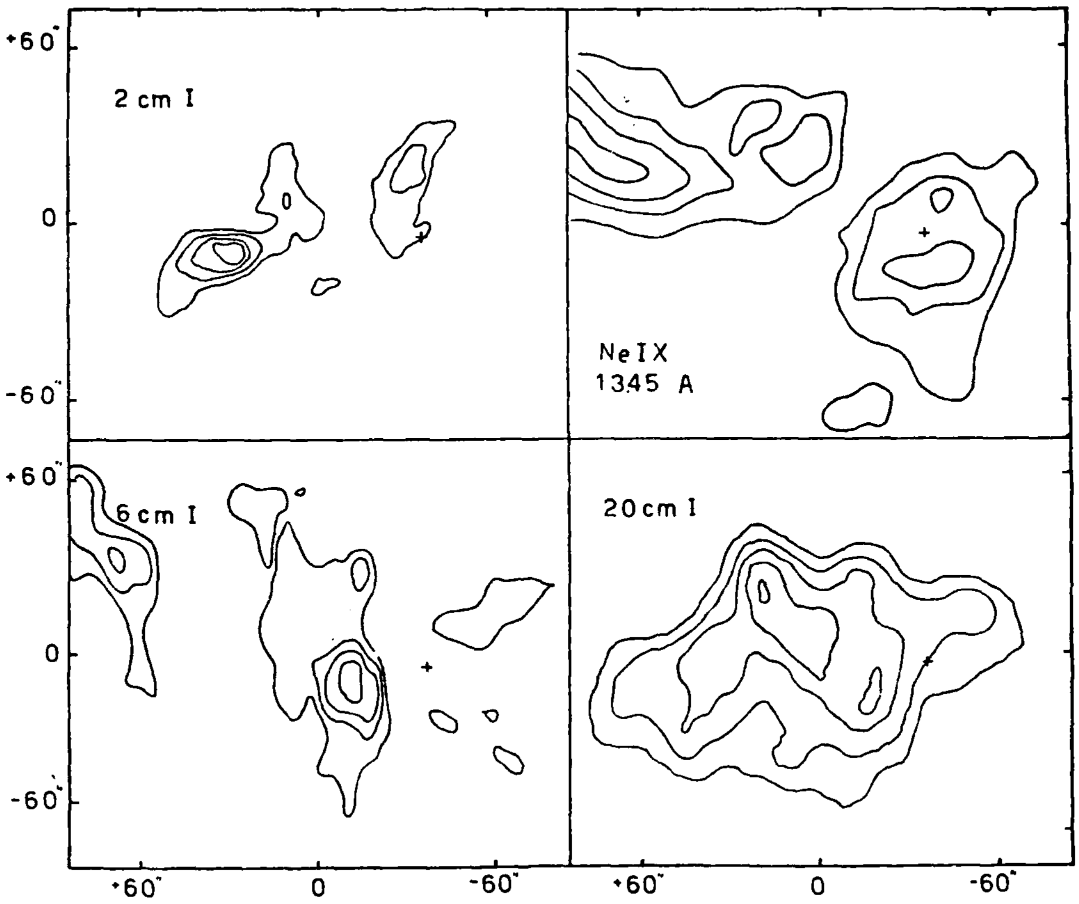

Figure 9. Radio wavelength synthesis maps of the total intensity, I, for AR 2490 at wavelengths of 2 cm (V.L.A.), 6 cm (W.S.R.T.) and 20 cm (V.L.A.) on June 11, 1980 together with an X.R.P. map at the Ne IX line (13.45 A) taken on the same day. Notice the structural changes when compared with Figure 8 which indicate an evolutionary time scale on the order of 1 day. Here the orientation is the same as Figure 8. The contours in the upper left hand corner of the 6 cm and C.R.P. maps refer to AR 2505 which was only partly in the field of view of the X.R.P. and is not discussed in this section.

Table 2. Maximum radio brightness temperature, T_B(max), observed on June 10 and 11 in the I and V maps.

Day	λ (cm)	T_B(K)	
		I	V
June 10	2	7.2×10^4	-
	6	2.2×10^6	6.0×10^5
	20	1.6×10^6	4.9×10^5
June 11	2	6.3×10^4	-
	6	2.5×10^6	5.0×10^5
	20	1.4×10^6	5.4×10^5

with bright Hα plage was, in fact, previously noticed by Felli, Lang and Willson[2] for another active region. Here we extend this to other radio wavelengths by noticing that a decrease in plage intensity at component B was associated with a decrease in the intensity of the radio emission of component B at 2 cm, 6 cm, 20 cm and X-ray wavelengths on June 11. Also on June 11, the emergence of new bright plage in the vicinity of component A was associated with an increase in its intensity at 2 cm, 20 cm and X-ray wavelengths. The interesting aspect of these correlated changes is that the Hα features, and also perhaps the 2 cm features, refer to the chromospheric level of the solar atmosphere above active regions, while the 6 cm and 20 cm features with brightness temperatures on the order of a million degrees refer to the low coronal levels of the atmosphere. The observed changes therefore indicate a close interplay between the morphology and energy content at the chromospheric and coronal levels of the solar atmosphere above active regions. The observed time scale of the changes is on the order of one day, and shorter time scales of less than a few hours can be ruled out because the radio wavelength synthesis maps refer to features which are stable over these shorter intervals. Examination of the Hα film indicates that the dominant Hα emission was stable for periods of at least six hours.

Figure 8 and 9 also indicate a westward displacement of the 6 cm and 20 cm features with respect to their 2 cm counterpart. The cross mark on each map refers to the same position on the solar surface, which is known with an accuracy of one second of arc. The displacements of the centroids at different wavelengths may be inferred from the angular separations from the cross mark. Using the mean solar coordinates of W26° and W39° on June 10 and 11, respectively, the observed displacements indicate that the 6 cm and 20 cm features have heights of between 1.4×10^9 cm and 4.4×10^9

cm above the 2 cm feature assuming that 1" = 7.25 x 10^7 cm at the solar surface. Felli, Lang and Willson[2] have previously inferred a height of 2 x 10^9 cm for the 6 cm plage-associated emission above the photosphere using a similar displacement with respect to a sunspot in another active region, and this is in agreement with 4 cm limb observations of yet another coronal condensation which indicates 4 cm emission at a height of 1.5 x 10^9 cm above the photosphere[60]. Moreover, solar limb observations at wavelengths between 2 cm and 4 cm with the RATAN-600 telescope indicate heights of between 0.5 x 10^9 cm and 7.5 x 10^9 cm above the photosphere depending on the wavelength and the region observed[61]. Thus, other observations are consistent with our interpretation of the observed westward displacements in terms of a projection effect caused by the greater height of the emission at longer wavelengths, and that the 2 cm emission is located close to the chromosphere at levels where the temperatures are about one hundred thousand degrees.

A representative Hα photograph taken on June 10 is compared with the June 10 synthesis map of total intensity at 6 cm wavelength in Figure 10. An ultraviolet map taken in a 13 min interval on June 10 at the C IV line at 1548 Å is presented in Figure 11. The 6 cm map has contours of equal brightness corresponding to 0.2, 0.4, 0.6 and 0.8 times the maximum brightness temperature, T_B(max), whereas the lowermost C IV contours are at 100 and 200 counts per second. On June 10 component A is not associated with any detectable Hα or C IV emission, suggesting that this component of the radio emission is not related to bright plage on June 10. The absence of 2 cm emission from component A on this day is consistent with the absence of C IV emission which also refers to temperatures of one hundred thousand degrees. As explained in greater detail later, we attribute the absence of C IV emission at component A to a large temperature gradient in this region which is dominated by a group of several sunspots. In marked contrast with component A, the westward component B of the radio emission shows a strong correlation with bright Hα plage on June 10. Both the bright core and the westward extension of the 2 cm emission shown in Figure 8 have Hα counterparts, for example, and the 6 cm contours are also correlated with Hα features. Moreover, the C IV emission is nearly perfectly correlated with the Hα emission. Of special interest is the emergence of bright Hα plage near component A on June 11 and the weakening of the Hα emission from component B on the same day. As previously mentioned, these changes seem to be respectively correlated with increased emission from component A at 2 cm, 20 cm and X-ray wavelengths and decreased emission from component B at 2 cm, 6 cm and 20 cm wavelengths.

---

60. Akhmedov, S.B., Bogod, V.M. and Gel'freikh, G.B. (1981), The results of a study of local source of active region McMath 15974 on S.M.Y. program using Ratan-600, preprint.

61. Gel'freikh, G.B. et al. (1981), Simultaneous optical and radio observations of a coronal condensation off the limb on November 19, 1980, preprint.

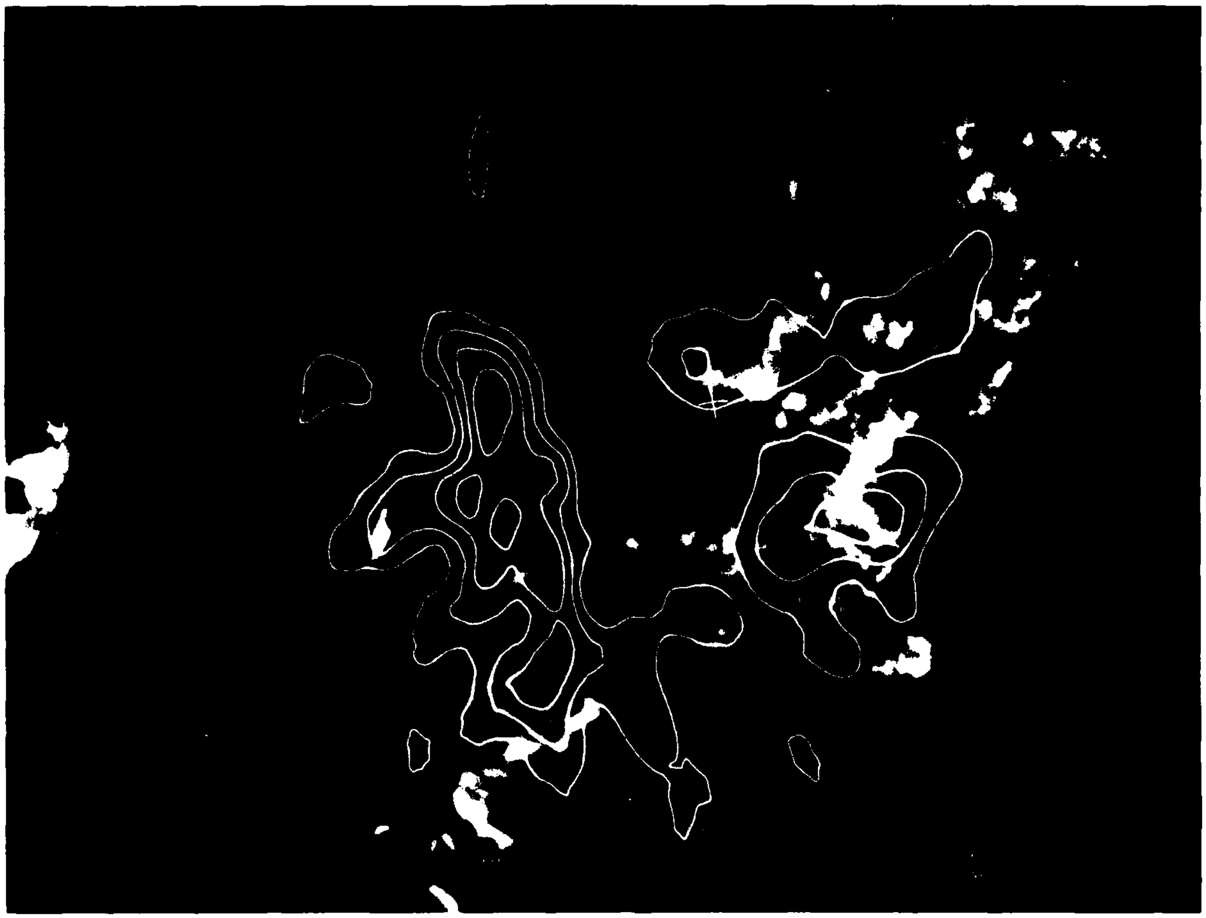

Figure 10. A comparison of an Hα photograph taken on June 10, 1980 with the W.S.R.T synthesis map of total intensity, I, at a wavelength of 6 cm. Notice that only the weaker components of radio emission are associated with the bright Hα plage. Here the solar north pole is up, west is to the right, and the angular scale can be inferred from Figure 8.

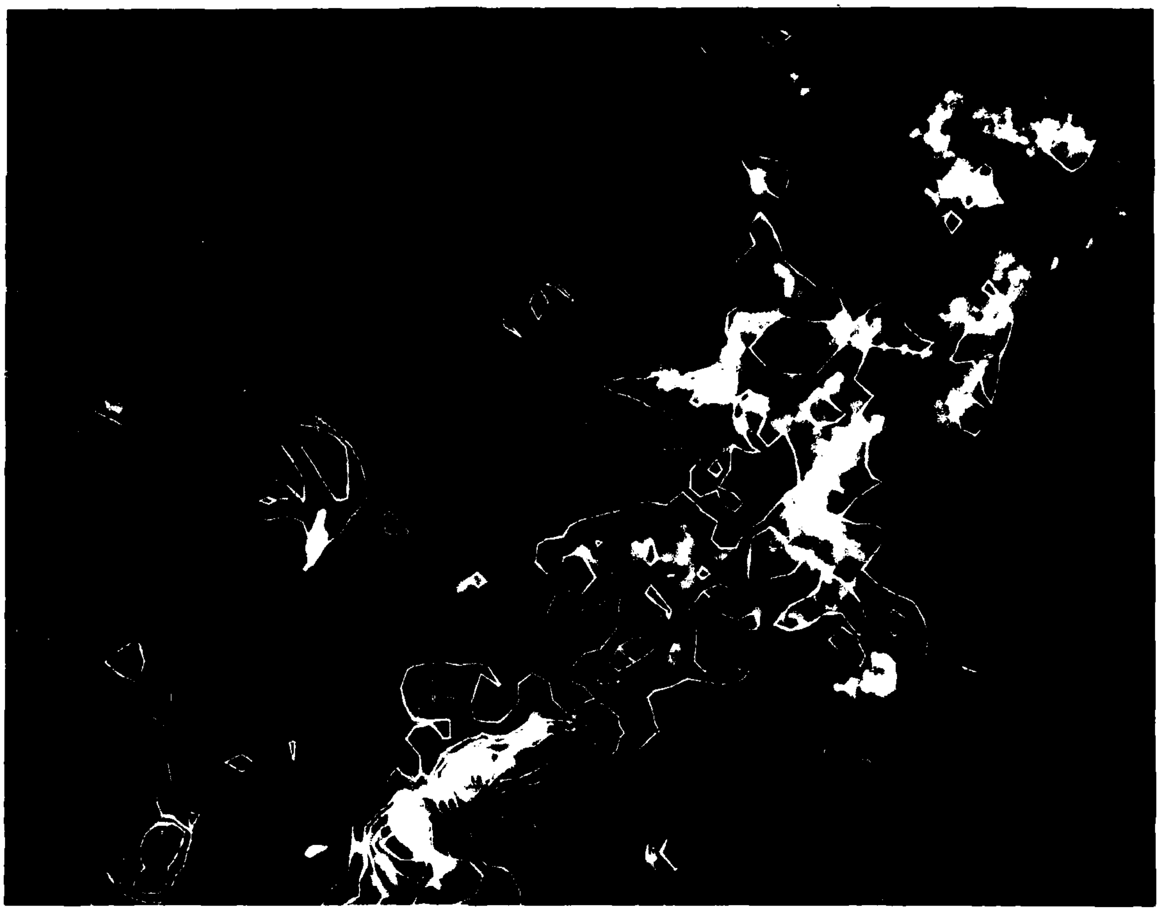

Figure 11. A comparison of an Hα photograph taken on June 10, 1980 with a U.S.V.P. (ultraviolet) map at the C IV line (1548 Å). Notice that the ultraviolet emission at the C IV line is well correlated with Hα plage. Here north is up, west is to the right, and the angular scale can be inferred from Figures 8 and 10.

As shown by Lang and Willson[38,39] and by Felli, Lang and Willson[2], the 6 cm synthesis maps of the Stokes parameter V act as coronal magnetograms for they delineate the magnetic structure at atmospheric levels with temperatures of a million degrees. According to Lang and Willson[39], the magnetic polarity, dipolar structure, and the shape and orientation of the 6 cm V maps of solar active regions agree with those seen in photospheric magnetograms. Both the Zeeman effect magnetograms and the circular polarization V maps refer to the longitudinal component of the magnetic field. The agreement between the longitudinal structure of the magnetic fields detected at different atmospheric levels suggests that the magnetic fields in solar active regions extend from the photosphere to the low solar corona with little radial divergence or loss of strength. All of these conclusions are further substantiated by our observations of AR 2490.

In Figures 12 and 13 the 6 cm I and V maps on June 10 are respectively compared with an offband Hα photograph showing the sunspot configuration on the same day together with the magnetic field polarity and strength in hundreds of gauss. The positioning of the radio maps on the photograph was determined by calculating the positions of the sunspots on the solar surface and converting these positions into the celestial coordinates of the synthesis maps at the same reference time. The V map has contours of equal brightness temperature corresponding to 0.2, 0.4, 0.6 and 0.8 times the maximum brightness temperature of 0.48×10^6 K. Dashed contours correspond to negative V values or right hand circular polarization with positive (north) magnetic polarity and magnetic lines of force pointing out of the solar surface. Solid contours correspond to positive V values or left hand circular polarization with negative (south) magnetic polarity and magnetic lines of force pointing into the solar surface. A careful comparison of the 6 cm V map with the 6 cm I map shown in Figure 8 indicates that the peaks of the two maps do not coincide, and that the degree of circular polarization varies throughout component A. A representative value for the degree of circular polarization $\rho_c = V/I$ is obtained by taking the ratio of the brightness temperatures at the position of peak V. The estimated uncertainty in determining ρ_c is ±10%. As illustrated in Figure 13, on June 10 component A has $\rho_c \sim 33 \pm 10\%$ at 6 cm wavelength, and the sense of circular polarization agrees with that of the underlying sunspots which delineate the overall magnetic structure at higher altitudes. Because the 6 cm maps and the offband Hα photograph refer to the same point on the solar surface, the comparison should demonstrate the projection effect caused by the greater height of the 6 cm emission. The expected westward displacement of the 6 cm emission of component A with respect to the sunspots is ∿ 6", providing an upper limit of 0.98×10^9 cm for its height

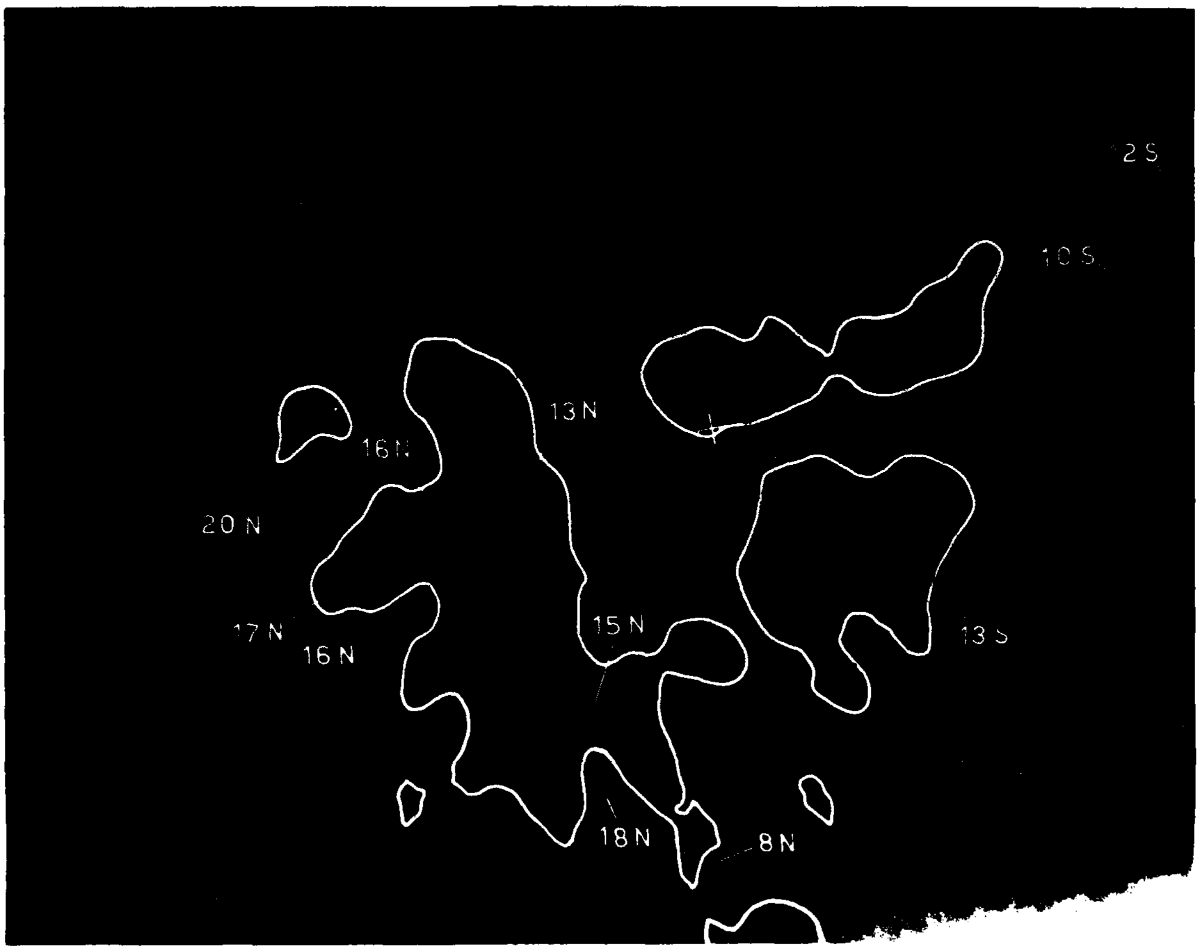

Figure 12. A comparison of an offband Hα photograph showing the sunspots on June 10, 1980 with the outermost contours of the 6 cm map of total intensity, I. The orientation is the same as in Figure 10. The magnetic polarity of the spots and their magnetic field strengths is hundreds of gauss; kindly provided by M.N. Gnevyshev of the Kislovodsk Station of the Pulkovo Observatory.

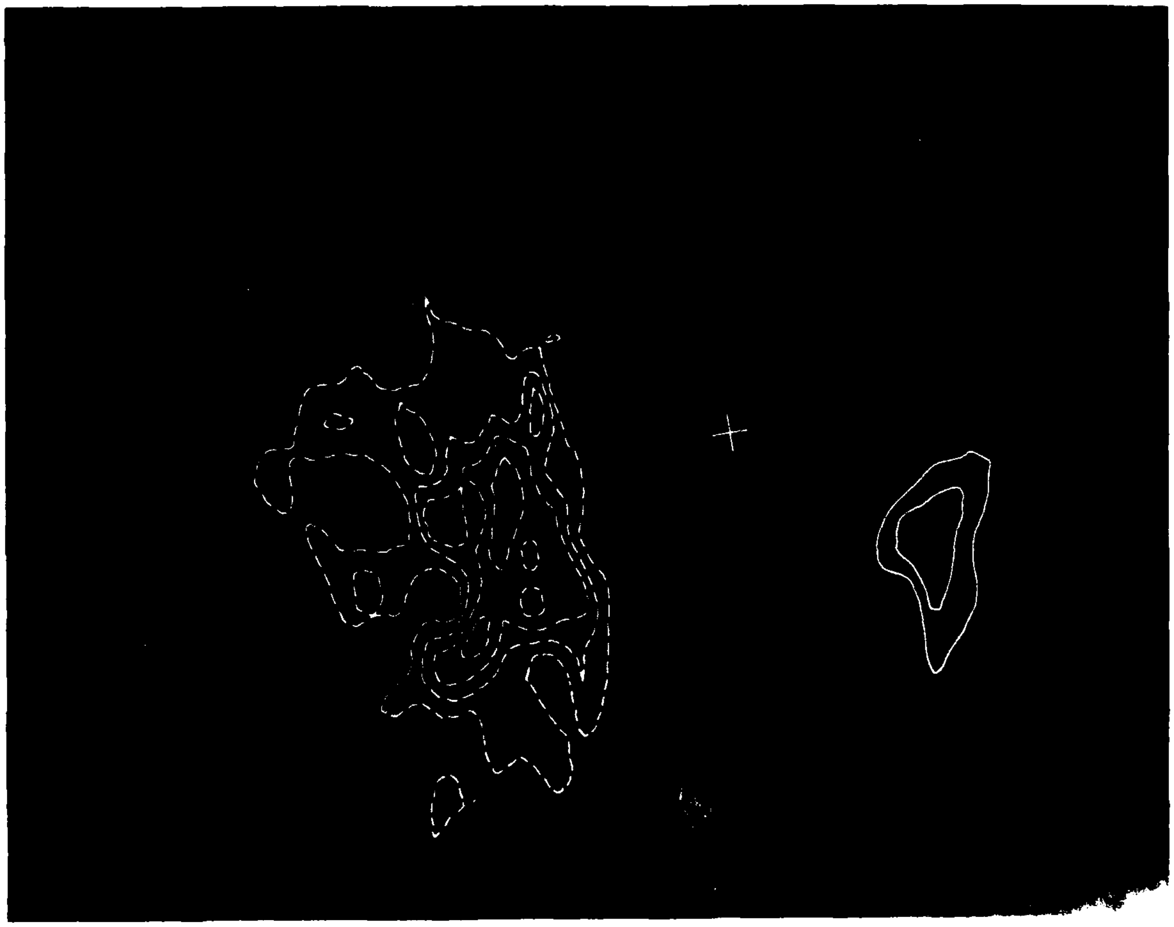

Figure 13. A comparison of an off-band Hα photograph showing the sunspots on June 10, 1980, with the 6 cm map of the Stokes parameter V. The orientation is the same as in Figure 12. Regions of positive magnetic polarity (north) correspond to negative V values (dashed contours and right hand circular polarization), and regions of positive magnetic polarity (south) correspond to positive V values (solid contours and left hand circular polarization).

above the sunspots, and suggesting that the 6 cm emission from component A lies at a lower height than the 6 cm emission of component B. There was no noticeable change in the circular polarization structure at 6 cm for component A between June 10 and 11. On June 10 component B had $\rho_c = +17 \pm 10\%$ at 6 cm wavelength, and the sense of circular polarization agreed with the small sunspot group lying to its west as well as with a diffuse region of south magnetic polarity which underlies the radio emission and is shown on photospheric magnetograms. Our observations of AR 2490 therefore reaffirm the conclusion that 6 cm V maps delineate the longitudinal magnetic structure at atmospheric levels corresponding to temperatures of millions of degrees, and that this structure is in general agreement with that determined by the Zeeman effect in the lower lying photosphere.

2.3.3 Emission Mechanisms for the Plage-Associated And Sunspot-Associated Components

Because the energy in soft X-ray spectral lines is produced by collisions of the observed ions with electrons, the relative intensities of the spectral lines of different ions give important information about the electron density, N_e, and the electron temperature, T_e, of the electrons in the emitting plasma. The observed X-ray photon flux, F, of a particular spectral line of a certain ion is given by

$$F = \frac{1}{4\pi D^2} \int N_n \, h\nu_{nm} \, A_{nm} \, dV \qquad (11)$$

where D is the Earth-Sun distance, N_n is the number density of ions in the upper level n, the photon energy of the spectral line is $h\nu_{nm}$, the spontaneous transition probability for the n-m transition is A_{nm}, the integral is taken over the emitting volume V, and the flux, F, is in units of erg cm^{-2} s^{-1}. Under the assumption that the level depopulation is balanced by collisional excitation from the ground state and that the large majority of ions are in the ground state,

$$F = \frac{h\nu_{mn}}{4\pi D^2} \int N_e \, N_i C_{mn} \, dV, \qquad (12)$$

where the rate of collisional excitation is given by Seaton[62] and Lang[40,41]

$$C_{mn} = \frac{h^2 \, N_e \Omega(m,n)}{\omega_m (2\pi m_e)^{3/2} (kT_e)^{1/2}} \exp\left(\frac{-h\nu_{mn}}{kT_e}\right)$$

$$= 8.6 \times 10^{-6} \, \frac{\Omega(m,n)}{\omega_m} \, \frac{N_e}{T_e^{\frac{1}{2}}} \, \exp\left(\frac{-h\nu_{mn}}{k\,T_e}\right) \, cm^3 \, s^{-1} \qquad (13)$$

---

[62] Seaton, M.J. (1964), The spectrum of the solar corona, Planetary Space Sci. 12:55-74.

where the collision strength $\Omega(m,n)$, the statistical weight ω_m, and the oscillator strength f_{nm} are related by

$$\frac{\Omega(m,n)}{\omega_m} = \frac{1.6\pi}{\sqrt{3}} \frac{f_{nm}E_1}{h\nu_{mn}} = 39.5 \frac{f_{mn}}{h\nu_{mn}} , \tag{14}$$

where in the numerical approximation we have assumed that $h\nu_{mn}$ is in e.v. and the binding energy of the hydrogen atom is $E_1 = 13.6$ e.v..

Assuming that all of the electrons are provided by hydrogen atoms, we have $N_e = N(H)$, the number density of hydrogen atoms, and we can express Eqs. (12) and (13) in terms of the relative abundance of the element N(E) to that of hydrogen and the relative abundance N(ion) of the ionization stage in question to that of the element. At the base of the coronal atmosphere where the temperatures are a few million degrees and the temperature gradients are not large, it is customary to remove the temperature dependent term from inside the integral to obtain a temperature dependent emissivity $E(T_e)$ per unit volume emission measure[63,64]. Assuming an Earth-Sun distance $D = 1.496 \times 10^{13}$ cm and combining coefficients in Eqs. (12) and (13) we obtain

$$F = E(T_e) \int N_e^2 \, dV, \tag{15}$$

where

$$E(T_e) = 1.6 \times 10^{-59} \, \nu_{mn} \frac{\Omega(m,n)}{\omega_m} \frac{N(E)}{N(H)} \frac{N(ion)}{N(E)} \quad \times$$

$$\frac{\exp(-h\nu_{mn}/kT_e)}{T_e^{\frac{1}{2}}} \quad \mathrm{erg\ cm\ s^{-1}}, \tag{16}$$

where the frequency of the spectral line ν_{mn} is in Hz and we have adopted the multiplicative normalization factor of about 0.78 used in extracting the temperature dependent term from the integral.

We have used the curves of $E(T_e)$ plotted as a function of T_e provided by Carole Jordan (private communication). The assumed logarithmic abundances of oxygen, neon and magnesium were log N(E) = 8.85, 7.95 and 7.60, respectively, on a scale in which the logarithmic abundance of hydrogen is log N(H) = 12.00. These do not differ from the cosmic abundances usually employed[46] by more than 3%. The relative abundances

---

[63] **Pottasch, S.R. (1964), On the interpretation of the solar ultraviolet emission line spectrum, Space Sci. Rev. 3:816-855.**

[64] **Mewe, R. (1972), Calculated solar X-radiation from 1 to 60 Å, Solar Phys. 22:459-491.**

N(ion)/N(E) were computed for the different stages of ionization at different electron temperatures by determining the equilibrium between collisional ionization and combined dielectronic and radiative recombination. For the ions considered here, O VIII, Ne IX and Mg XI, and the relevant temperature range of 1 to 4 million degrees, the values of N(ion)/N(E) were essentially the same as those given in Jordan[65]. These abundances and ionization populations were combined with the collision strengths specified by Eq. (13) to produce the curves of emissivity per unit volume emission measure for different electron temperatures.

The observed photon flux, F, in the spectral lines of O VIII, Ne IX and Mg XI were computed at the half intensity level for four maps taken on June 10 and for four maps taken on June 11. The observed counts per second at half maximum were converted into flux values by first subtracting the background, then dividing by the sensitivities of 0.4, 6.3 and 15.5 counts per seconds per photon cm^{-2} s^{-1} $arcsec^{-2}$ for O VIII, Ne IX and Mg XI respectively, then multiplying by the major and minor source half widths, θ_1 and θ_2, and finally multiplying by the photon energy of the spectral line. The ratios of the flux values for the three lines were then taken and compared with those inferred from Jordan's emissivity curves for different electron temperatures. In this way a total of twelve independent determinations of electron temperature could be made on each day to give the results shown in Table 3. The inferred electron temperature was then used with the observed line flux values to obtain a volume emission measure from the emissivity curves. These volume emission measures were then converted into line emission measure by dividing by the source area $\theta_1 \times \theta_2$ and assuming $1'' = 7.25 \times 10^7$ cm on the solar surface. A total of twelve independent measurements of the line emission measure on each day were then combined to give the results shown in Table 3. Here the errors are at the one standard deviation level, and they show that instrumental uncertainties from map to map give a 10% to 20% error in the determination of electron temperature and an uncertainty of a factor of between one and two for the line emission measure. We should point out here that there are still considerable uncertainties in the computations of emission measures from the X-ray data, for Allen and Dupree's ion equilibrium calculations[66] for Ne IX and Woolfson's values for the peak value of the emissivity function[67] of O VIII and Ne IX would lead to emission measures which are between two and three times those given in Table 3.

In addition to collisionally exciting ions which radiate spectral lines at

---

[65] Jordan, P. (1969), The ionization equilibrium of elements between carbon and nickel, M.N.R.A.S. 142:501-521.

[66] Allen, J.W. and Dupree, A.K. (1969), Calculations of ionization equilibria for oxygen,neon, silicon and iron, Ap. J. 155:27-36.

[67] Woolfson, C.J. (1981), Report to the Crimean solar maximum year workshop.

Table 3. Mean values of the major and minor axis of the X-ray source, $\Theta_1 \times \Theta_2$, electron temperatures, T_{e_2}, volume emission measure, $\int N_e^2 \, dV$ at half intensity level, and line emission measure, $\int N_e^2 \, dl$ as inferred from the observed line fluxes of the O VIII, Ne IX and Mg XI lines on June 10 and 11.

Source	$\Theta_1 \times \Theta_2$ (" x ")	T_e* (K)	$\int N_e \, dV$ (cm^{-3})	$\int N_e \, dl$* (cm^{-5})
Component B June 10	53 x 120	$3.53 \pm 0.36 \times 10^6$	9.5×10^{47}	$3.12 \pm 1.09 \times 10^{28}$
Component B June 11	49 x 81	$3.00 \pm 0.44 \times 10^6$	4.5×10^{47}	$2.72 \pm 1.97 \times 10^{28}$

---

* The errors are at the one standard deviation level for a total of twelve independent determinations. Allen and Dupree's (1969) calculation of the ion equilibrium of Ne IX and Woolfson's (1981) peak emissivity values for O VIII and Ne IX result in mean values of $\int N_e^2 \, dl$ which are two to three times higher than these.

X-ray wavelengths, the thermal electrons in a hot plasma also emit bremsstrahlung (braking radiation) when their trajectories are modified by the Coulomb fields of the ions. This bremsstrahlung is detected at radio wavelengths where observations provide independent estimates of the electron temperature, T_e, and the electron density, N_e. The observed maximum brightness temperature, $T_B(\max)$, observed at radio wavelengths (Table 2) provides a lower limit to T_e, for example, provided that bremsstrahlung is the dominant radiation mechanism in the observed region. Moreover, under this assumption the high observed degree of circular polarization, ρ_c, implies a bremsstrahlung optical depth, τ_B, less than unity, for an optically thick plasma with $\tau_B \geq 1$ would have no circularly polarized radiation. We have, in fact, used the observed brightness temperatures at half maximum level, $T_B(\max)/2$, to infer a representative optical depth using the relation

$$\tau_B = - \ln \left[1 - \left(\frac{T_B(\max)}{2\,T_e}\right)\right], \tag{17}$$

where the mean electron temperature, T_e, inferred from the X-ray measurements has been used for component B and a representative value of $T_e = 3.0 \times 10^6$ K has been used for component A. The derived values for optical depth are given in Table 4 together with the corresponding value of the emission measure, $N_e^2 dl$, which is given by the relation[40,41]

$$\int N_e^2 dl = \frac{102.19\, \nu^2\, T_e^{3/2}}{\ln(4.7 \times 10^{10}\, T_e/\nu)} \quad \mathrm{cm}^{-5} \text{ for } T_e > 10^5 \text{ K}, \tag{18}$$

where the observing frequency ν is in Hz, the T_e is in K, and the logarithmic factor becomes $\ln[4.954 \times 10^7\, T_e^{3/2}/\nu]$ when $T_e < 10^5$ K. Because the optical depth is very small at 2 cm wavelength, and also because the 2 cm radiation lies at about 10^9 cm below the 6 cm and 20 cm radiation, we compute the optical depth and emission measure at 2 cm assuming that it originates in the chromosphere-corona transition region where $T_e \approx 10^5$ K. Because the 2 cm brightness temperature can never exceed the local electron temperature the observed brightness temperatures indicate that the 2 cm emission must originate above the chromospheric levels where $T_e = 10^4$ K.

The interesting aspect of Table 4 is that the emission measures inferred for component B at 6 cm and 20 cm are consistent with those inferred from the X-ray observations, indicating that both the radio and X-ray radiation are the bremsstrahlung of the same hot plasma. The 2 cm emission measure from component B is consistent with the hypothesis that the 2 cm radiation is bremsstrahlung from the chromosphere-corona transition region, and the detailed morphology of this 2 cm radiation is, in fact, well correlated with the bright Hα plage originating in the chromosphere. Moreover, the intensity of component B at 2 cm, 6 cm, 20 cm and X-ray wavelengths

Table 4. Optical depth τ_b , emission measure $\int N_e^2 \, dl$, and longitudinal magnetic field strength H_ℓ inferred under the assumption that the radio emission is thermal bremsstrahlung at electron temperature T_e and that the degree of circular polarization, ρ_c , is due to a propagation effect.

Source	Wavelength (cm)	$T_B(\max)/2$ (K)	T_e (K)	τ_B	$\int N_e^2 \, dl$ (cm^{-5})	ρ_c (%)	H_ℓ (Gauss)
Component B	2	3.66×10^7	1.00×10^5	0.450	2.8×10^{28}	-	-
June 10	6	2.00×10^5	3.53×10^6	0.058	5.38×10^{28}	+17	153
	20	0.80×10^6	3.53×10^6	0.257	2.00×10^{28}	+40	108
Component B	2	1.25×10^4	1.00×10^5	0.133	8.40×10^{27}	<15	<400
June 11	6	1.50×10^5	3.00×10^6	0.051	3.71×10^{28}	<20	<100
	20	2.80×10^5	3.00×10^6	0.098	0.60×10^{28}	<15	< 40
Component A	2	3.15×10^4	1.00×10^5	0.38	2.40×10^{28}	<15	<400
June 11	6	0.67×10^6	3.00×10^6	0.252	18.5×10^{28}	-31	279
	20	0.70×10^6	3.00×10^6	0.266	1.64×10^{28}	-34	92
Component A	6	0.80×10^6	3.00×10^6	0.310	22.77×10^{28}	-33	297
June 10	20	0.30×10^6	3.00×10^6	0.105	0.65×10^{28}	-	-

decreased between June 10 and June 11, and this decrease was correlated with a weakening of the bright Hα plage. Thus, we conclude that the radiation from component B at Hα, radio and X-ray wavelengths is due to the bremsstrahlung of a plage-associated source. As we shall discuss in greater detail later, the order of magnitude excess of emission measure at 6 cm wavelength for component A, as well as the absence of detectable X-ray emission from this component on June 10, indicates that an additional radiation mechanism and opacity source is involved for this sunspot-associated source.

Before discussing the radiation mechanism of the sunspot-associated component, we interpret the observed circular polarization in terms of a propagation effect when the dominant radiation mechanism is bremsstrahlung. An electromagnetic wave passing through a magnetoionic medium is split into two normal waves, the ordinary, o, and the extraordinary, e, waves. Under the assumption of quasi-longitudinal propagation the degree of circular polarization, ρ_c, of the emergent radiation is given by Eqs. (8), (9) and (10). For optical depths $\tau_B < 1$ and frequencies $\nu >> \nu_H$, Eq. (8) can be written as

$$H_\ell = H \cos \theta = 54 \frac{\rho_c}{\lambda} , \tag{19}$$

where the degree of circular polarization ρ_c is given in percent and the wavelength λ is in cm. The observed degrees of circular polarization are given in Table 4 together with the value of the longitudinal magnetic field strength H_ℓ inferred from Eqs. (8) or (19). Values of $H_\ell \sim 100$ gauss are obtained at both 6 cm and 20 cm for the plage-associated component on June 10, whereas an upper limit of $H_\ell < 40$ gauss is obtained from the 20 cm observations of this component on June 11. These magnetic field strengths refer to plage-associated regions in the low solar corona where the temperatures are about a million degrees and the heights are around 2×10^9 cm above the photosphere. The measurements suggest that the magnetic field strengths of plage regions do not decrease significantly in height when passing from the photosphere through the chromosphere and into the low solar corona. This conclusion is supported by the measurement of $H_\ell \sim 250$ gauss using the polarized emission at 6 cm wavelength from a region of exceptionally bright plage[2], by optical wavelength observations of the Zeeman effect which indicate that longitudinal magnetic field strengths in the chromosphere do not differ significantly from those in the photosphere with value as large as 200 gauss for very bright plage[68], and by RATAN-600 measurements between 2 cm and 4 cm which indicate longitudinal magnetic field strengths of 40 and

---

[68] Severnyi, A.B. (1966), Magnetic fields at various depths in the solar atmosphere, Sov. Astr. AJ. 10:367-379.

80 gauss for a plage-associated region and a so-called coronal condensation lying between sunspots[69,61].

Of particular interest in Table 4 is the order of magnitude increase in emission measure for the sunspot-associated component A at 6 cm wavelength under the assumption that it is ordinary thermal bremsstrahlung. When this is combined with the failure to detect this component at 2 cm and X-ray wavelengths on June 10, we can only conclude that it is not radiating by the bremsstrahlung process. The distinction between the temperature and density structure of the coronal atmosphere above sunspots and plage has, in fact, been repeatedly emphasized by X-ray and E.U.V. observations which suggest low emission measures of $\int N_e^2 dl < 10^{27}$ cm^{-5} and cool loops with 10^5 K $\lesssim T_e \lesssim 10^6$ K above sunspots. As emphasized by Pallavicini et al.[36], Alissandrakis, Kundu and Lantos[35], Felli, Lang and Willson[2] and Pallavicini, Sakurai and Vaiana[37], the low electron density above sunspots requires an additional source of radio wavelength opacity due to gyroresonance absorption if radio emission with high brightness temperatures of $T_B(\max) \sim 10^6$ K are to be explained. This gyroresonant process was first introduced by Stepanov[20], Ginzburg and Zheleznyakov[21], and Zheleznyakov[22], and more detailed models have been developed by Lantos[26], Zlotnik[27,28] and Alissandrakis, Kundu and Lantos[35].

With typical values for the electron density, temperature, and magnetic scale height in the solar corona, gyroresonant absorption can only provide effective opacity while also producing circular polarization if it occurs at the third harmonic of the gyrofrequency, ν_H, at 6 cm wavelength. Moreover, because the optical depth only varies linearly with wavelength, it is also the third harmonic which is most important at 2 cm and 20 cm wavelength. This is essentially because the second harmonic is optically thick to both propagation modes and therefore cannot produce the high observed degrees of circular polarization, while the fourth and higher harmonics do not provide sufficient optical depth to give the high observed brightness temperatures. For the third harmonic the longitudinal magnetic field strengths of H_ℓ = 1,800, 600 and 180 gauss are respectively inferred for gyroresonant absorption at 2 cm, 6 cm and 20 cm wavelength.

We therefore attribute the extra opacity of the sunspot-associated component A to gyroresonant absorption at the third harmonic, and infer longitudinal magnetic field strengths of $H_\ell \sim 600$ gauss at atmospheric levels where $T_e \sim 10^6$ K above sunspots. This conclusion has been repeatedly emphasized by Lang and Willson[3,4,38,39], Alissandrakis, Kundu and Lantos[35], and Felli, Lang and Willson[2]. It is further

---

69. Bogod, V.M. and Gel'freikh, G.B. (1980), Measurements of the magnetic field and the gradient of temperature in the solar atmosphere above a flocculus using radio observations, Solar Phys. 67:29-46.

confirmed by the failure to detect gyroresonant absorption at 2 cm wavelength on June 10 from the sunspot-associated component. This means that the magnetic field strength was not high enough to provide sufficient optical depth, or that $H_\ell < 1{,}800$ gauss (or the third harmonic) at levels where $T_e = 10^5$ K to 10^6 K. This is consistent with $H_\ell = 1{,}300$ G to 1,800 G for the sunspots in the underlying photosphere. We incidently attribute the enhanced emission at 2 cm, 20 cm and X-ray wavelengths from component A on June 11 to the growth of plage-associated bremsstrahlung in this region. Observations at wavelengths between 2 cm and 4 cm independently confirm the fact that magnetic fields as strong as 2,000 G may penetrate the solar corona above sunspots[60,61].

The unexpected detection of strong magnetic fields with strengths between 600 and 1800 gauss in the coronal atmosphere above sunspots could be explained if the low solar corona lies close to the photosphere in the regions which overlie sunspots. This would place the detected radio emission with temperatures of $\sim 10^6$ K at low heights above sunspots where the magnetic fields would be stronger. According to this interpretation the failure to detect X-rays above sunspots is due to low values of electron density in these regions rather than low values of electron temperature. According to Noyes[70], observations of spectral lines at extreme ultraviolet wavelengths do, in fact, indicate that the temperature gradient is steeper and the transition zone is thinner above active regions. This is consistent with our failure to detect C IV emission lines in the sunspot associated component A, for the intensity of these lines varies inversely with the temperature gradient. Moreover, solar limb observations by Gelfreikh _et al_.[61] indicate that the height of the sunspot associated radio emission at 2 cm to 4 cm wavelength is an order of magnitude lower than the height of plage-associated or "coronal condensation" component (2×10^8 cm above the photosphere above sunspots as opposed to 2×10^9 cm for the plage-associated component). At first sight our interpretation would appear to be inconsistent with Foukal's [52,53] observations of cool loops (10^5 K $\leq T_e \leq 10^6$ K) which extend to high altitudes above sunspots; but these thin loops might well be embedded in extensive hotter material[71]. According to Pallavicini, Sakurai and Vaiana[37], the cool loops only occupy a small fraction (one third) of the umbra, and this is variable with time. We therefore argue that both hot ($T_e \sim 10^6$ K) and cool ($T_e \sim 10^5$ K) regions coexist in the coronal atmosphere above sunspots, and that the hot and cool regions may respectively extend to low ($h \sim 2 \times 10^8$ cm) and high ($h \sim 2 \times 10^9$ cm) altitudes above the photosphere. The hot material would enclose

---

[70] Noyes, R.W. (1971), Ultraviolet studies of the solar atmosphere, _Ann. Rev. Astr. Ap._ _9_:209-235.

[71] Levine, R.H. and Withbroe, G.L. (1977), Physics of an active region loop system, _Solar Phys._ _51_:83-101.

the cool loops and may occupy a substantial fraction of the region above sunspots. This intepretation has, in fact, been supported by the model of Brombozcz *et al.*[57] in which a steep temperature gradient exists for hot material above sunspot umbrae. According to this model, the hot material, which occupies 80% to 90% of the involved volume, has a shallow transition layer and reaches coronal values of $T_e = 2 \times 10^6$ K at $h = 3 \times 10^8$ cm.

2.3.4 Summary of the Two Component Model of Solar Active Regions

The multiple wavelength observations given here support Felli, Lang and Willson's[2] two component model of solar active regions in which the radio emission of one plage-associated component is due to ordinary thermal bremsstrahlung and the radio emission of the other sunspot-associated component has an additional contribution due to the gyroresonant emission of the thermal electrons. For the plage-associated component we conclude that:

a. The plage-associated emission exhibits detectable X-ray radiation which is spatially coincident with the radio emission.

b. The emission measures inferred from the relative intensities of the X-ray lines agree, within the observational uncertainties, with those inferred from the 6 cm and 20 cm radiation under the bremsstrahlung hypothesis. Emission measures of between 1×10^{28} cm^{-5} and 5×10^{28} cm^{-5} are inferred.

c. The 2 cm emission is well correlated with Hα emission and is due to bremsstrahlung at the chromosphere-corona transition region where $T_e = 10^5$ K.

d. The 6 cm and 20 cm radiation lie at about 2×10^9 cm above the photosphere where the $T_e = 2\text{-}4 \times 10^6$ K.

e. The longitudinal magnetic field structure in the low solar corona and the chromosphere-corona transition region is well correlated with the longitudinal magnetic field structure in the photosphere.

f. Longitudinal magnetic field strengths of $H_\ell = 100$ gauss are inferred for the low solar corona above the plage-associated component.

g. Changes in plage intensity and morphology are correlated with similar changes in the radio emission of the plage-associated component at 2 cm (where $T_e = 10^5$ K) and 6 cm (where $T_e = 2\text{-}3 \times 10^6$ K) wavelengths.

For the sunspot-associated component we conclude that:

a. The sunspot-associated component exhibits weak or undetectable X-ray radiation which is due to relatively low electron densities with $\int N_e^2 dl < 10^{27}$ cm^{-5}.

b. An additional source of opacity due to gyroresonant absorption is required to explain the 6 cm emission of the sunspot-associated component.

c. Longitudinal magnetic field strengths between 600 and 1800 gauss are inferred for the low solar corona (where $T_e = 2\text{-}3 \times 10^6$ K) above sunspots.

d. The high magnetic field strengths at levels where the temperature reaches a million degrees may be attributed to a thin transition zone above sunspots. This is consistent with observations of spectral lines at ultraviolet wavelengths. We suggest that million degree temperatures may be reached at altitudes of $h = 2 \times 10^8$ cm above sunspots.

e. Both cool ($T_e = 10^5$ K) and hot ($T_e = 10^6$ K) regions coexist in the coronal atmosphere above sunspots.

f. For this active region the sunspot associated component is the most intense component at 6 cm wavelength.

2.4 MULTIPLE WAVELENGTH, VERY LARGE ARRAY (V.L.A.) OBSERVATIONS OF SOLAR ACTIVE REGIONS

2.4.1 Introduction

Fan beam observations of solar active regions by Kundu[23,24] at 3.2 cm wavelength led to a core-halo model in which bright (10^6 K), polarized cores with angular sizes $\phi \overset{<}{\sim} 1.8'$ are associated with sunspots, and a weaker, extended halo is associated with bright plage. Kakinuma and Swarup[25] and Zheleznyakov[22] explained the intensity and polarization spectra of the sunspot-associated cores in terms of the gyroresonant emission of thermal electrons spiralling in the intense magnetic fields of sunspots. This interpretation was given added support when Lang[30] used interferometric observations at 3.7 cm wavelength to resolve the core sources which have angular sizes $\phi \sim 20''$ and degrees of circular polarization up to $\rho_c = 100\%$. The exceptionally high degrees of circular polarization are difficult to explain unless gyroresonant emission is invoked. This is because polarization by propagation effects would require intense magnetic fields which would make the region everywhere optically thick to gyroresonant absorption.

More recently, Alissandrakis, Kundu and Lantos[35] and Pallavicini, Sakurai and Vaiana[37] have noticed that X-ray observations indicate a low electron density in the coronal atmosphere above sunspots. This low density requires additional radio wavelength opacity due to gyroresonant absorption if radio emission with high brightness temperatures of $T_B \geq 10^6$ K are to be explained. Furthermore, plane parallel models of the temperature and density structure of the chromosphere-corona transition region have been used to predict the gyroresonance emission expected in the magnetic fields above sunspots[26,27,28]. These theoretical models predict that the total intensity of the emission at 6 cm wavelength will be enhanced above sunspot umbrae where the strong, radial magnetic fields allow the detection of the third harmonic of the gyrofrequency at the higher, hotter levels of the solar atmosphere were the temperature gradient is small. These enhancements have been confirmed by high resolution synthesis maps at 6 cm wavelength which indicate that longitudinal magnetic field strengths of $H_\ell \sim 600$ gauss are present in the solar atmosphere above sunspots where the temperatures are 10^6 K[34,35,38,39]. Final compelling evidence for gyroresonant emission at 6 cm wavelength above sunspots has come from recent observations of circularly polarized horseshoe structures which overlie sunspot penumbrae[3,55]. These horseshoe structures were predicted from the theory of gyroresonant absorption in the magnetic fields of individual sunspots[50].

The observations therefore seemed to provide convincing evidence that the 6 cm emission from solar active regions is enhanced above sunspot umbrae where brightness temperatures $T_B \geq 10^6$ K are explained by gyroresonant emission in magnetic fields with strength $H_\ell \sim 600$ gauss. Curiously enough, however, there has been more recent evidence that there are temperature depresssions above some sunspot umbrae at 6 cm wavelength. Felli, Lang and Willson[2] showed, for example, that the sunspot-associated emission is correlated with bright chromospheric plage rather than with sunspots. Kundu, Schmahl and Rao[51] similarly found that the most intense 6 cm sources in other active regions are associated with filamentary structures and magnetic neutral lines, and that they are not located directly over sunspots. This was attributed to the existence of cool material above the sunspot umbrae. In fact, Foukal[52,53] has argued several times that the cool "plumes" observed at E.U.V. wavelengths indicate that the coolness of sunspots persists up into the corona. Furthermore, Alissandrakis and Kundu[55] have reported the detection of a temperature depression at 6 cm wavelength above one sunspot umbra.

High resolution synthesis maps at 6 cm wavelength have therefore revealed a rich diversity of coronal structures which have a variety of optical wavelength counterparts, and which indicate that both temperature enhancements and temperature depressions might occur above sunspot umbrae. Because these single wavelength observations refer to a bewildering complexity of optical wavelength counterparts, morphological types, and magnetic field configurations, no clear cut generalizations are possible. We felt that a more fruitful approach from the physical point of view would result from multiple wavelength observations which refer to different levels within the solar atmosphere above active regions. In Section 2.4.2 we present V.L.A. synthesis maps at 2 cm, 6 cm and 20 cm wavelength and compare them with off-band Hα photographs. In Section 2.4.3 the 20 cm emission is interpreted in terms of the bremsstrahlung of coronal electrons trapped within magnetic loops; the 6 cm emission is interpreted in terms of the gyroresonant emission of thermal electrons spiralling in the legs of magnetic loops, and the 2 cm emission is interpreted in terms of either gyroresonant emission in the low solar corona or bremsstrahlung in the transition region.

2.4.2 Observations of Solar Active Regions at 2, 6 and 20 Centimeters Wavelength

We have used the Very Large Array (V.L.A.) to observe the solar active region AR 2505 on June 12, 1980 and the active region AR 2646 on Sept. 3 and 4, 1980. The position of AR 2505 on the solar surface was 14°S and 40°W at 13^h U.T. on June 12. The position of AR 2646 on the Sun's surface was 11°N and 9.5°W at 13^h U.T. on Sept. 3, and 11°N and 22°W at 13^h U.T. on Sept. 4. The incoming signal was sampled at two different wavelengths for alternate 15 minute periods throughout the eleven hours of observations each day. The wavelengths, λ, were λ = 2.0 cm and 6.2 cm (or 15016.0 MHz and 4866.3 MHz) on June 12 and Sept. 3, and λ = 6.2 cm and 20.75 cm (or 1446.1 MHz and 4866.3 MHz) on Sept. 4. In every case the bandwidth was 12.5 MHz. The individual antennae have a diameter of 25 m which provided beamwidths of 3.0', 9.3' and 31.1' at λ = 2 cm, 6 cm and 20 cm. On June 12 eleven antennae were used with distances from the array center ranging from 0.04 to 10.5 km and minimum and maximum spacings between interferometer pairs of 0.05 and 11.5 km. On Sept. 3 and 4 twenty-two antennae were used with distances from the array center ranging from 0.05 to 2.0 km and minimum and maximum spacings between interferometer pairs of 0.11 and 3.4 km. The average correlated flux of 55 and 242 interferometer pairs was respectively sampled on June 12 and Sept. 3 and 4. Both the left hand circularly polarized (LCP) signal and the right hand circularly polarized (RCP) signal were sampled every 10 s. These data were then calibrated, edited and time averaged over 60 s to make synthesis maps of the total intensity, I = (LCP+RCP)/2 and Stokes parameter, V = (LCP-RCP)/2.

On June 12 the data were calibrated by observing NRAO 150 for 5 min every 30 min, and by assuming that the flux density of this calibration was 10.5 and 10.2 Jy at λ = 2 and 6 cm, respectively. On Sept. 3 and 4 the data were calibrated by observing PKS 0923 + 392 for 5 min every 30 min, and by assuming that the flux density of this calibrator was 7.65, 7.36 and 8.53 Jy at λ = 2 cm, 6 cm and 20 cm respectively. The amplitude and phase of the correlated flux were calibrated according to the procedure described by Lang and Willson[38], together with a correction for the differences in the signal from high temperature noise sources detected in each polarization channel. At each wavelength the calibrated amplitude and phase for each polarization and every antenna pair were then taken to be the amplitude and phase of the source visibility function. The source intensity distribution was then obtained by Fourier transforming the calibrated data and using the CLEAN procedure developed by Clark[72]. On June 12, roughly 32,000 u-v components were used to obtain maps whose synthesized beams have half power widths of 2.4" x 3.4" (tilted at a position angle

---

[72] Clark, B.G. (1980), An efficient implementation of the algorith clean, <u>Astr. Ap</u>. <u>89</u>:377-381.

of 31°) at $\lambda = 2$ cm and 1.5" x 2.2" (tilted at a position angle of 26°) at $\lambda = 6$ cm. On Sept. 3 and 4 roughly 54,000 u-v components were used to obtain maps whose synthesized beams were not elongated, and which had half power widths of 2.3", 4.1" and 11.4" at $\lambda = 2$ cm, 6 cm and 20 cm, respectively.

The synthesis maps of the total intensity, I, of the radiation from AR 2505 are shown in Figure 14. Here the contours mark levels of equal brightness temperature corresponding to 0.2, 0.4, 0.6 and 0.8 times the maximum brightness temperature

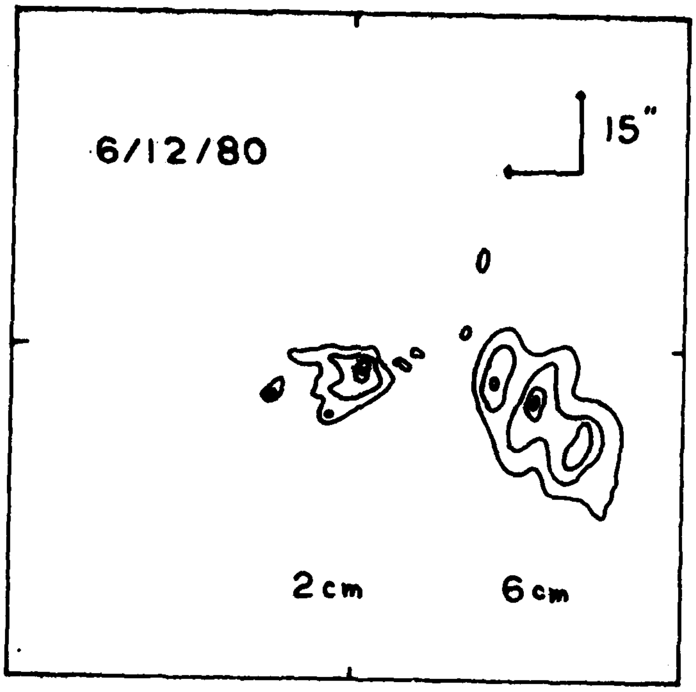

Figure 14. Synthesis maps of the total intensity I of the radiation from active region AR 2505 taken simultaneously with the Very Large Array (V.L.A.) at 2 cm (left) and 6 cm (right) wavelengths on June 12, 1980. The position of AR 2505 was near the west limb at about 14°S and 40°W. Here north is up, west is to the right, and both maps have the same phase center and the same angular scale denoted by the 15" arrows. Notice that the centroid of the 6 cm emission is displaced with respect to the centroid of the 2 cm emission by 40"±5" to the southwest. This is interpreted as a projection effect caused by the greater height of the 6 cm emission which lies at a height of $3.5 \pm 0.8 \times 10^9$ cm above the 2 cm emission.

of 5.1×10^4 K and 1.5×10^6 K at $\lambda = 2$ cm and 6 cm respectively. The enhanced 6 cm emission is associated with a group of three sunspots whose total angular extent is the same as that of the 2 cm emission. We attribute the broader extent of the 6 cm emission to the diverging magnetic fields of a dipolar loop which has one footprint in the group of sunspots, and a higher lying leg marked by the 6 cm emission. The centroid of the 6 cm emission is displaced with respect to the centroid of the 2 cm emission by 40"±5" to the southwest. This is interpreted as a radial, limbward displacement caused by the greater height of the 6 cm emission. Both the westward component of the displacement (35"±5") and the southward component (12"±5") indicate a height $h = 3.5 \pm 0.5 \times 10^9$ cm for the 6 cm emission above the chromosphere. Because this is comparable to the height of the plage-associated component of 6 cm emission in another active region[2], our observations provide no evidence for a difference in the thickness of the transition zone above sunspots and plage.

When allowance is made for the projection effect caused by a greater height, both the 2 cm and 6 cm emission lie above the group of sunspots. The low brightness temperatures $T_B \sim 10^4$ K and the low degree of circular polarization $\rho_c \sim 15\%$ of the 2 cm emission may be explained in terms of thermal bremsstrahlung in the transition region or low solar corona. The high brightness temperatures $T_B \sim 10^6$ K and the high degree of circular polarization $\rho_c \sim 60\%$ of the 6 cm emission are most easily explained as optically thin gyroresonance emission in the low solar corona. The strong radial magnetic fields of the sunspot umbrae allow the detection of the third harmonic of the gyrofrequency at higher, hotter levels in the solar atmosphere. Our 6 cm observations indicate longitudinal magnetic field strengths of $H_\ell \sim 600$ gauss (third harmonic at $\lambda = 6$ cm) at heights $h \sim 3.5 \times 10^9$ cm. This suggests that the radial magnetic field has decreased by a factor of three or four over an altitude which is comparable to the horizontal scale in the sunspots. Because the observations indicate relatively strong magnetic fields at relatively high altitudes where the temperatures reach 10^6 K, they cannot be explained by a relatively thin transition zone in which high temperatures occur close to sunspots where the magnetic fields are stronger[57].

Synthesis maps of the total intensity, I, of the 6 cm and 20 cm radiation of AR 2646 are shown in Figure 15. Here the contours mark levels of equal brightness temperature corresponding to 0.2, 0.4, 0.6, 0.8 and 1.0 times the maximum brightness temperatures of 2.9×10^6 K and 9.4×10^5 K at $\lambda = 6$ cm and 20 cm respectively. The two 6 cm sources lie above two sunspot groups of opposite magnetic polarity (see Figure 16). The regions of enhanced 6 cm emission have high brightness temperatures of $T_B = 1$ to 3×10^6 K and high degrees of circular polarization $\rho_c = 55$ to 70% which are most easily explained by gyroresonance emission in the low solar corona. The 6 cm emission marks the legs of a magnetic dipole where the longitudinal magnetic field strength $H_\ell \sim 600$ gauss and the temperatures reach millions of degrees. The two 6 cm sources mark the higher lying part of the dipole which joins the two sunspot groups. The unpolarized 20 cm emission ($\rho_c < 12\%$) is attributed to optically

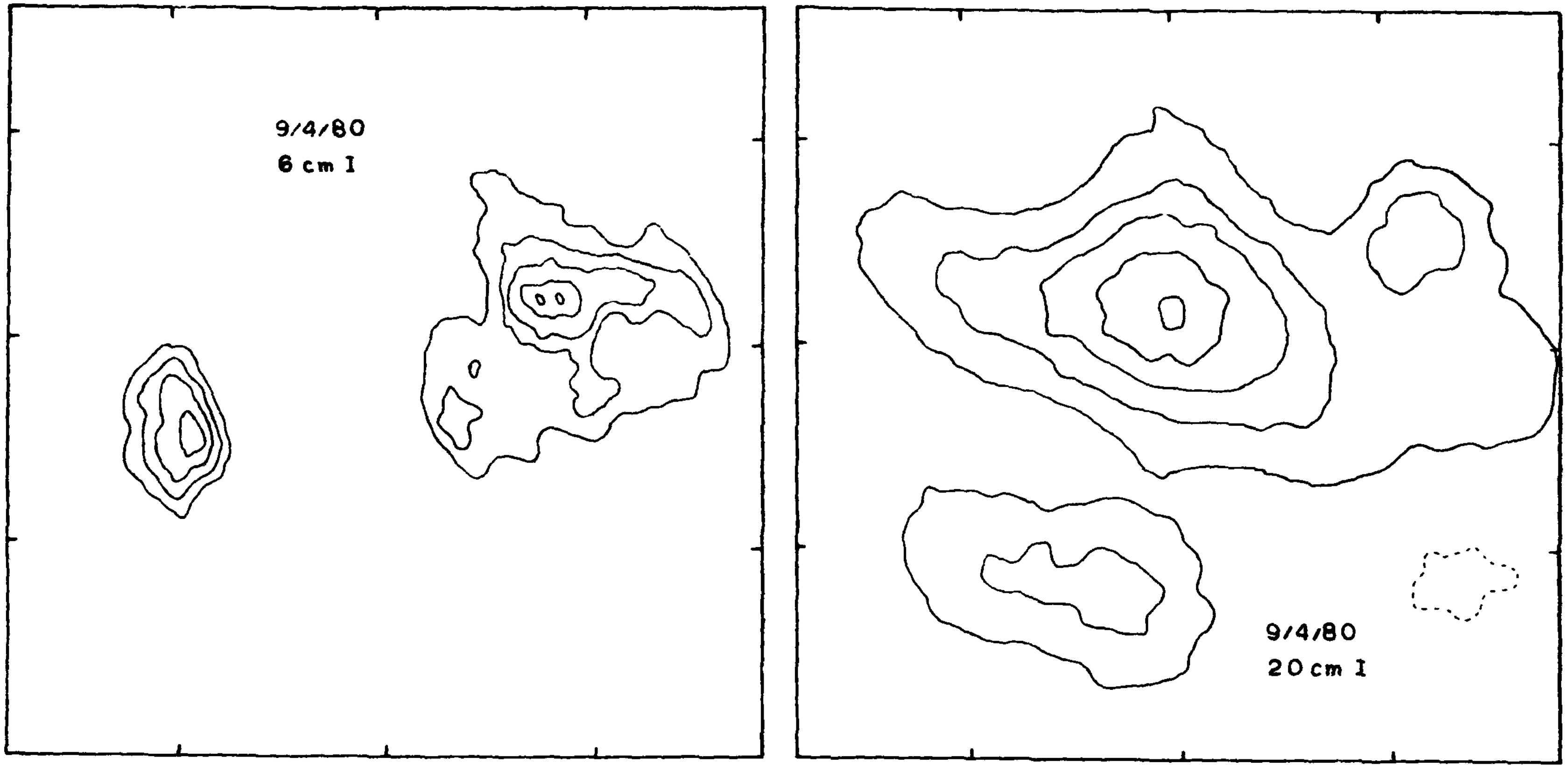

Figure 15. Synthesis maps of the total intensity I of the radiation from active region AR 2646 taken simultaneously with the Very Large Array (V.L.A.) at 6 cm (left) and 20 cm (right) wavelengths on Sept. 4, 1980. Here, north is up, west is to the right, and both maps have identical fields of view and the same angular scale denoted by the 60" spacing between the fiducial marks on the axes. The two 6 cm sources have brightness temperatures of $T_B \sim 10^6$ K, and lie above two sunspot groups of opposite magnetic polarity (see Figure 16). The larger 20 cm source is interpreted in terms of the optically thin bremsstrahlung of a coronal loop which joins the two sunspot groups. Notice that the peak brightness temperature at 20 cm is located near the central apex or top of the loop and that it has a value of 9.4×10^5 K.

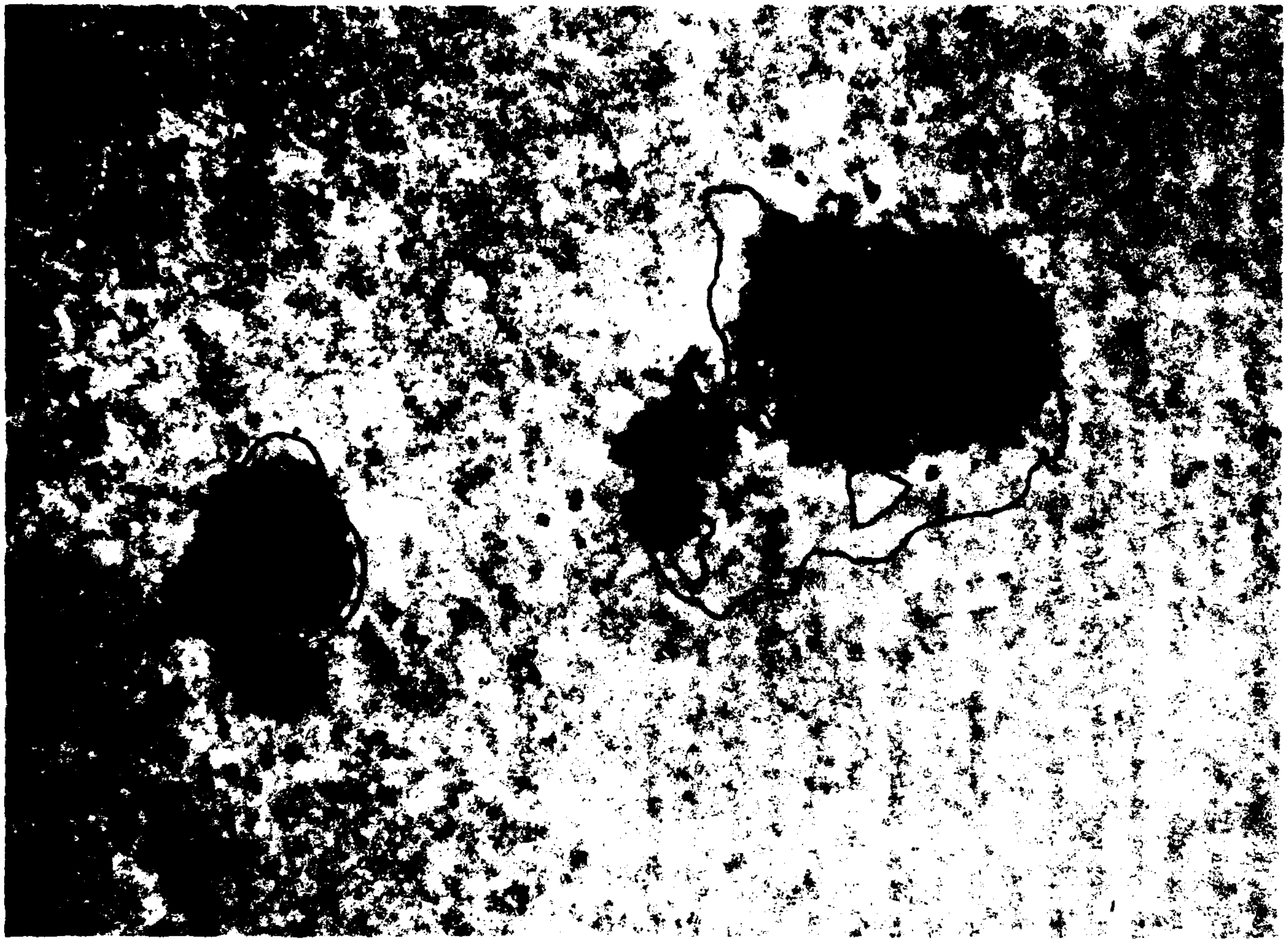

Figure 16. A V.L.A. synthesis map of the total intensity of the 6 cm radiation from active region AR 2646 on Sept. 4, 1980 (see Figure 15) is superimposed upon an offband Hα photograph of the same active region taken at the Ottawa River Solar Observatory at 18^h37^m U.T. on the same day. The largest component of 6 cm emission has an angular extent of about 60", but refer to Figure 15 for exact angular scale. The position of AR 2646 was near the Sun center at about 11°N and 20°W. Notice that the two components of 6 cm emission are displaced inwards and away from the sunspots as would be expected if they originate at higher levels in the magnetic loops which join the two sunspot groups. The 6 cm emission appears to be associated with both the sunspot umbrae and penumbrae.

thin bremsstrahlung near the apex of the coronal loop where the magnetic fields are mainly transverse to the line of sight. As discussed in greater detail later, we believe that the 20 cm emission is the radio wavelength counterpart of the ubiquitous coronal loops detected at X-ray wavelengths.

In Figure 16 the 6 cm emission of AR 2646 on Sept. 4 is superimposed on an off-band Hα photograph (Hα +1.4 Å) taken on the same day. The uncertainty in this superposition is no greater than 10". The two main groups of sunspots have opposite magnetic polarity, and the circular polarization of the 6 cm emission corresponds to the extraordinary mode of wave propagation in magnetic fields with the same polarity as the underlying sunspots. The two components of the 6 cm emission are displaced inwards and away from the sunspots as would be expected if they mark the higher lying legs of the magnetic dipole which joins the two sunspot groups. To a first approximation we may assume that these groups of sunspots mark the feet of a loop of circular form whose radius $r \sim 70'' \sim 5.0 \times 10^9$ cm, where $1'' \sim 725$ km on the solar surface. We may then infer the heights of the 6 cm components from their inward displacements of $x \sim 25''\pm5'' \sim 1.8\pm0.4 \times 10^9$ cm. We obtain $h = r \sin\{\cos^{-1}[(x-r)/r]\} = 3.8\pm0.4 \times 10^9$ cm above the solar photosphere. This provides additional evidence that magnetic fields of $H_\ell \sim 600$ gauss exist at heights of $h \sim 3.5 \times 10^9$ cm above sunspots where the temperatures $T \sim 10^6$ K.

The inward displacement of the two main components of 6 cm emission with respect to the underlying sunspots is also shown in Figure 17 which compares the 6 cm map of AR 2646 on Sept. 3 with an offband Hα photograph (Hα -1.0 Å) taken on the same day. The positional uncertainty in this comparison is no greater than 10". Here the contours mark levels of equal brightness temperature corresponding to 0.2, 0.4....1.0 times the maximum brightness temperature of 2.2×10^6 K. The two peaks found in the largest component of the 6 cm emission probably mark the higher lying parts of the outwardly-diverging magnetic flux tubes which join the two umbrae that are separated by a light bridge. A comparison with Figure 16 indicates that changes in the sunspot configuration produced low level changes in the 6 cm emission; but that the more intense dipolar features remain relatively stable during the two days.

The synthesis maps of the total intensity, I, and the Stokes parameter, V, of the dominant component AR 2646 are shown in Figure 18. The contours of the I maps at 6 cm (map A) and 2 cm (map B) mark levels of equal brightness temperature corresponding to 0.2, 0.4...1.0 times the maximum brightness temperatures of 2.2×10^6 K and 1.6×10^5 K, respectively. The contours of the V maps at 6 cm (map C) and 2 cm (map D) mark levels of equal brightness temperature corresponding to 0.2, 0.4...1.0 times the maximum brightness temperatures of 1.4×10^6 K and 1.3×10^5 K, respectively. The dashed contours of the V map refer to regions of negative, right handed circular polarization and positive (north or white) magnetic polarity. The sense of

Figure 17. A V.L.A. synthesis map of the total intensity of the 6 cm radiation from active region AR 2646 on Sept. 3, 1980, is superimposed upon an offband Hα photograph of the same active region taken at the Ottawa River Solar Observatory at 15^h35^m U.T. on the same day. The field of view and angular scale are the same as those in Figure 16. The position of AR 2646 on this day was also near the Sun center at about 11°N and 10°W. A comparison with Figure 16 indicates that changes in the 6 cm emission are associated with changes in the sunspot configuration, but that the outermost components of 6 cm emission remain displaced inwards and away from the two main sunspot groups.

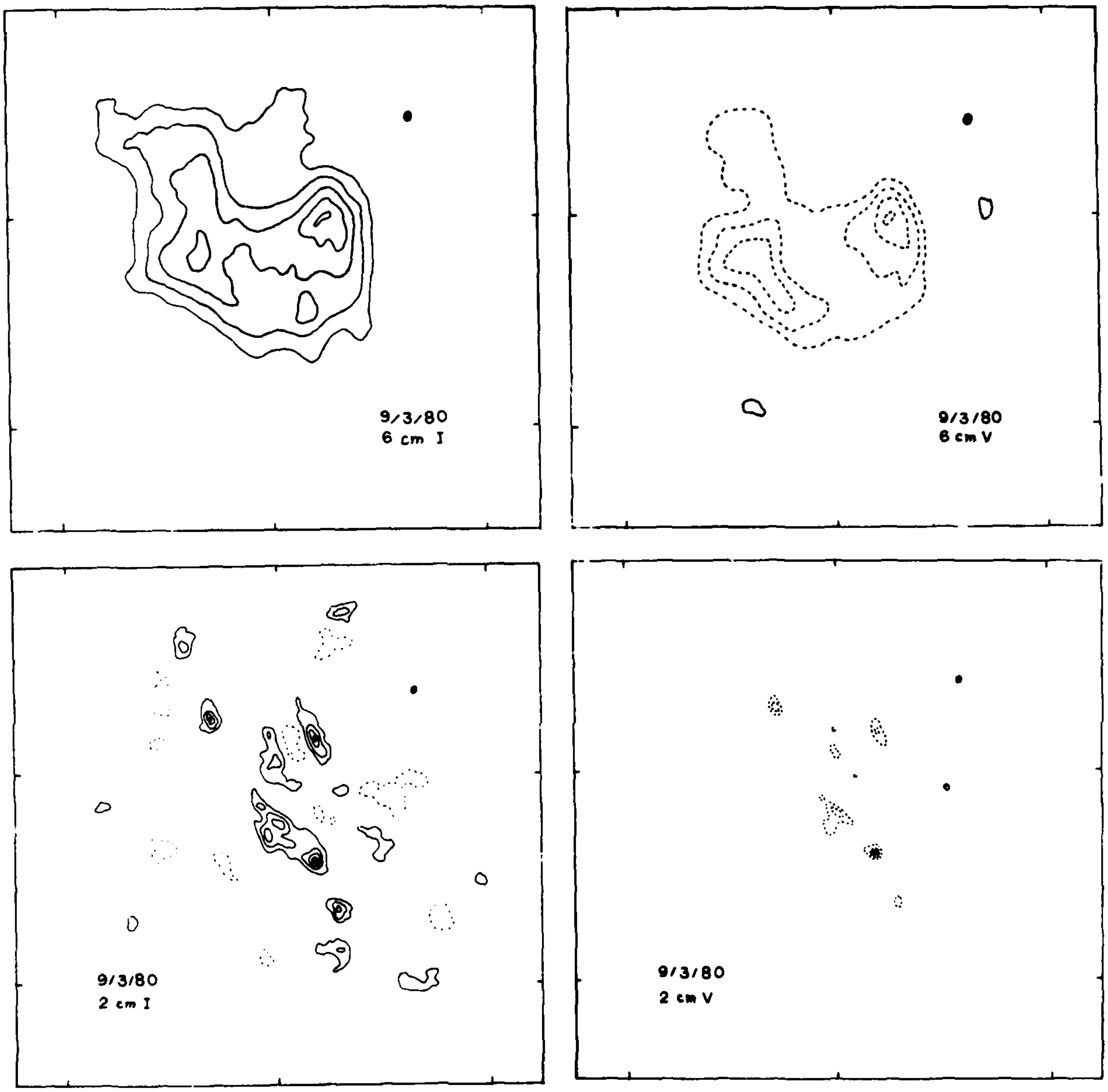

Figure 18. V.L.A. synthesis maps of total intensity I at 6 cm (A) and 2 cm (B), and the Stokes parameter V at 6 cm (C) and 2 cm (D). The black dot denotes the size of the synthesis beam, and all of the maps have the same field of view with angular scales denoted by the 60" spacing between the fiducial marks on the axes. Notice that both the 2 cm and 6 cm emission are highly circularly polarized (67% to 86%); but that the emission at 2 cm wavelength is broken up into tiny hot spots with brightness temperatures $T_B \sim 10^5$ K.

the circular polarization at both 2 cm and 6 cm wavelengths corresponds to the extraordinary mode of wave propagation in a magnetic field which has the same polarity as the magnetic field in the underlying photosphere. The degrees of circular polarization at 2 cm and 6 cm are similar, with $\rho_c \sim 87\%$ and $\rho_c \sim 67\%$, respectively. The spatial configurations of the 2 cm and 6 cm emissions are, however, different. The peaks of the 6 cm emission have angular sizes of $\phi \sim 20''$ and appear to be the coronal counterparts of the two sunspot umbrae, while the two most intense 2 cm sources have angular sizes of $\phi \sim 5''$ and the 2 cm hot spots do not seem to have any special relation with the sunspots. One of these 2 cm hot spots did, however, coincide, within the uncertainty of the alignment (10"), with the light bridge which separates the two westernmost sunspots. Curiously enough, Hα flares were emitted from the light bridge on Sept. 3, even though the magnetic field has the same polarity on each side of the bridge.

2.4.3 Emission Mechanisms of Active Region Loops at Centimeter Wavelengths

2.4.3.1 Coronal loops at 20 cm wavelength

We have observed a looplike structure at 20 cm wavelength which extends across two groups of sunspots of opposite magnetic polarity, and which is most intense in the central regions between them. The 20 cm radiation is interpreted in terms of the bremsstrahlung of thermal electrons which are trapped within a single wide loop or an arcade of loops which join the two regions of opposite magnetic polarity. The fact that the 20 cm emission connects two regions whose brightness temperatures exceed 10^6 K at 6 cm wavelength suggests that the electron temperature of the higher lying 20 cm loop has coronal values of $T_e = 2 \times 10^6$ K. We can use this value together with the average brightness temperature $T_B \sim 4.7 \times 10^5$ K of the 20 cm loop to infer an optical depth $\tau = -\ln[1 - (T_B/T_e)] = 0.3$. With these values of optical depth and electron temperature, the bremsstrahlung formulae given in Eq. (18) indicate an emission measure of $\int N_e^2 dl \sim 10^{28}$ cm^{-5}. This emission measure is comparable to those inferred from X-ray measurements of coronal loops[48]. The semilength of the 20 cm emission has the value of $L \sim 5 \times 10^9$ cm, which is also comparable to the X-ray coronal loops (L is half the total extent of the loop measured along the magnetic field). The electron density is $N_e = [\int N_e^2 dl/L]^{\frac{1}{2}} \sim 1.5 \times 10^9$ cm^{-3} and the loop pressure $p = 2\, kT_e N_e = 0.83$ dyn cm^{-2} (where Boltzmann's constant $k = 1.38 \times 10^{-16}$ erg °K^{-1}). The values for the N_e and p of the 20 cm loop are also comparable to those of the X-ray coronal loops[73], and the 20 cm loop parameters satisfy the scaling relationship $T_e(\max) \sim 1.4 \times 10^3 (pL)^{1/3}$ for X-ray loops. The 20 cm emission may

---

[73] **Rosner, R., Tucker, W.H. and Vaiana, G.S. (1978), Dynamics of the quiescent corona, Ap. J. 220:643-665.**

therefore be interpreted as optically thin bremsstrahlung of a hot, dense plasma trapped within an arcade of coronal loops whose physical parameters are similar to those detected at X-ray wavelengths. The fact that the 20 cm emission exhibits no detectable circular polarization may be attributed to the fact that the bremsstrahlung comes mainly from the central regions of the coronal loop where the magnetic fields are mainly transverse to the line of sight. There has incidentally been one previous report of the detection of a low lying coronal loop at 6 cm wavelength[74,75], but these observations were confused by the gyroresonance emission of the sunspots which becomes negligible at the longer 20 cm wavelength.

When the observations given in this section are combined with our more recent V.L.A. observations of hot ($\sim 10^6$ K) coronal loops at 20 cm wavelengths[7], we may conclude that we have discovered the radio wavelength counterpart of the coronal loops detected at X-ray wavelengths. It is the ubiquitous coronal loops which appear to be the dominant structural element in the low solar corona and which seem to outline the three dimensional configuration of the coronal magnetic field. Future V.L.A. observations at 20 cm wavelength may specify the temperature and density structure of coronal loops with a few seconds of arc angular resolution. The evolution of coronal loops can be investigated by taking V.L.A. synthesis maps at intervals of one hour or less, and this may lead to the detection of temperature enhancements which are expected during preflare activity. Our discovery therefore opens up the possibility of using 20 cm synthesis maps to investigate the detailed structure, evolution and preflare activity of coronal loops. Synthesis maps of several hours duration may be used to study the relatively stable loops detected at X-ray wavelengths, while maps of shorter duration may be used to study the short-lived, cooler loops.

2.4.3.2 Legs of dipolar loops at 6 cm wavelength

We have detected intense 6 cm emission which marks the legs of a dipolar loop whose two footpoints are delineated by lower-lying sunspots of opposite magnetic polarity. In contrast to the reports of Alissandrakis and Kundu[55] and Kundu, Schmahl and Rao[51], we do not observe a temperature depression in the 6 cm emission above sunspot umbrae. The brightness temperatures above the umbrae are instead enhanced with values of $T_B \sim 10^6$ K. This is in agreement with the observations of Lang and Willson[38,39] and Alissandrakis, Kundu and Lantos[35]. The high brightness temperatures

---

[74] Velusamy, T. and Kundu, M.R. (1980), Observations of solar active regions at 2 and 6 cm wavelengths with three arc second resolution, I.A.U. Symposium No.86: Radio Physics of the Sun, M.R. Kundu and T.E. Gergely, Eds., Reidel, Dordrecht, pp.105-108.

[75] Kundu, M.R. and Velusamy, T. (1980), Observation with the V.L.A. of a stationary loop structure in the sun at six cm wavelength, Ap. J. Lett. 240:L63-L67.

and the high degrees of circular polarization of ρ_c = 55% to 70% indicate that the 6 cm radiation is due to gyroresonant emission in the solar atmosphere overlying sunspots (see Section 2.4.1 and references therein). The quasi-longitudinal expression for the optical depth due to gyroresonant absorption is given by[27,29,30]

$$\begin{aligned}
\tau_2 &= 2.985 \times 10^{-22}\, \lambda N_e T_e L_H \sin^2\theta(1\pm\cos\theta)^2 \text{ for } n = 2 \\
\tau_3 &= 3.829 \times 10^{-31}\, \lambda N_e T_e^2 L_H \sin^4\theta(1\pm\cos\theta)^2 \text{ for } n = 3 \\
\tau_4 &= 7.224 \times 10^{-40}\, \lambda N_e T_e^3 L_H \sin^3\theta(1\pm\cos\theta)^2 \text{ for } n = 4,
\end{aligned} \tag{20}$$

where the frequency of the radiation is given by $\nu = 2.8 \times 10^6\, n\, H_\ell$ for the n^{th} harmonic in a longitudinal magnetic field of strength H_ℓ, the wavelength is λ, the electron density and electron temperature are N_e and T_e, respectively, the scale height for the variation of the magnetic field is L_H, the angle between the line of sight and the magnetic field is θ, and the + and - signs respectively refer to the extraordinary and ordinary modes of wave propagation. The 20 cm observation discussed in the previous section indicates that the coronal loop which connects the 6 cm sources has $N_e \sim 10^9$ cm^{-3}, $T_e \sim 10^6$ K, and $L_H \sim 10^9$ cm. Using these parameters in Eqs. (20) together with λ = 6 cm, we see that the second harmonic (n = 2) is everywhere optically thick, and that the fourth harmonic (n = 4) is an ineffective opacity agent. The million degree brightness temperatures require enough opacity to rule out the fourth harmonic, while the circular polarization, which requires an optically thin condition, is most easily accounted for by the third harmonic emission which becomes optically thin at levels where $T_e \sim 10^6$ K. Furthermore, the second harmonic must not provide equally bright ordinary mode radiation, either because the field strength is inadequate, or the second harmonic level is below the corona where $T_e << 10^6$ K. We therefore conclude that the 6 cm radiation is due to gyroresonant emission at the third harmonic (n = 3) which corresponds to a longitudinal magnetic field strength of H_ℓ = 600 Gauss.

Our observations also show no evidence for a cool region in the coronal atmosphere above sunspot umbrae. At first sight this would seem to contradict Foukal's[52, 53] argument that the cool "plumes" detected at E.U.V. wavelengths project upwards into the solar corona to form cool loops. Static cool loops are unstable, however, and the spikey cool structure observed above sunspot umbrae has short lifetimes of tens of minutes[58]. Furthermore, the cool "plumes" fill only a fraction of the umbrae area and change considerably with time[37]. The cool loops actually coexist with hot loops which have lifetimes as long as days. Because our 6 cm synthesis maps refer to observations averaged over a 12 hour period, we would only expect to detect the more stable, long-lived hot loops. In fact, we are somewhat skeptical of reports of the detection of cool material above sunspot umbrae in 6 cm synthesis maps[51,55], for they imply unexpectedly long lifetimes for the cool material. The cool loops might be more effectively detected in "snapshot" maps using 6 cm observations lasting an hour or less.

2.4.3.3 Hot spots at 2 cm wavelength

The 2 cm emission from AR 2505 has low brightness temperatures characteristic of the transition region (10^4 to 10^5 K), while the 6 cm emission has high brightness temperatures characteristic of the corona (1 to 3×10^6 K). Furthermore, the 2 cm emission from AR 2505 is, within the uncertainties of measurement, spatially coincident with the underlying sunspots, and it has no detectable circular polarization. The 6 cm emission, on the other hand, was displaced from the sunspots and had a high degree of circular polarization ($\rho_c \sim 60\%$). These differences suggest that we are dealing with two different emission mechanisms in this case. The 2 cm radiation may be attributed to bremsstrahlung of thermal electrons in the transition region, while the 6 cm radiation is attributed to gyroresonant emission in the corona. Nevertheless, the overall bright 2 cm region in Figure 14 was observed with relatively poor UV coverage, and it could be composed of several highly polarized bright spots of the type which were detected in AR 2646 (Figure 18) when the array configuration permitted the sampling of many more UV components.

The unexpectedly high degrees of circular polarization ($\rho_c \sim 87\%$) of the 2 cm hot spots observed in AR 2646 suggest gyroresonant emission. The observed polarization could be explained by gyroresonant emission in the low solar corona with longitudinal magnetic field strengths $H_\ell \sim 1800$ gauss ($n = 3$) provided that the electron density is high ($N_e \sim 10^{10}$ cm^{-3}). As pointed out by George Dulk, the appropriate scale length, L_H, for gyroresonance emission in the transition region is a factor of 10^2 or 10^3 smaller than it is in the corona, and for this reason transition region emission is much less plausible. Nevertheless, comparable polarization may occur under imaginable conditions in both the low solar corona ($T_e \sim 5 \times 10^5$ K, $N_e \sim 10^{10}$ cm^{-3}, $L_H \sim 10^9$ cm, $H_\ell \sim 1{,}800$ gauss, $n = 3$) and the transition region ($T_e \sim 10^5$ K, $N_e \sim 10^{11}$ cm^{-3}, $L_H \sim 10^6$ cm, $H_\ell \sim 2{,}700$ gauss, $n = 2$). The fact that the 2 cm hot spots are not found everywhere over the sunspots additionally argues against transition region emission, however, for one would expect strong magnetic fields everywhere over the umbrae. An alternative possibility is that the hot spots are transient brightenings similar to those which are often seen at Hα wavelengths. In fact, one of the hot spots did coincide with a light bridge in which Hα flares were emitted during the observation period. It is also possible that the 2 cm hot spots mark the legs of warm ($\sim 10^5$ K) loops.

2.5 CORONAL LOOPS AT 20 CENTIMETER WAVELENGTH

2.5.1 Introduction

Observations of the solar corona at visual wavelengths in the 1940s led to the discovery of arch-shaped features whose intense emission lines were attributed to density enhancements in the coronal atmosphere overlying sunspots[76,77,78]. These "coronal condensations" were rediscovered in the subsequent decade when solar radio emission was detected with brightness temperatures of millions of degrees[10,11]. Although the emission at shorter radio wavelengths was subsequently attributed to gyroresonance emission in the intense magnetic fields of sunspots, the longer wavelength emission had to be due to the bremsstrahlung of thermal electrons in dense "coronal condensations". This was particularly true for the emission at 20 cm wavelength which exhibits no detectable circular polarization and has brightness temperatures which correspond to coronal electron temperatures of $T_e = 2$ to 4×10^6 K[18,19,79]. Of course, only the larger 20 cm sources with angular sizes of a few arc minutes could be resolved in only one direction with these early fan beams. Nevertheless, subsequent observations using the Westerbork Synthesis Radio Telescope (W.S.R.T.) with an angular resolution of 21" x 61" have reconfirmed the old conclusion that the 20 cm emission associated with solar active regions is extended with angular sizes of a few arc minutes, brightness temperatures on the order of coronal electron temperatures, and no detectable circular polarization[80]. These characteristics are most easily explained in terms of the optically thick bremsstrahlung of thermal electrons in "coronal" condensations.

The recent development of space instruments which detect solar X-ray and ultraviolet emission has led to a renewed interest in the coronal atmosphere above solar active regions. Satellite X-ray observations have, for example, led to the detection of the arch-like "coronal condensations" which are now called "coronal loops". Moreover, the high spatial and spectral resolution of the X-ray instruments (i.e. those aboard Skylab and the S.M.M.) have revealed the richness and diversity of their structure[48]. The X-ray data indicate that the solar corona is mainly composed of

---

[76] Waldmeier, M. (1940), Variation der koronaform, Zs. f. Ap. 20:195-213.

[77] Lyot, B. (1944), Le filtre monochromatique polarisant et ses applications en physique solaire, Ann. d'Ap. 7:31-49.

[78] Van de Hulst, H.C. (1953), The chromosphere and the corona, The Sun, G.P. Kuiper, Ed., University of Chicago Press, Chicago, pp.203-321.

[79] Christiansen, W.N., Warburton, J.A. and Davies, R.D. (1957), The distribution of radio brightness over the solar disk at a wavelength of 20 centimeters, Austr. J. Phys. 10:491-514.

[80] Chiuderi-Drago, F., Felli, M. and Tofani, G. (1977), High resolution intensity and polarization structure of the sun at 21 cm, Astr. Ap. 61:79-91.

loop structures which outline the three-dimensional configuration of the coronal magnetic fields, and that the X-ray emission is due to hot, dense plasma which is confined by these fields. Furthermore, these quiescent loop structures appear relatively unchanged for time scales of hours, and only fluctuate over time scales of days. The slow evolution and long lifetime of the "coronal loops" detected at X-ray wavelengths makes them ideal candidates for aperture synthesis techniques at radio wavelengths. In fact, one would expect to detect them at 20 cm wavelength where the "coronal condensations" were observed more than two decades ago.

Unfortunately, high resolution observations of solar active regions at radio wavelengths have almost universally been carried out at 6 cm wavelength. Because the competing processes of gyroresonance emission and thermal bremsstrahlung come into play at this shorter wavelength, the 6 cm emission has been associated with a bewildering complexity of solar features including the legs of magnetic dipoles[6,38,39], sunspot umbrae[34], sunspot penumbrae[3,55], and magnetic neutral lines between sunspots[51]. Nevertheless, the 6 cm emission from one active region has been interpreted in terms of the optically thin bremsstrahlung of a hot, dense "coronal condensation" whose spatial configuration, emission measure, electron density and temperature are consistent with those inferred from X-ray observations of other active regions[2]. In addition, Velusamy and Kundu[74] and Kundu and Velusamy[75] have reported the detection of a looplike structure connecting two sunspots of opposite magnetic polarity at 6 cm wavelength. This discovery of the radio wavelength counterpart of a "coronal loop" was not entirely unambiguous, however, for the most intense emission was due to the gyroresonance emission of the sunspots and the polarity of the weaker bremsstrahlung did not change along the loop. This would be difficult to explain if a dipolar loop is involved. At any rate, the 6 cm loop emission can only be due to the optically thin bremsstrahlung of low lying loops, and the confusing effects of gyroresonant absorption can only be overcome by observing at 20 cm wavelength where the higher lying loops become optically thick to thermal bremsstrahlung and the gyroresonance emission is negligible.

Here, we report the first Very Large Array observations of looplike structures at 20 cm wavelength. In Section 2.5.2 we present the observations and show that the 20 cm loops extend across regions of opposite magnetic polarity in the underlying photosphere. In Section 2.5.3 we demonstrate that the 20 cm loops have physical parameters which are consistent with X-ray observations of "coronal loops". We then briefly discuss the significance of our observations for future studies of the structure of "coronal loops" and the triggering mechanisms of solar flares.

2.5.2 Observations of Coronal Loops at 20 Centimeters Wavelength

We have used the Very Large Array (V.L.A.) to observe the solar active region

AR 3159 on June 15 and 16, 1981. The position of AR 3159 on the solar surface was 26°S and 19°E at 14^h U.T. on June 15 and 26°S and 7°E at 14^h U.T. on June 16. The active region was observed at a wavelength, λ, of 20.75 cm (or 1446 MHz) with a bandwidth of 12.5 MHz for a four-hour period between 13^h30^m U.T. and 17^h30^m U.T. on each day. The individual antennae have a diameter of 25 m, providing a beamwidth of 29' at $\lambda = 20$ cm. A total of 26 antennae were used on all three arms of the array in the "B" configuration, with distances from the array center ranging from 0.15 to 6.39 km and minimum and maximum spacings between interferometer pairs of 0.34 and 11.1 km. The average correlated flux of 325 interferometer pairs was sampled every 10 s for both the left hand circularly polarized (LCP) signal, the right hand circularly polarized (RCP) signal, and the two crossed polarized signals. These data were then calibrated, edited and averaged to make synthesis maps of the total intensity, I = (LCP+RCP)/2 and Stokes parameter, V = (LCP-RCP)/2.

The data were calibrated by observing NRAO 150 for 5 min every 15 min, and by assuming that the flux density of this calibrator is 5.5 Jy at $\lambda = 20$ cm. The amplitude and phase of the correlated flux were calibrated according to the procedure described by Lang and Willson[38] together with a correction for the differences in the signal from high temperature noise sources detected in each polarization channel. The calibrated amplitude and phase for each polarization and every antenna pair were then taken to be the amplitude and phase of the source visibility function. The source intensity distribution was then obtained by Fourier transforming the calibrated data and using the CLEAN procedure on roughly 60,000 u-v components for each four-hour observation period. The synthesized beam has half power widths of 3.7" x 5.0" and is tilted at a position angle of -20°.

The synthesis maps of the total intensity I at $\lambda = 20$ cm are shown in Figure 19. The contours of the I maps mark levels of equal brightness temperature corresponding to 0.2, 0.4.....1.0 times the maximum brightness temperature of 2.1×10^6 K on June 15 (map A) and 4.1×10^6 K on June 16 (map B). On both days there was no detectable circular polarization ($V/I \lesssim 15\%$); suggesting that the emitting regions are optically thick to both the extraordinary and the ordinary modes of wave propagation. In this case the brightness temperatures are equal to the electron temperatures, T_e, which are typical of those found in the coronal loops observed at X-ray wavelengths ($T_e = 2$ to 4×10^6 K).

In Figure 19 we also show Meudon magnetograms of the longitudinal component of the photospheric magnetic field taken at 14^h02^m U.T. on June 15 (map C) and at 15^h 24^m U.T. on June 16 (map D). Here, the solid contours correspond to longitudinal magnetic field strengths of -200, -400, -600, -800, -1000, -1500 and -2000 gauss, while the dashed contours correspond to longitudinal magnetic field strengths of +100, +200, +400, +600, +800 and +1000 gauss. Notice that a dipolar feature,

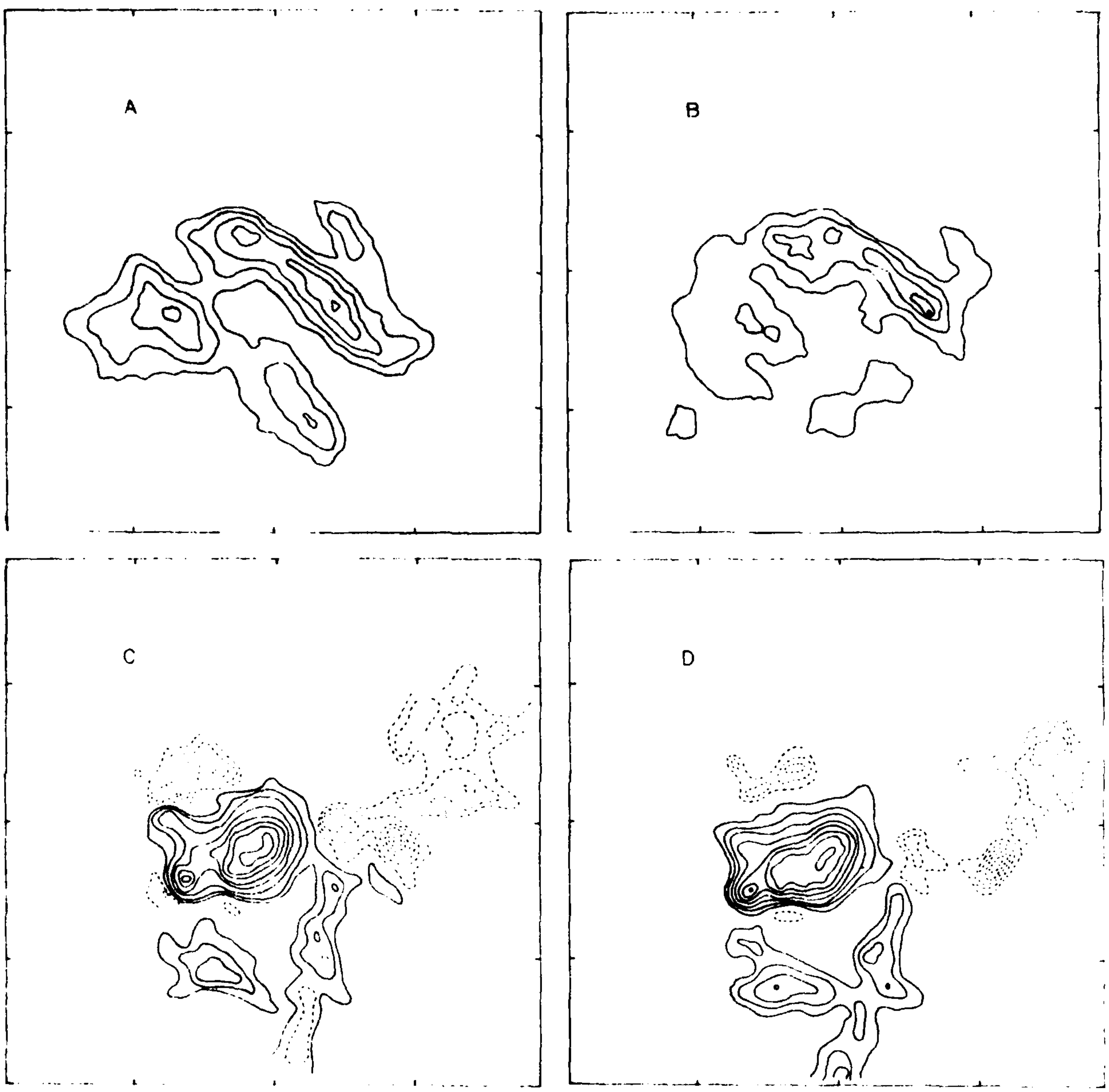

Figure 19. Very Large Array (V.L.A.) synthesis maps (A and B) of the total intensity I of the 20 cm radiation from active region AR 3159 are compared with Meudon magnetograms (C and D) of the longitudinal component of the photospheric magnetic field. All of the maps and magnetograms have identical fields of view and angular scales denoted by the 60" spacing between the fiducial marks on the axes. Looplike structures which join regions of opposite magnetic polarity have brightness temperatures of a few millions of degrees, and they appear to be the radio wavelength counterparts of the coronal loops detected at soft X-ray wavelengths.

whose feet are marked by field strengths as large as -2000 and +1000 gauss, dominates the region on each day. The looplike coronal structures observed at $\lambda = 20$ cm extend across these regions of opposite magnetic polarity, suggesting that they delineate the dipolar loops which join the two dominant sunspots while also connecting with other weaker magnetic features in the underlying photosphere.

The 20 cm loops are almost certainly the radio wavelength counterparts of the ubiquitous "coronal loops" detected at soft X-ray wavelengths. The absence of detectable circular polarization suggests that the 20 cm loops are optically thick, and that the brightness temperatures are equal to the electron temperatures of the hot, dense plasma trapped within the loop. In fact, the field of view of the individual V.L.A. antennae at 20 cm wavelength covers the entire Sun. We therefore examined our data for 20 cm coronal loops associated with other active regions. We found a total of 15 coronal loops associated with 3 active regions on 5 days. The 20 cm coronal loops are therefore truly ubiquitous features of the solar atmosphere (see Figure 20 for another example). The maximum electron temperatures, T_e(max), are characteristic of those found in the X-ray coronal loops with $T_e(\max) = 2$ to 4×10^6 K. The total extents of the 20 cm loops range between 4×10^9 cm and 4×10^{10} cm (where 1" = 725 km on the solar surface), and these are also comparable to the X-ray coronal loops which have semilengths L of 10^9 cm to 10^{10} cm (L is half the total extent of the loop as measured along the magnetic field).

2.5.3 Interpretation of the Observations as the Radio Wavelength Counterpart of the X-ray Coronal Loops

We have discovered looplike coronal structures at 20 cm wavelength which join regions of opposite magnetic polarity. The 20 cm loops are almost certainly the radio wavelength counterparts of the ubiquitous "coronal loops" detected at soft X-ray wavelengths. The absence of detectable circular polarization suggests that the 20 cm loops are optically thick, and that the brightness temperatures are equal to the electron temperatures of the hot, dense plasma trapped within the loop. The maximum electron temperatures, T_e(max), are then characteristic of those found in the X-ray coronal loops with $T_e(\max) = 2$ to 4×10^6 K. The total extents of the 20 cm loops range between 4×10^9 cm and 4×10^{10} cm (where 1" = 725 km on the solar surface), and these are also comparable to the X-ray "coronal loops" which have semilengths L of 10^9 cm to 10^{10} cm (L is half the total extent of the loop as measured along the magnetic field). Furthermore, under the assumption that the 20 cm loops are in hydrostatic equilibrium, we can use the scaling relationship of Rosner, Tucker and Vaiana[73]

$$T_e(\max) = 1.4 \times 10^3 \, (pL)^{1/3} \tag{21}$$

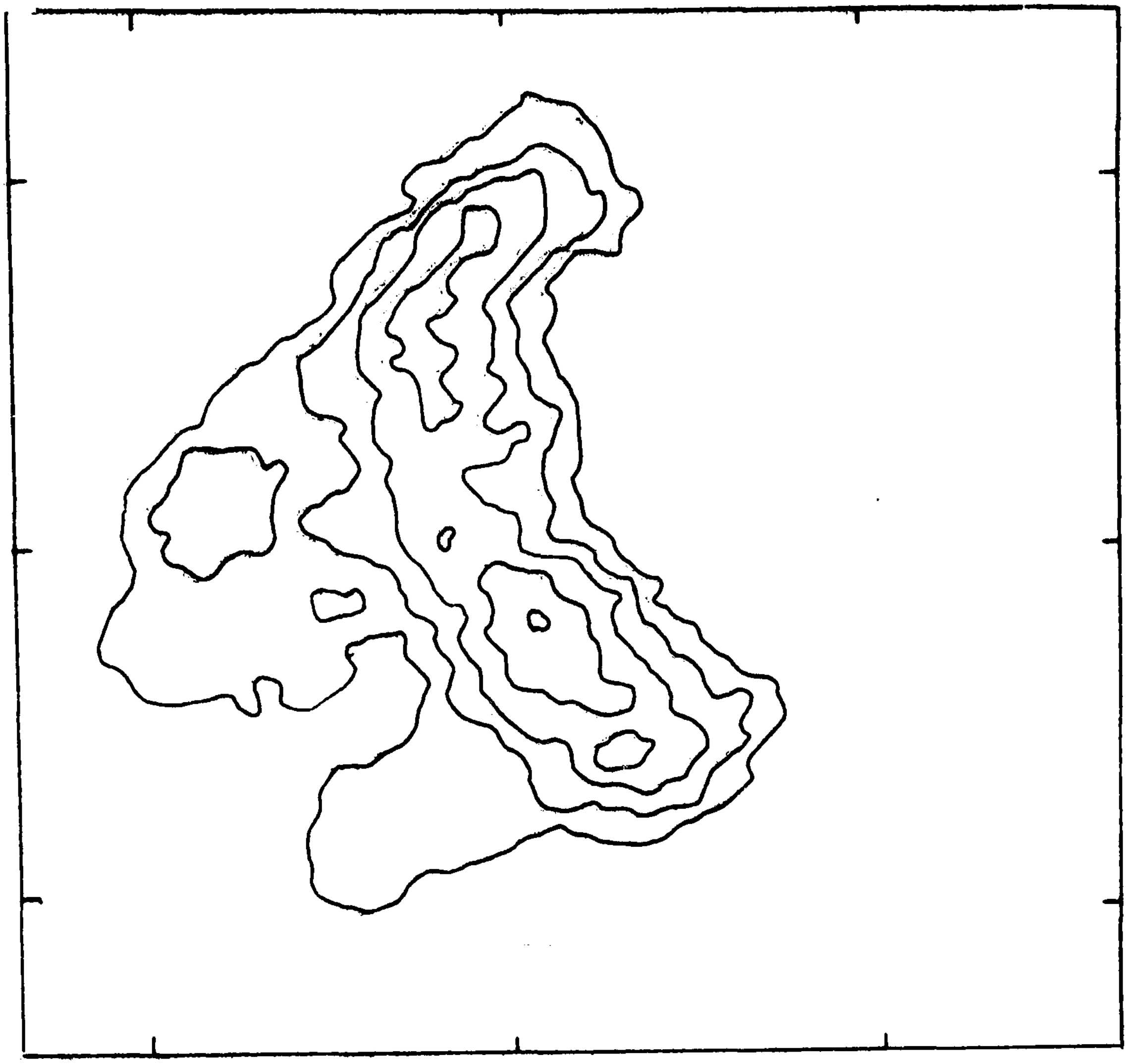

Figure 20. The 20 cm coronal loop associated with the active region AR 3159 on June 13, 1981. The active region was located about 20° across the solar surface from the east limb, and the 20 cm loop is therefore seen projected eastward (to the left). Here the contours mark levels of equal brightness temperature corresponding to 0.2, 0.4, ...1.0 times the maximum brightness temperature of $T_B \sim 2 \times 10^6$ K.

to obtain the loop pressure p. Choosing $T_e(\mathrm{max}) = 3 \times 10^6$ K and $L = 5 \times 10^9$ cm, we obtain a pressure of $p = 1.96$ dyn cm^{-2}, which is again characteristic of the X-ray coronal loops. We can also check the consistency of our argument that the 20 cm loops are the optically thick bremsstrahlung of thermal electrons by determining the electron density $N_e = p/(2kT_e) = 2.5 \times 10^9$ cm^{-3}, where Boltzmann's constant $k = 1.38 \times 10^{-16}$ erg °K^{-1}. This value of electron density can be used together with an average electron temperature of $T_e \sim 10^6$ K to obtain the optical depth, τ_B, of thermal bremsstrahlung from Eq. (1) which indicates that $\tau_B = 2.5$. Our assumptions are therefore satisfied for the brightness temperature $T_B = [1 - \exp(-\tau_B)]T_e = 0.92\ T_e$. Finally, we also notice that when the geometry of a hydrostatic loop is considered, the only physical solutions are those for which the temperature maximum occurs at the central apex or top of the loop[73]. Interestingly enough, the brightness temperatures of the 20 cm loops do have their maximum values near the central portions of the loops.

In summary then, Very Large Array observations of solar active regions at 20 cm wavelength have led to the detection of looplike coronal structures which have physical parameters that are identical to those of the coronal loops detected at X-ray wavelengths. Despite the considerable theoretical effort which has been devoted to an understanding of the X-ray loops[73,81,82,83,84], comparisons of model predictions with X-ray data have generally been limited to consistency checks with overall loop parameters. The possibility of detailed comparisons with model predictions has now been opened up with the discovery that V.L.A. synthesis maps at 20 cm wavelength can specify the temperature and density structure of coronal loops with second of arc accuracy. Furthermore, the evolution of coronal loops can be investigated by taking V.L.A. synthesis maps at intervals of one hour or less. This may lead to the detection of temperature enhancements which are expected during pre-flare activity[85]. This discovery may also lead to the future investigation of the thermal cyclotron lines in the solar corona which have been predicted by Zheleznyakov and Zlotnik[86,87,88].

---

[81] Craig, I.J.D., McClymont, A.N. and Underwood, J.H. (1978), The temperature and density structure of active region coronal loops, Astr. Ap. 70:1-11.

[82] Vesecky, J.F., Antiochos, S.K. and Underwood, J.H. (1979), Numerical modeling of quasi-static coronal loops, Ap. J. 233:987-997.

[83] Serio, S., Peres, G., Vaiana, G.S., Golub, L. and Rosner, R. (1981), Closed coronal structures II. Generalized hydrostatic model, Ap. J. 243:288-300.

[84] Pallavicini, R., Peres, G., Serio, S., Vaiana, G.S., Golub, L. and Rosner, R. (1981), Closed coronal structures III. Comparison of static models with X-ray, e.u.v. and radio observations, Ap. J. 247:692-706.

[85] Syrovatskii, S.I. and Kuznetsov, V.D. (1980), On the possibility of radio observations of current sheets on the Sun, I.A.U. Symposium No. 86: Radio Physics of the Sun, M.R. Kundu and T.E. Gergely, Eds., Reidel, Dordrecht.

[86] Zheleznyakov, V.V. and Zlotnik, E. Ya. (1980a), Thermal cyclotron radio emission of neutral current sheets in the solar corona, Solar Phys. 68: 317-326.

[87] Zheleznyakov, V.V. and Zlotnik, E. Ya. (1980b), Fine structure of microwave solar radio emission from solar activity centers, Sov. Astr. AJ 24:448-454.

[88] Zheleznyakov, V.V. and Zlotnik, E. Ya. (1980c), Thermal cyclotron radiation from solar active regions, I.A.U. Symposium No. 86: Radio Physics of the Sun, M.R. Kundu and T. Gergely, Eds., Reidel, Dordrecht.

3. TIME DEVELOPMENT OF RADIO EMISSION FROM SOLAR ACTIVE REGIONS

3.1 VERY LARGE ARRAY OBSERVATIONS OF MULTIPLE COMPONENT BURSTS

3.1.1 Introduction

High resolution observations of solar flares at soft X-ray and ultraviolet wavelengths have led to the conclusion that the flare energy at these wavelengths is *emitted from small, hot and dense* kernels with electron temperatures of $T_e \sim 2 \times 10^7$ K[89,90,91], electron densities of $N_e \sim 10^{10}$ cm^{-3},[92] and angular sizes of $\phi \sim 2''$-$10''$ [93,91]. It is now possible to use synthesis arrays to resolve second-of-arc angular structure at radio wavelengths, and in this section we report observations with the Very Large Array (V.L.A.) of radio wavelength bursts with brightness temperatures of $T_B \sim 1$-2×10^7 K and angular sizes of $\phi \sim 6''$-$12''$. We therefore seem to have detected the radio wavelength counterpart of the soft X-ray kernels. In addition to providing new information on the angular sizes and brightness temperatures of the radio emitting bursts, the V.L.A. observations also provide circular polarization information

---

89. Cheng, C.C. and Widing, K.G. (1975), Spatial distribution of XUV emission in solar flares, Ap. J. 201: 735-739.

90. Widing, K.G. (1975), Fe XXIII 263 Å and Fe XXIV emission in solar flares, Ap Lett. 197: L33-L35.

91. Brueckner, G.E. (1976), ATM observations on the XUV emission from solar flares, Phil. Trans. Roy. Soc. London, A281: 443-459.

92. Moore, R.L. et al. (1978), The thermal X-ray plasma. Big Bear Solar Obs. Rpt. 0180.

93. Kahler, S.W., Krieger, A.S. and Vaiana, G.S. (1975). Morphological evolution of X-ray flare structures from the rise through the decay phase, Ap. J. Lett. 199: L57-L61.

which, given plausible assumptions about the electron density, can provide information about the magnetic field strength in the emitting region.

It is also of interest to specify the location of the burst emitting regions. Observations at Hα wavelengths indicate, for example, that this flare emission occurs near magnetic neutral lines away from sunspots[94], but the chromospheric flares seen at Hα wavelengths could be secondary effects of energy release in the solar corona. Soft X-ray data indicate that flare energy is actually released in magnetic loops which are not necessarily connected to sunspots[91], and that soft X-ray flares tend to occur near small, bright "suprathermal plasma nodules"[95]. The angular sizes of the nodules are comparable to those of the regions of enhanced radio emission which overlie chromospheric plage in "coronal condensations"[2], and the V.L.A. observations given in 3.1.2 indicate that two 6 cm bursts occurred within a plage-associated "coronal condensation" in regions away from sunspots and near magnetic neutral lines. Our observations are therefore consistent with those of Alissandrakis and Kundu[96] and Marsh, Zirin and Hurford[97] which indicate that small radio wavelength burst sources lie near magnetic neutral lines rather than sunspots.

The temporal evolution of the solar flares observed at hard X-ray wavelengths is of special interest for they appear to be composed of a train of about a dozen "elementary flare bursts" which have individual lifetimes of ~ 10 s to 30s[98,99,100,101,102,103]. Small Hα kernels with angular sizes of $\phi \sim 4''-9''$ have also been

---

94. Svestka, Z. (1976), *Solar flares* Dordrecht, Reidel .

95. de Feiter, L.D. and de Jager, C. (1973), Superthermal plasma nodules and their relation to solar flares, *Solar Phys.* *28*: 183-186.

96. Alissandrakis, C.E. and Kundu, M.R. (1978) 6 centimeter observations of solar bursts with 6" resolution, *Ap. J.* *222*: 342-356.

97. Marsh, K.A., Zirin, H. and Hurford, G.J. (1979), VLA observations of solar flares, interpreted with optical, X-ray and other microwave data, *Ap. J.* *228*: 610-615.

98. Frost, K.J. (1969), Rapid fine structure in a burst of hard solar X-rays observed by OSO-5, *Ap. J. Lett.* *158*: L159-L163.

99. Parks, G.K. and Winckler, J.R. (1969) Sixteen-second periodic pulsations observed in the correlated microwave and energetic X-ray emissions from a solar flare, *Ap. J. Lett.* *155*: L117-L120.

100. Janssens, T.J. and White, K.P. (1970), Description of mass motions and brightenings in a class 2b flare, August 8, 1968, *Solar Phys.* *11*: 299-309.

101. van Beek, H.F., deFeiter, L.D. and deJager, C. (1974), *Space Research XIV*, M.J. Rycroft and R.D. Reasenberg (Eds.) Akademie Verlag , Berlin, p.447.

102. van Beek, H.F., deFeiter, L.D. and deJager, C. (1976), *Space Research XVI*, M.J. Rycroft (Ed.), Akademie Verlag, Berlin, p. 819.

103. deJager, C. and deJonge, G. (1978), Properties of elementary flare bursts, *Solar Phys.* *58*: 127-137.

Both the V.L.A. and the W.S.R.T. synthesis maps refer to an observing interval of about eleven hours, and for four of these hours (13^h30^m U.T. to 17^h30^m U.T.) the active region was being simultaneously observed by both synthesis telescopes.

The radio wavelength synthesis maps of the total intensity, I, of AR 2490 on June 10 are given in Figure 8 where they are compared with a soft X-ray map taken at the Ne IX line in a 20 min interval centered at 13^h 54^m U.T. Two main components are shown on the 6 cm and 20 cm maps, which we designate as component A (to the east) and component B (to the west). Component A is the most intense source at 6 cm wavelength on June 10, and it is associated with a group of sunspots (cf. Figure 12); while component B is the most intense component at 20 cm wavelength on June 10, and it is associated with bright plage seen at Hα wavelengths (cf. Figure 10). Component B is also detected at both 2 cm and X-ray wavelengths on June 10, while component A was undetected at these wavelengths on June 10. The radio maps have contours of equal brightness temperature corresponding to 0.2, 0.4, 0.6 and 0.8 times the maximum brightness temperature, T_B(max), given in Table 2. This maximum brightness temperature was derived using the Rayleigh-Jeans law together with the assumption that there is a constant brightness temperature over the synthesized beam area at the point of maximum brightness. For a maximum flux density, S(max), per unit beam area and major and minor synthesized beam half power widths θ_1 and θ_2, we have $T_B(\mathrm{max}) = 1.36 \times 10^3 \lambda^2 S(\mathrm{max})/(\theta_1\theta_2)$ where the wavelength λ is in cm, the flux density is in Jy where 1 Jy = 10^{-23} erg s^{-1} cm^{-2} Hz^{-1} and θ_1 and θ_2 are in seconds of arc. The X-ray contours are at levels of 50, 60, 70 and 80 counts per second above a background level of 13.2 counts per second with a maximum signal of 101.1 counts per second and an instrumental sensitivity of 6.3 counts per photon cm^{-2} s^{-1} arc sec^{-2} for a uniform extended source at the Ne IX line. The position of the X-ray source was determined relative to nearby sunspots and located in Figure 8 with a positional accuracy of about 5" by determining the positions of the sunspots relative to the phase center of the radio synthesis maps. The cross mark shown in Figures 8 and 9 corresponds to the same position on the solar surface at all wavelengths and for both days.

The radio wavelength synthesis maps of the total intensity, I, of AR 2490 on June 11 are given in Figure 9 where they are compared with a soft X-ray map taken at the Ne IX line in a 20 min interval centered at 20^h12^m U.T. The radio maps have contours of equal brightness temperature corresponding to 0.2, 0.4, 0.6 and 0.8 times the maximum brightness temperature, T_B(max), given in Table 2, while the X-ray contours are at 20, 30 and 40 counts per second above a background level of 13.2 counts per second with a maximum of 85.9 counts per second. A comparison of Figures 8 and 9 indicates dramatic changes in source structure on an interval of one day which are correlated with similar changes in the chromospheric plage seen at Hα wavelengths. A correlation between changes in the detailed morphological features of 6 cm emission detected during the emission of hard X-ray flares[104,105,106], but the available instrumentation has not allowed the resolution of hard X-ray sources with second-of-arc angular sizes. Nevertheless, deJager[107] has suggested that the elementary flare bursts detected at hard X-ray wavelengths are excited by small kernels similar to those detected at soft X-ray wavelengths. In Section 3.1.2 we report related radio wavelength observations of bursts that are composed of elementary events whose temporal evolution is very similar to that detected at hard X-ray wavelengths, but whose angular sizes and brightness temperatures are similar to the sizes and temperatures of the soft X-ray kernels.

In Section 3.1.2 we present our basic observational data while also discussing the limitations of using the V.L.A. to extract information about small, weak bursts. Here, we present angular sizes, brightness temperatures, circular polarization structures, and time profiles for a total of seven bursts observed at 6 cm and 20 cm wavelength. The limiting time resolution of the observed profiles is 10 s, and it therefore precludes the detection of burst components with shorter duration. In Section 3.1.2 we also provide the location of two 6 cm bursts on 6 cm synthesis maps of the active region. In Section 3.1.3 we interpret our observations in terms of thermal gyroresonance absorption in a hot ($\sim$ 2 x 10^7 K), dense ($\sim 10^{10}$ to 10^{11} electrons cm^{-3}) plasma, and also provide an estimate of the magnetic field strength in the emitting region ($H \sim 90$ gauss). Here we also discuss the constraints which V.L.A. observations provide on the physical nature of the burst emitting sources.

3.1.2 Observations of the Bursts and Location of the Energy Release

Seven weak radio bursts have been detected while using the V.L.A. to track active region AR 2032 from sunrise to sunset on October 5 and 6, 1979. Region AR 2032 had a position on the Sun's surface of 17°N and 61°E at 13^h U.T. on October 5, and 16°N and 45°E at 13^h U.T. on October 6. Although this region was at all times in the center of our beam, the field of view of the individual antennae also included AR 2030 which was 3'N and 2'W of AR 2032. Observations were made simultaneously at 6 cm and 20 cm by splitting the V.L.A. antennae into two subarrays of nearly identical u-v coverage[2]. While the periods of the bursts were time edited from all of the observed fringe visibilities before making the maps of the active

---

104. deJager, C. (1967), The hard solar X-ray burst of 18 September 1963, Solar Phys. 2: 327-346.

105. Vorpahl, J. and Zirin, H. (1970), Identification of the hard X-ray pulse in the flare of September 11-12, 1978, Solar Phys. 11: 285-290.

106. Vorpahl, J. (1972), X-radiation (E > 10 KeV), Hα and microwave emission during the impulsive phase of solar flares, Solar Phys. 26: 397-413.

107. deJager, C. (1979), On the seats of elementary flare bursts, Solar Phys. 64: 135-141.

regions, as detailed elsewhere[2], the burst data are here used separately to derive useful information about the size, brightness temperature, polarization, positions and temporal evolution of the bursting emission.

The methods of amplitude and phase calibration which were applied to the steady radio emission of the active region[2] were also applied to the solar radio bursts. Although in principle the best way to study the evolution of a radio burst would be to make "snapshot" maps for each 10 s integration, for several reasons these nearly instantaneous maps could not be made from our data. One reason was the increase in the residual phase calibration error with increasing projected baseline. While these errors are of minor importance when mapping extended structures in which most of the flux density is detected at the shorter baselines, they become intolerable in the case of the smaller bursts, in which most of the flux is detected at the longer baselines. Moreover, the intrinsic shape of the beam for a snapshot map is much more complex than that of a full synthesis map, for it is dominated by strong grating responses. In the presence of phase errors the intensity peaks in the snapshot maps therefore tend to have even closer values, and this makes the cleaning process very inefficient, if not impossible. There is also the additional problem of isolating the fringe visibilities of the weak radio bursts from those of the steady emission of the active region. The background emission of the active region dominates the signal on the shorter baselines, and particularly at 20 cm wavelength the separation of the amplitudes and phases of the weak bursts at the shorter baselines is very uncertain.

In view of these difficulties in handling the fringe visibilities of weak radio bursts, we only used amplitude and phase information to obtain approximate positions of the 6 cm bursts, while generally limiting our analysis to the relative fringe amplitudes detected at the time of peak flare intensity. By discarding all phase information as well as unreliable amplitudes, we lose the ability to make full use of the different points in the two-dimensional u-v plane, but we gain much more reliable information on the size, brightness temperature, and polarization of the flare emitting sources. The angular sizes of these sources were, for example, determined by plotting the fringe amplitudes at the time of peak flare intensity as a function of $(u^2 + v^2)^{\frac{1}{2}}$, where u and v are the coordinates of the visibility function in the u-v plane. These amplitude data were then fitted by the method of least squares to obtain the intensity and angular size (full width to half power, ϕ) of that spherical Gaussian source whose fringe visibility amplitudes give the best fit to the data. By doing this, one discards information about the two-dimensional structure of the source, and only an equivalent spherical diameter is obtained. Moreover, because the detected flares were usually weak and small in angular size, our analysis was generally limited to the amplitude information obtained on roughly two-thirds of the available baselines. Nevertheless, this procedure enabled us to make reliable estimates of the angular sizes, ϕ, at the time of peak flare intensity with an uncertainty of only ±0.6". As illustrated in Table 5, the bursting source was in every case resolved with angular sizes, ϕ , between 6" and 12", peak flux densities of between 0.1 and 6.0 sfu (where 1 sfu = 10^4 Jy = 10^{-19} ergs s^{-1} cm^{-2} Hz^{-1}), and peak brightness temperatures, T_B, in the range between 1 and 2 x 10^7 K.

In order to study the degree of circular polarization ρ_c = V/I, we have computed the ratio of the V visibility amplitude to that of the I visibility amplitude for those baselines with fringe frequencies close to the size of the bursting source for which the ratio of the flux of the burst to that of the active region is a maximum. Because the background emission of the active region at 6 cm was circularly polarized with ρ_c = 30±10%, we could not reliably measure the weak circular polarization of the two 6 cm flares, but the circular polarization of the background emission at 20 cm was small, and at peak intensity all five bursts detected at this wavelength had ρ_c = 80-100% with an uncertainty of ±15% due to spurious instrumental polarization[2].

The positions of the two 6 cm bursts, whose time profiles were of the impulsive-gradual decay type, were determined by making a snapshot map at the time of peak burst intensity. As illustrated in Figure 21 we were able to use these crude, uncleaned maps to locate the position of the peak emission with respect to the full 6 cm synthesis map of the active region. Although the nominal positional accuracy of the uncleaned snapshot maps is better than 3", additional uncertainty arises from nearby grating responses of similar intensity. The error box of ∿ 10" in width takes this into account, and as illustrated in Figure 21 we are able to conclude that the two solar bursts observed at 6 cm wavelength occurred within the plage-associated "coronal condensation" shown on the synthesis maps. Moreover, for one of the bursts an Hα photograph could be used to compare the positions of the Hα and 6 cm emission. After correcting for the displacement of ∿ 20" caused by the higher radio emission located ∿ 2 x 10^9 cm above the Hα emission, the Hα flare and 6 cm burst were found to be spatially coincident within the uncertainty of ±5%.

Of special interest is the temporal evolution of the several bursts detected at 20 cm wavelength. As illustrated in Figures 22 and 23, the bursts are composed of trains of events which have individual lifetimes of between 20 s and 30 s. The rapid rise and decay times and the durations of the individual events, as well as the number of events per burst, are very similar to the "elementary flare bursts" observed at hard X-ray wavelengths. Nevertheless, the limiting time resolution of our data is 10 s, while the hard X-ray instrumentation has usually been limited to ∿ 1 s time resolution, and for this reason we cannot preclude the existence of more rapid structure in both the 20 cm bursts and the hard X-ray flares. In fact, the

TABLE 5. Start and stop times, peak flux density, S, angular size, ϕ, and peak brightness temperature. T_B, of solar bursts detected at wavelengths λ = 6 cm or 20 cm[a].

Start (UT)	Stop (UT)	Date	Active Region	λ (cm)	S sfu)	ϕ (")	T_B (K)
16^h10^m............	17^h00^m	1979 Oct. 5	AR 2030	20	0.25	9.9	1.4×10^7
20 07.............	20 20	1979 Oct. 5	AR 2032	20	0.10	7.7	0.9×10^7
20 21.............	20 23	1979 Oct. 5	AR 2032	6	6.00	14.1	1.5×10^7
20 35.............	20 38	1979 Oct. 5	AR 2032	20	0.10	7.3	1.0×10^7
22 47.............	23 02	1979 Oct. 5	AR 2030	20	0.50	14.1	1.4×10^7
17 23.............	17 25	1979 Oct. 6	AR 2032	6	1.00	9.4	0.5×10^7
19 57.............	20 23	1979 Oct. 6	AR 2030	20	0.12	9.4	0.7×10^7

[a] The peak brightness temperature T_B was derived using the relation $T_B = (S\,\lambda^2)/(2.266\,k\,\phi^2)$.

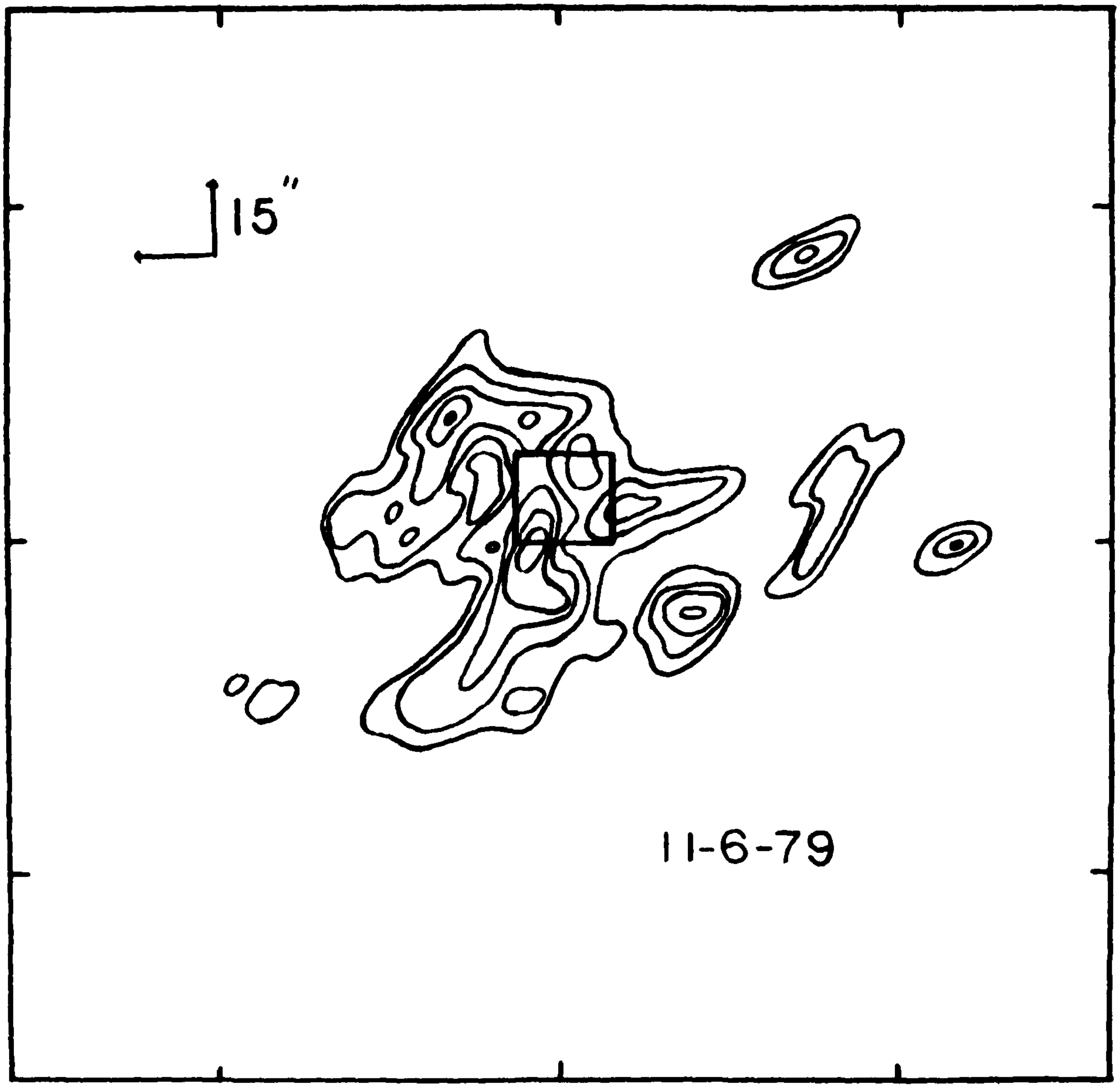

Figure 21. The location of a 6 cm burst (square) on a 6 cm synthesis map of the total intensity of the active region. The radio burst occurs within a hot, 10^6 K plasma located between two sunspots in a region of one magnetic polarity.

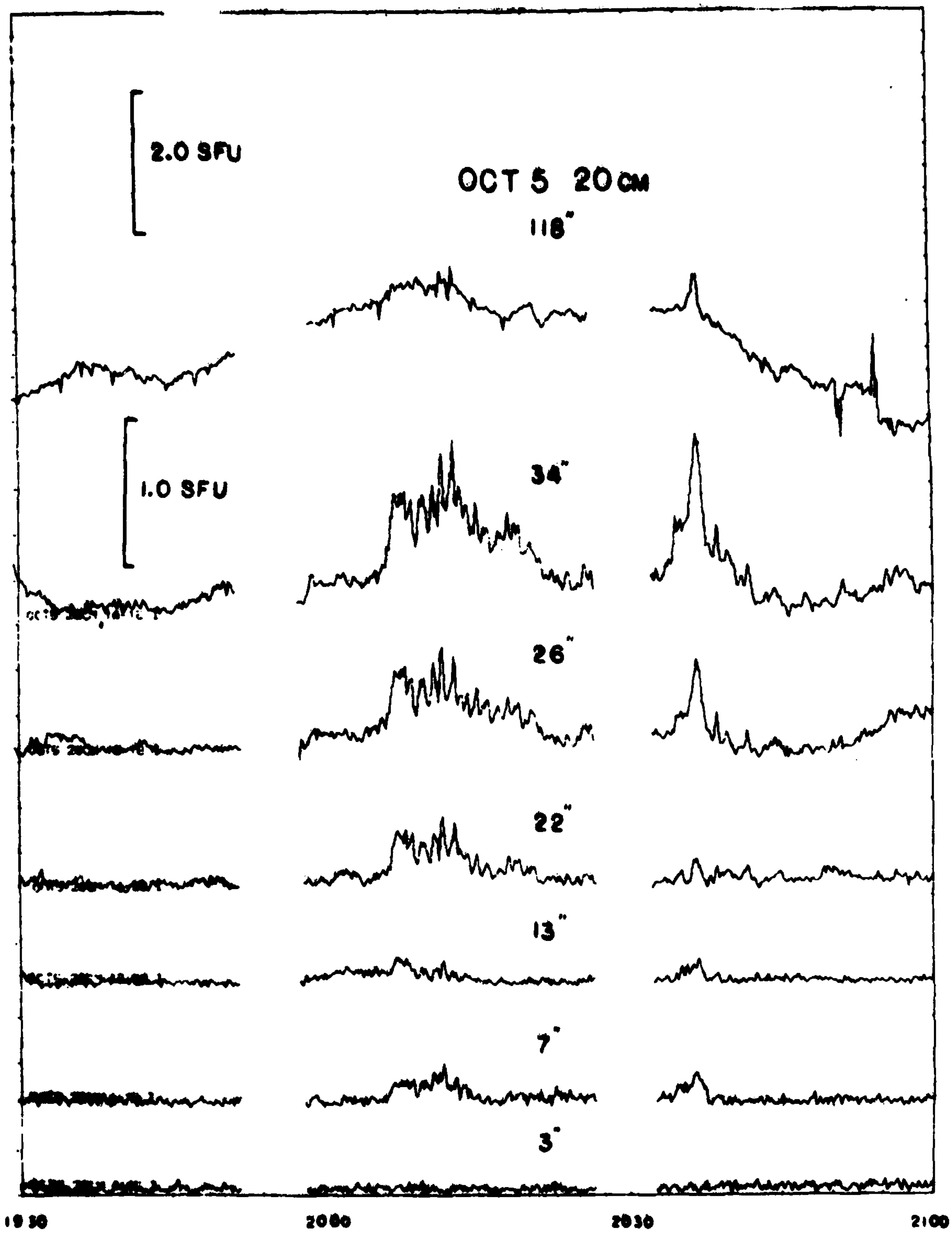

Figure 22. The time profiles of several spikelike events making up a burst at 20 cm wavelength. Each profile was detected with one interferometer pair whose angular resolution is given above the profile. The combined amplitudes of 28 pairs gave the visibility function of an 8" source at 20^h13^m U.T. and 20^h36^m U.T., suggesting that all of the spiked emission comes from a source of this size. Each spike has a duration between 10 s and 60 s, a circular polarization of $\rho_c \sim 100\%$, and a brightness temperature of $T_B \sim 1 \times 10^7$ K.

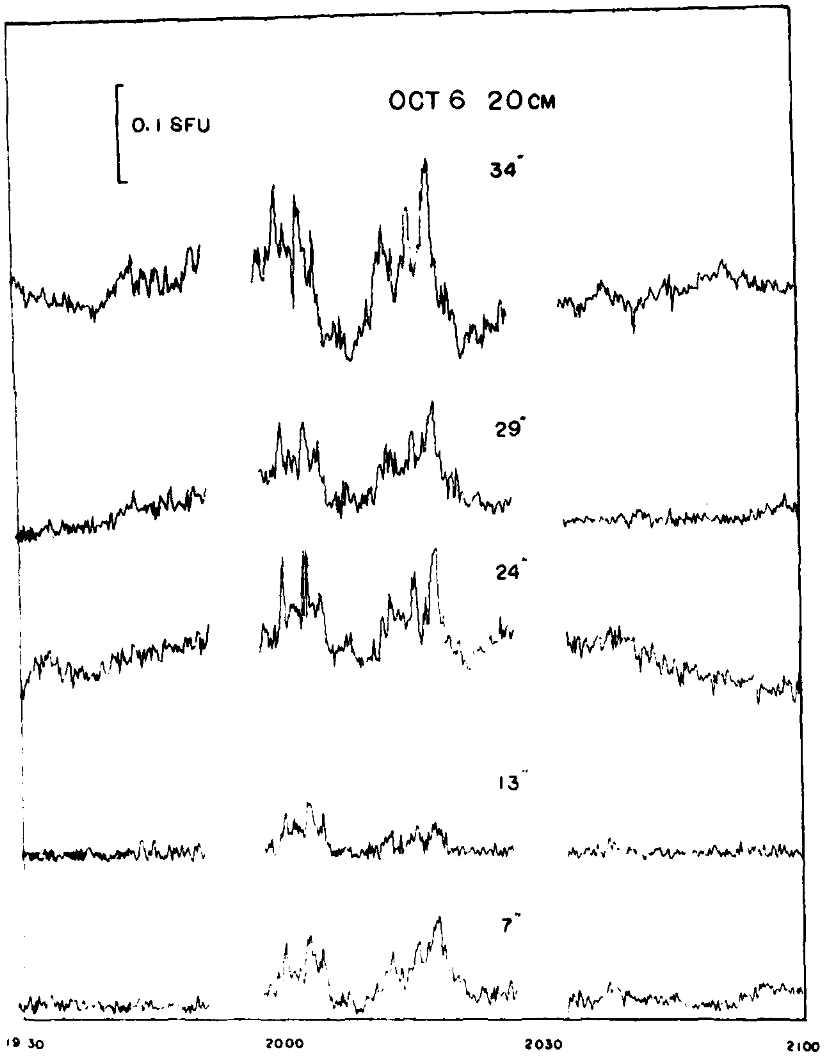

Figure 23. The time profiles of several spikelike events making up two bursts at 20 cm wavelength. Each profile was detected with one interferometer pair whose angular resolution is given above the profile. The combined amplitudes of 28 interferometer pairs gave the visibility function of a 9" source at 20^h18^m U.T.. This source had a peak brightness temperature of $T_B \sim 1 \times 10^7$ K and a circular polarization of $\rho_c \sim 100\%$.

Solar Maximum Mission satellite is apparently now recording hard X-ray spikes with scales of about 0.1 s, and rapid spikelike structures with durations or periodicities of about 0.1 s are known to be superposed upon the longer components of solar bursts seen at both decimeter and centimeter wavelegnths[108,109.110,111,112]. Moreover, quasi-periodic intensity fluctuations with time scales between 10 s and 100 s are known to be associated with the microwave emission of type IV bursts[113,114,115]. Thus, detection of intensity fluctuations during solar bursts at radio wavelengths with time scales $\sim$ 20 s is certainly not unique, but we have for the first time been able to measure the angular sizes, brightness temperatures, and circular polarizations of the sources which are giving rise to the individual bursts. As illustrated in Table 5, angular sizes of $\phi \sim 8''$ and brightness temperatures of $T_B \sim 2 \times 10^7$ K are found at the times of peak flare intensity at 20 cm wavelength. Moreover, because the relative amplitudes at different baselines remain constant from event to event (cf. Figure 22), there is some evidence that the angular size of the emitting source does not change during the emission of a train of events which make up a burst. As already mentioned, the angular sizes and temperatures of the 20 cm bursts are comparable to those of the kernels detected at soft X-ray wavelengths, suggesting that the observed bursts are coming from the radio wavelength counterpart of the soft X-ray kernels.

---

108. Young, C.W., Spencer, C.L., Moreton, G.E. and Roberts, J.A. (1961), A preliminary study of the dynamic spectra of solar radio bursts in the frequency range 500-950 Mc/s, *Ap. J. 133*: 243-257.

109. deGroot, T. (1970) Solar radio spectra between 160 and 320 MHz, *Solar Phys. 14*: 176-189.

110. Gotwols, B.L. (1972), Quasi-periodic solar radio pulsations at decimetric wavelengths, *Solar Phys. 25*: 232-236.

111. Kaufman, P. (1976), Fast time structures superimposed to impulsive solar microwave bursts with slowly varying or stationary polarization degree, *Solar Phys. 60*: 367-381.

112. Elgaroy, O. and Sveen, O.P. (1979),Drifting spikes - a new species of solar radio bursts, *Nature 278*: 626-627.

113. Cribbens, W., and Matthews, P.A. (1969), Periodic structure in solar radio bursts and its relation to burst energy, *Nature 222*: 158-159.

114. Maxwell, A. and Fitzwilliam, J. (1973), Microwave pulsations from solar flares, *Ap. Letters. 13*: 237-242.

115. Cliver, E.W., Hurst, M.D., Wefer, F.L. and Bleiweiss, M.P. (1976), Quasi-periodic burst structure at 28 GHz and its relationship to burst morphological parameters, *Solar Phys. 48*: 307-320.

3.1.3 Multiple Component Bursts from a Single Small Emitter

We have used the V.L.A. to resolve the regions of burst energy release at 6 cm and 20 cm wavelength, showing that they have angular sizes of $\phi \sim 8''$ and brightness temperatures $T_B \sim 2 \times 10^7$ K which are similar to the sizes and temperatures of the soft X-ray kernels. This leads us to suppose that we are detecting the radio emission of the thermal plasma which gives rise to the soft X-ray flares. As was the case for the steady radio emission of the active regions[2], the burst emission might be explained by either the bremsstrahlung or the gyroresonance radiation of this hot, dense plasma. To compare the two radiation mechanisms we choose an electron temperature $T_e = 2 \times 10^7$ K, which is near the observed brightness temperatures, and an electron density of $N_e = 10^{10}$ cm^{-3}. For $N_e > 3 \times 10^{10}$ cm^{-3}, the plasma frequency would exceed 1.495×10^9 Hz and the 20 cm radiation would not then propagate through the emitting plasma, and the optical depth would become infinite. In this case, $T_B = T_e$, but the radiation is unpolarized, contradicting the observations and therefore setting an upper limit to N_e. An $N_e = 10^{10}$ cm^{-3} is characteristic of the plage-associated coronal condensation from which the radio bursts are likely to arise. The relevant formulae for the optical depth[2,29,40,41] then give $\tau_B \sim 0.003$ for the 20 cm bremsstrahlung of a source with angular size $\phi = 8''$, and $\tau_{GR} \sim 0.1$ for the 20 cm gyroresonance absorption at the sixth harmonic ($H_\ell = 90$ gauss). The high degree of circular polarization of the 20 cm bursts as well as the observed T_B are most easily explained by the gyroresonant process. This is because the gyroradiation is itself circularly polarized with the relatively low magnetic field strengths of $H_\ell = 90$ G and sufficiently high optical depths can be achieved. Bremsstrahlung would require propagation effects in much stronger magnetic fields of $H_\ell \sim 500$ gauss to produce the necessary increase in optical depth of the extraordinary wave and the observed degree of circular polarization.

Our V.L.A. observations also provide some evidence about the physical nature of the sources which emit the sequence of radio events which make up the bursts observed at 20 cm. An examination of the fringe amplitudes of the individual events which make up the flare shown in Figure 22, for example, indicates that the relative amplitudes remained the same for all interferometer pairs during the burst. This suggests that the angular size of the burst emitter did not change from event to event, or that if the size changed it was undetectable. Similarly, there was no detectable phase change of the correlated signal associated with the individual events of the burst for the fringe spacing which provided the most intense burst signal (see Figure 24). This suggests that only one source emits the train of events associated with the burst and that the individual events are not excited by different sources at different positions within the active region. Of additional interest is the fact

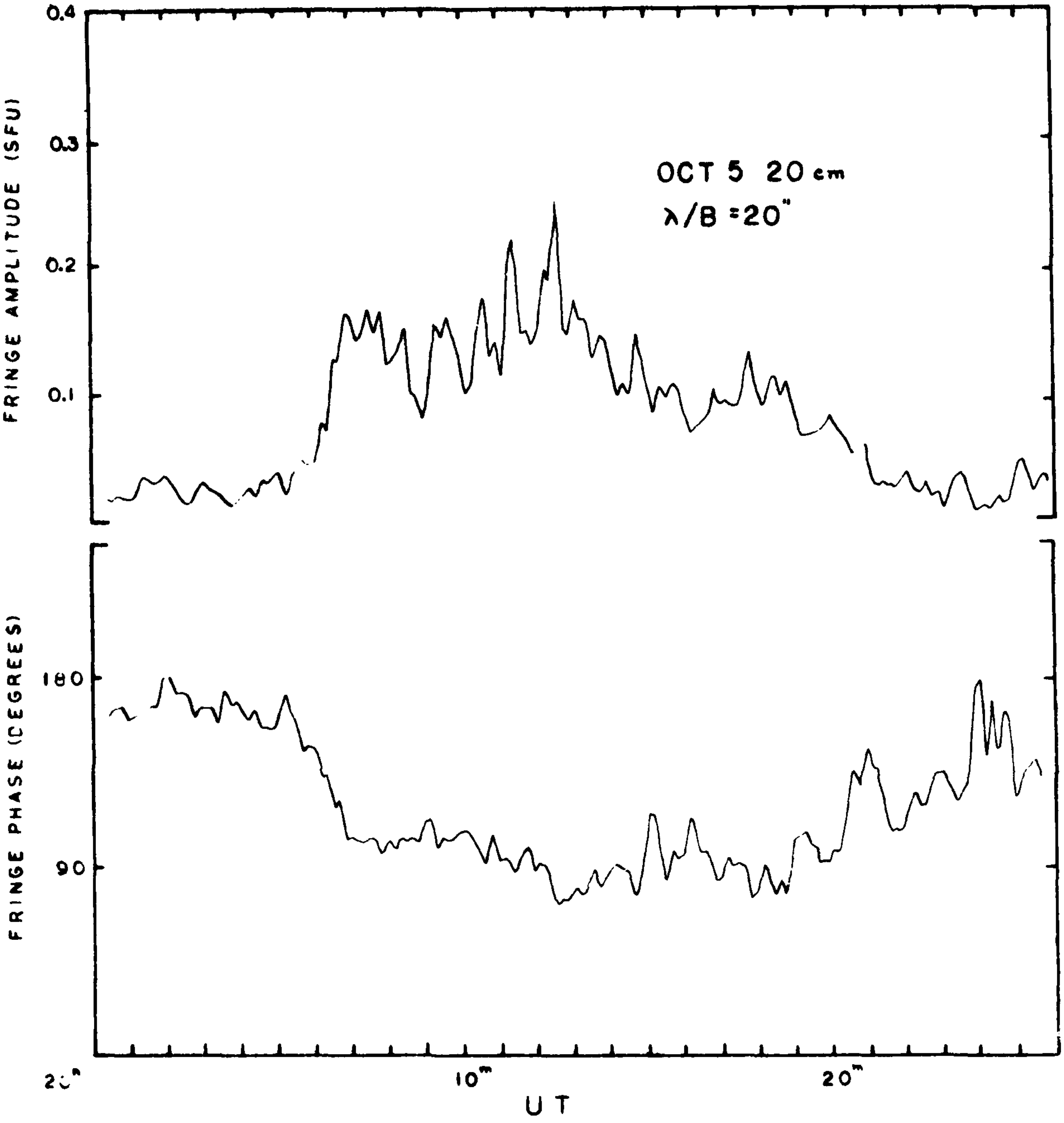

Figure 24. A comparison of the amplitude and phase during a multiple component burst at 20 cm wavelength. There is no detectable phase change between successive components indicating that the position of the emitter does not change, and that several emitters or one moving emitter are ruled out.

AD-A126 640 THREE DIMENSIONAL STRUCTURE AND TIME DEVELOPMENT OF RADIO EMISSION FROM S..(U) TUFTS UNIV MEDFORD MA DEPT OF PHYSICS K R LANG 15 JAN 83 AFGL-TR-83-0018

2/2

UNCLASSIFIED F19628-80-C-0090 F/G 3/2 NL

END
DATE
FILMED
5 83
DTIC

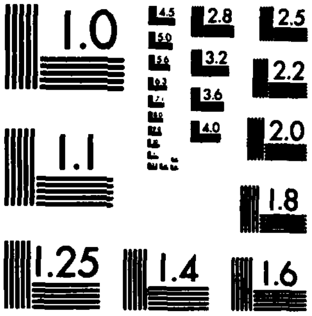
1.0
4.5
5.0
5.6
6.3
7.1
8.0
2.8
3.2
3.6
4.0
2.5
2.2
2.0
1.1
1.8
1.25
1.4
1.6

that the degree of circular polarization remained constant at 80±15% throughout the entire sequence of events. The nonvarying properties of the relative fringe amplitudes, phase and circular polarization are all suggestive of a single emitting source, and, although this conclusion remains somewhat speculative, the results are indicative of the potential use of the V.L.A. in understanding the nature of burst sources.

3.2 HIGH RESOLUTION OBSERVATIONS OF SOLAR RADIO BURSTS AT 2, 6 AND 20 CENTIMETERS WAVELENGTH

3.2.1 Introduction

Solar radio bursts can now be studied with second-of-arc resolution by using the Very Large Array (V.L.A.) and the Westerbork Synthesis Radio Telescope (W.S.R.T.). In addition to providing new information on the sizes, locations and brightness temperatures of the radio bursts, the radio synthesis maps can be compared with the optical wavelength data at comparable time intervals and angular resolutions. Furthermore, the V.L.A. and the W.S.R.T. are capable of measuring the radio polarization with high angular and time resolution, thereby providing information about the evolution of the magnetic fields in the bursting regions. All of this information is, of course, vital to our understanding of the origin, development and prediction of solar bursts.

Previous V.L.A. observations of solar bursts indicate that 6 cm bursts often occur above magnetic neutral lines located between sunspots[8,96], and that both the 2 cm and 6 cm emission are frequently located in the central regions of magnetic arches located between flaring Hα kernels[97,116]. These results imply that the energy release at radio wavelengths occurs near the apex of the magnetic loops. More recent V.L.A. observations indicate that in some cases the 6 cm emission is most intense at the footpoints of magnetic loops[117,118,119]. This is consistent with the W.S.R.T. observations of complex 6 cm bursts occurring in the widely separated footpoints of

---

116. Marsh, K.A. and Hurford, G.J. (1980), Two-dimensional VLA maps of solar bursts at 15 and 23 GHz with arcsec resolution, Ap. J. Lett. 240: L111-L114.

117. Kundu, M.R., Bobrowsky, M. and Velusamy, T. (1982), VLA observations of positions of 6 centimeter burst peaks associated with hard X-ray burst spikes, Ap. J. 251: 342-351.

118. Kundu, M.R., Schmahl, E., Velusamy, T. and Vlahos, L. (1982), Radio imaging of solar flares using the Very Large Array: new insights into the flare process, Astr. Ap. 108:188-194.

119. Kundu, M.R., Schmahl, E. and Velusamy, T. (1982), Magnetic structure of a flaring region producing impulsive microwave and hard X-ray bursts, Ap. J. 253: 963-974.

coronal loops[120]. The observations presented in Section 3.2.3 indicate that the solar radio bursts at 6 cm and 20 cm wavelength are usually located at the apex of magnetic loops rather than at their footpoints.

Radio interferometric observations can also provide valuable information about the changing magnetic topology before and during the radio bursts. Of special interest are the burst precursors observed in the form of increased intensity and polarization before burst emission. Lang[30] has, for example, called attention to dramatic changes in circular polarization which occur on times scales of about one hour before the emission of solar bursts. More recent V.L.A. polarization maps at 6 cm wavelength[117] indicate that the structure of the polarized emission and hence the magnetic field topology, undergoes changes prior to and during radio bursts. These observations are related to models which involve changing magnetic field configurations to explain the release and source of flare energy[121,122,123,124]. Recent V.L.A. observations at 6 cm wavelength[117,118,119] indicate that the locations of different peaks of multiple bursts are the same to within ±2", although the polarization is not always the same for different peaks. Lang, Willson and Felli[8] have shown that the size, position and circular polarization remain constant during the emission of successive 20 cm bursts. This suggests that one source is emitting the sequence of events, and that the energetic electrons are being accelerated in the same magnetic region of the loop. In Section 3.2.4 we also provide new information on the locations and changing magnetic fields of single and multiple wavelength bursts.

The sizes, brightness temperatures, locations, polarizations and time evolution of eight solar bursts have been specified using V.L.A. and W.S.R.T. observations. In Section 3.2.2 we describe our observational procedures and present our basic results on angular sizes and brightness temperatures. In Section 3.2.3 we present a series of 10 s snapshot maps made during more intense bursts and compare them with simultaneous Hα photographs. We thereby establish the site of energy release while also providing evidence for preburst heating. In Section 3.2.4 we discuss a burst which exhibited dramatic changes in its polarization structure and discuss the

---

[120] Kattenberg, A. (1981), Solar radio bursts and their relation to coronal magnetic structures, Ph.D. Thesis, University of Utrecht, The Netherlands.

[121] Gold, T. and Hoyle, F. (1960), On the origin of solar flares, M.N.R.A.S. 120: 89-105.

[122] Heyvaerts, J., Priest, E.R. and Rust, D.M. (1977), An emerging flux model for the solar flare phenomenon, Ap. J. 216:123-137.

[123] Rust, D.M. (1972), Flares and changing magnetic fields, Solar Phys. 25: 141-157.

[124] Rust, D.M. (1976), An active role for magnetic fields in solar flares, Solar Phys. 47:21-40.

possible physical conditions which give rise to these changes. A summary of our results is given in Section 3.2.5.

3.2.2 Summary of Burst Properties

We have used the V.L.A. and W.S.R.T. to observe eight bursts on five days between March 1980 and June 1981. The wavelengths of observation, antenna configurations and synthesized beamshapes are given in Table 6. At the V.L.A., the individual antennae have diameters of 25 m, which at $\lambda = 2$, 6 and 20 cm, respectively, provide half-power beamwidths of 3.0', 9.3' and 31.1'. The W.S.R.T. antennae have individual diameters of 26 m which provide a 9.5' field of view at 6 cm wavelength. At the V.L.A. the average correlated signal of $N(N-1)/2$ interferometer pairs, where N is the number of antennea used on each day, was sampled every 10 s for both the left-hand circularly polarized (LCP) and the right-hand circularly polarized (RCP) signals, thereby providing the data needed to compute maps of total intensity $I = (LCP+RCP)/2$ and the Stokes parameter $V = (LCP-RCP)/2$. The bandwidth used in every case was 12.5 MHz. At the W.S.R.T. the average correlated flux of 40 interferometer pairs was sampled every 0.1 s for both the total intensity, I, and circular polarization, V.

Table 6. Summary of Observational Parameters for Eight Solar Bursts.

Date	Instrument	Wavelength	Number of Antennae	Baseline range (km)	Synthesized beamshape ("x")
March 20, 1980	V.L.A.	2 cm	10	0.10-1.95	2.2 x 3.1
June 12, 1980	V.L.A.	20 cm	11	0.08-13.60	6.8 x 12.6
Sept. 4, 1980	V.L.A.	6 cm	22	0.04-1.95	5.8 x 7.4
June 13, 1981	V.L.A.	6 cm	26	0.13-6.40	4.2 x 5.5
June 14, 1981	V.L.A.	20 cm	26	0.13-6.40	7.8 x 9.2
June 13, 1981	W.S.R.T.	6 cm	14	0.05-2.71	4.6 x 600

The V.L.A. data were calibrated by observing either NRAO 150 or PKS 0923 + 392 for 5 minutes every 30 minutes. The flux density of NRAO 150 was assumed to be 10.5, 10.2 and 5.5 Jy at 2, 6 and 20 cm, respectively, while the respective flux densities of PKS 0923 + 392 were taken to be 7.65, 7.36 and 8.53 Jy. The amplitude and phase of the correlated signal were calibrated according to the procedure described by Lang and Willson[38] together with a correction for the differences in the signal from high temperature noise sources detected in each polarization channel. Details of the observing and calibration procedure at the W.S.R.T. are given by Bregman[56].

Here, the interferometric phases were calibrated by observing Cassiopeia A whose flux density at 6 cm wavelength was assumed to be 745 Jy. The uncertainty in the calibration at both the V.L.A. and the W.S.R.T. is estimated to be ≤ 5° in phase and ≤ 10° % in amplitude.

A summary of the observed bursts is given in Table 7, where we provide the date, time and observing wavelength, the active region number, the full angular width to half intensity, peak brightness temperature and maximum degree of circular polarization, $\rho_c = V/I$. The burst was in every case resolved with angular sizes between 5" and 30", peak brightness temperatures between 2×10^7 and 2×10^8 K, and degrees of circular polarization which ranged between 10 and 90%. In Sections 3.2.3 to 3.2.5. we discuss the details of each burst and present snapshot maps which determine the sites of energy release and specify the changing magnetic topology within the bursting regions.

3.2.3 Site of Energy Release and Preburst Heating

Although it is generally believed that solar radio bursts occur through the conversion of magnetic to particle energy within a complex network of coronal loops, the exact location of the sites of energy release within the loop structure has only recently been determined. As discussed in Section 3.2.1, radio bursts at 2 cm and 6 cm wavelength are usually located at the central regions of magnetic loops, but there are some examples in which the 6 cm burst emission is strongest near the footpoints of the loops. For those cases in which we could compare the positions of the radio bursts and optical features, we found that the radio emission originates near the center of magnetic loops, rather than at the footpoints. In Figure 25 we compare a 10 s snapshot map of the impulsive phase of a burst observed at 6 cm wavelength with both a map of the preburst radio emission (A) made three minutes before the peak of the burst and an Hα photograph taken at the same time. The figure indicates that the radio burst was elongated in a direction joining the two bright Hα kernels, and that it was most intense at a point located midway between them. The preburst radio emission (A) was contained within a looplike structure which also joins the sites of subsequent Hα emission. Here the peak brightness temperature is $\sim 5.5 \times 10^6$ K as compared with the peak burst brightness temperature of 4.2×10^7 K. Because the brightness temperature of quiescent coronal emission at 6 cm is typically $\sim 2 \times 10^6$ K,[2,34] the somewhat higher temperature observed in the preburst loop could represent pre-burst heating of the coronal plasma. In order to check that the brightness temperature was in fact higher than normal at this time, we also made several maps of 10 minutes duration centered around one hour before the burst. We found that the radio source had a similar size and shape but that the peak brightness tempera-

Table 7. Observed Parameters of Eight Radio Wavelength Flares.

DATE	TIME (U.T.)	WAVELENGTH	ACTIVE REGION	ANGULAR SIZE (" x ")	MAXIMUM BRIGHTNESS TEMPERATURE (°K)	MAXIMUM CIRCULAR POLARIZATION (%)
March 20, 1980	2040-2100	2 cm	AR 2339	5 x 5	2.1×10^7	80
June 12, 1980	1339-1344	20 cm	AR 2509	16 x 35	1.5×10^8	~ 100
June 12, 1980	1454-1455	20 cm	AR 2511	15 x 15	2.0×10^8	75
Sept. 4, 1980	2215-	6 cm	AR 2645	15 x 30	4.2×10^7	60
June 13, 1981	1142-1155	6 cm	AR 3159	~ 8	-	< 10
June 13, 1981	2156-2158	6 cm	AR 3159	5 x 10	2.7×10^7	$\lesssim 15$
June 14, 1981	2041-2049	6 cm	AR 3159	5 x 17	2.6×10^7	25
June 14, 1981	1510-1512	20 cm	AR 3159	10 x 25	5.5×10^7	< 15

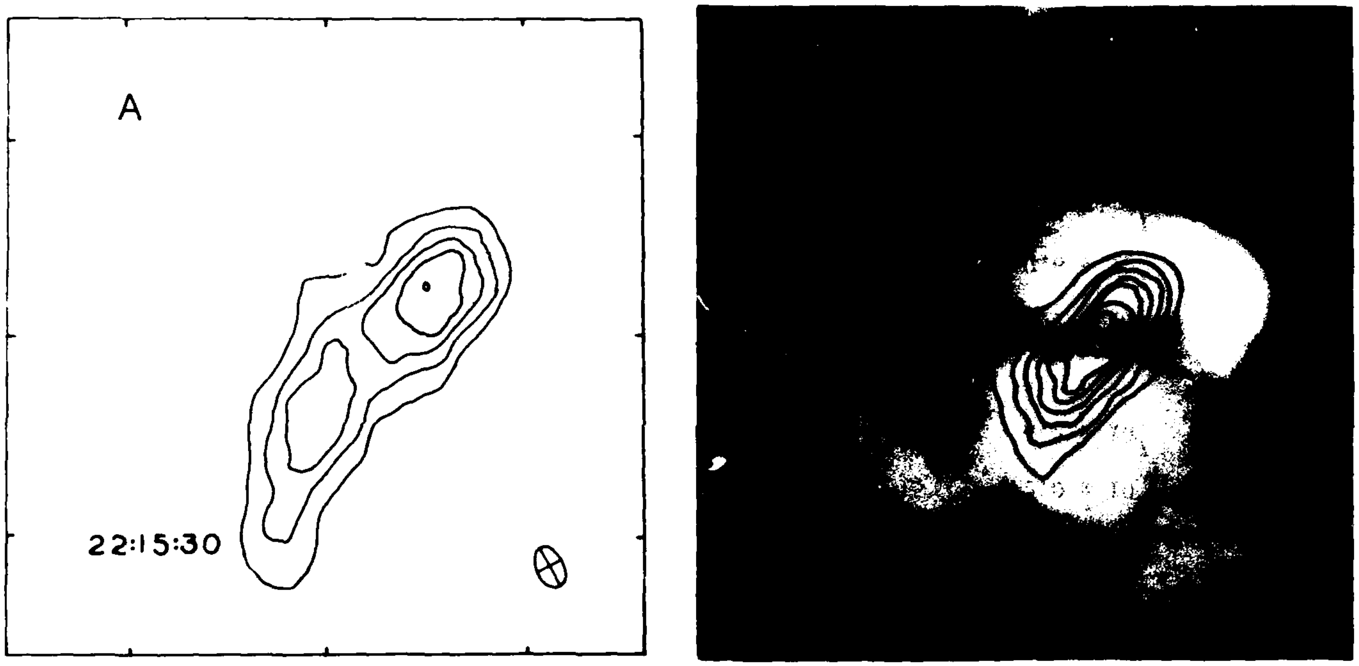

Figure 25. V.L.A. synthesis maps of the preflare (A) and impulsive phase (B) of a burst detected at 6 cm wavelength on September 4, 1980. Each map of total intensity, I, was made from 10 s of data at the time indicated. The contours of both maps mark levels of equal brightness temperature. For A, the contours are drawn at 1 x 10^6, 2 x 10^6......5 x 10^6 K, while for B, the contours are drawn at 5.5 x 10^6 K, 1.1 x 10^7...3.8 x 10^7 K. Note that the burst emission spans the region between the two Hα kernels and is most intense between them. The Hα photograph was taken at the Big Bear Solar Observatory (courtesy Frances Tang).

tures were more than a factor of two lower with values of about 1.7×10^6 K. We therefore believe that we have detected preburst heating which occurs minutes before burst emission. Unfortunately the Solar Maximum Mission satellite was not observing this active region at the time of the burst and so we cannot check to see if there was also an enhancement of soft X-ray emission at the footpoints of the loop. We also note that Kundu et al.[117,118,119] have also found evidence for heating of the plasma in coronal loops before the impulsive phase of a 6 cm burst.

The fact that the preburst radio emission lies closer to the Hα emission than the peak of the impulsive burst suggests that the plasma is heated at a lower level than the site of the burst emission. The location of the impulsive phase is in agreement with the theoretical models in which the primary release of energy occurs at the top of a magnetic loop[125,126,127,128].

In Figure 26 we compare the impulsive phases of two other radio bursts with Hα photographs taken at the same time. The 2 cm (A) burst has a size of ∿ 5" and is located near the center of the Hα emission, which is itself located between two groups of sunspots. Another 6 cm burst (B) consists of two components, both displaced by about 10" to the southeast of the Hα emission. We attribute the angular displacement between the radio and optical sources as a radial, limbward displacement caused by the greater height of the 6 cm burst emission. Both the eastward component of the displacement (∿ 10") and the southward component (∿ 10") indicate a height of $\sim 1.5 \pm 0.2 \times 10^9$ cm for the 6 cm emission above the photosphere (the active region coordinates were 26°S 32°E).

In Figure 27 we present the time profile of another 6 cm burst whose 10 s snapshot maps are given in Figure 28. The sequence of maps, which were made before, during and after the impulsive phase of the burst, indicate that the impulsive component is smaller and spatially separated from both the preburst radio emission and the gradual decay component of the burst. The gradual decay component is about 10" in size and 30% left circularly polarized, while the impulsive component is $\leq 3"$ in size and less than 15% circularly polarized. An examination of a series of

---

125. Vlahos, L. and Papadopoulos, K. (1979), Collective plasma effects associated with the continuous injection model of solar flare particle streams, Ap. J. 233:717-726.

126. Emslie, A.G. and Vlahos, L. (1980), Radiation signatures from a locally energized flaring loop, Ap. J. 242:359-373.

127. Petrosian, V. (1982), Structure of the impulsive phase of solar flares from microwave observations, Ap. J. Lett. 255:L85-L89,

128. Holman, G.D., Kundu, M.R. and Papadopoulos, K. (1982), Electron pitch angle scattering and the impulsive phase microwave and hard X-ray emission from solar flares, Ap. J. 257:354-360.

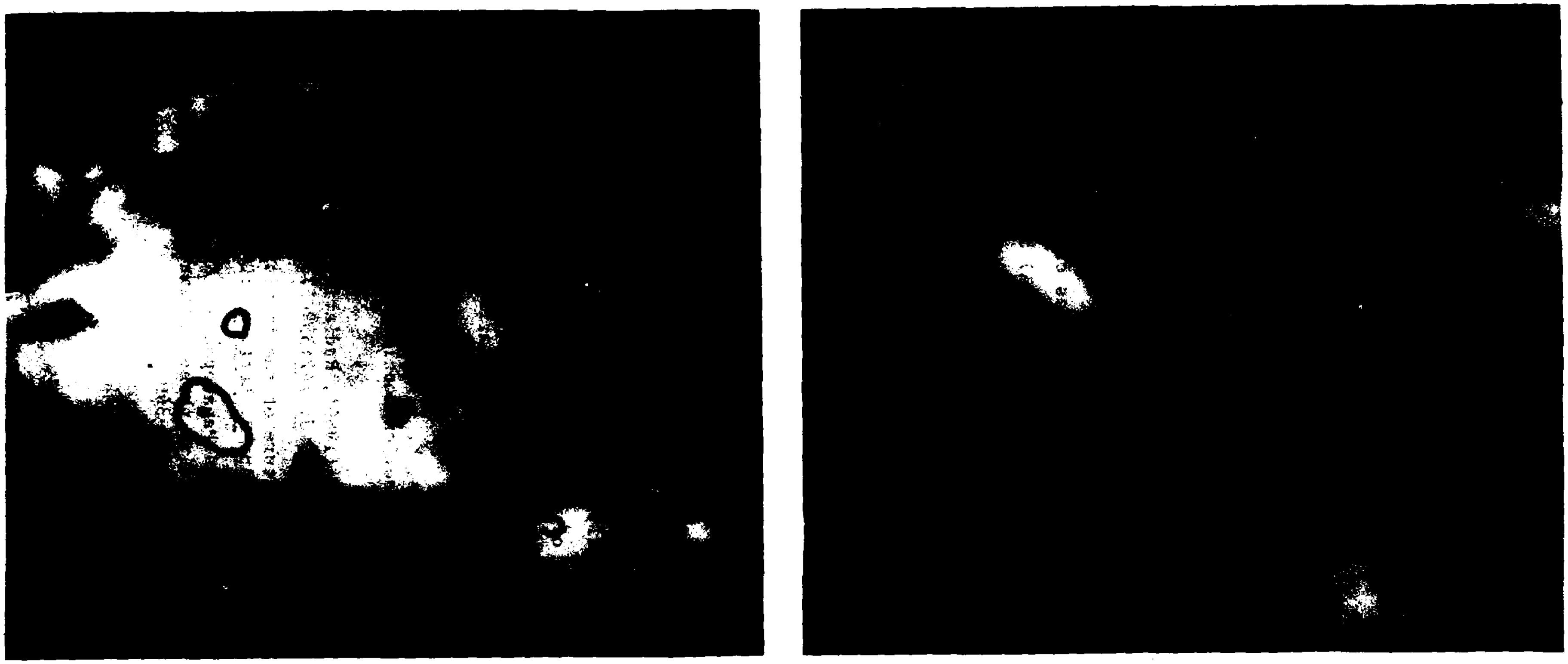

Figure 26. V.L.A. synthesis maps of the total intensity, I, of the impulsive phases of two bursts observed at $\lambda = 2$ cm on March 20, 1980 (left) and at $\lambda = 6$ cm on June 14, 1981 (right). The 2 cm burst source is located between two groups of sunspots suggesting that the burst was located near the apex of a magnetic coronal loop which joins the spots. The 10" southeastward displacement of the 6 cm radio source relative to the $H\alpha$ flare emission is attributed to a radial, limbward displacement caused by the greater height of the radio source.

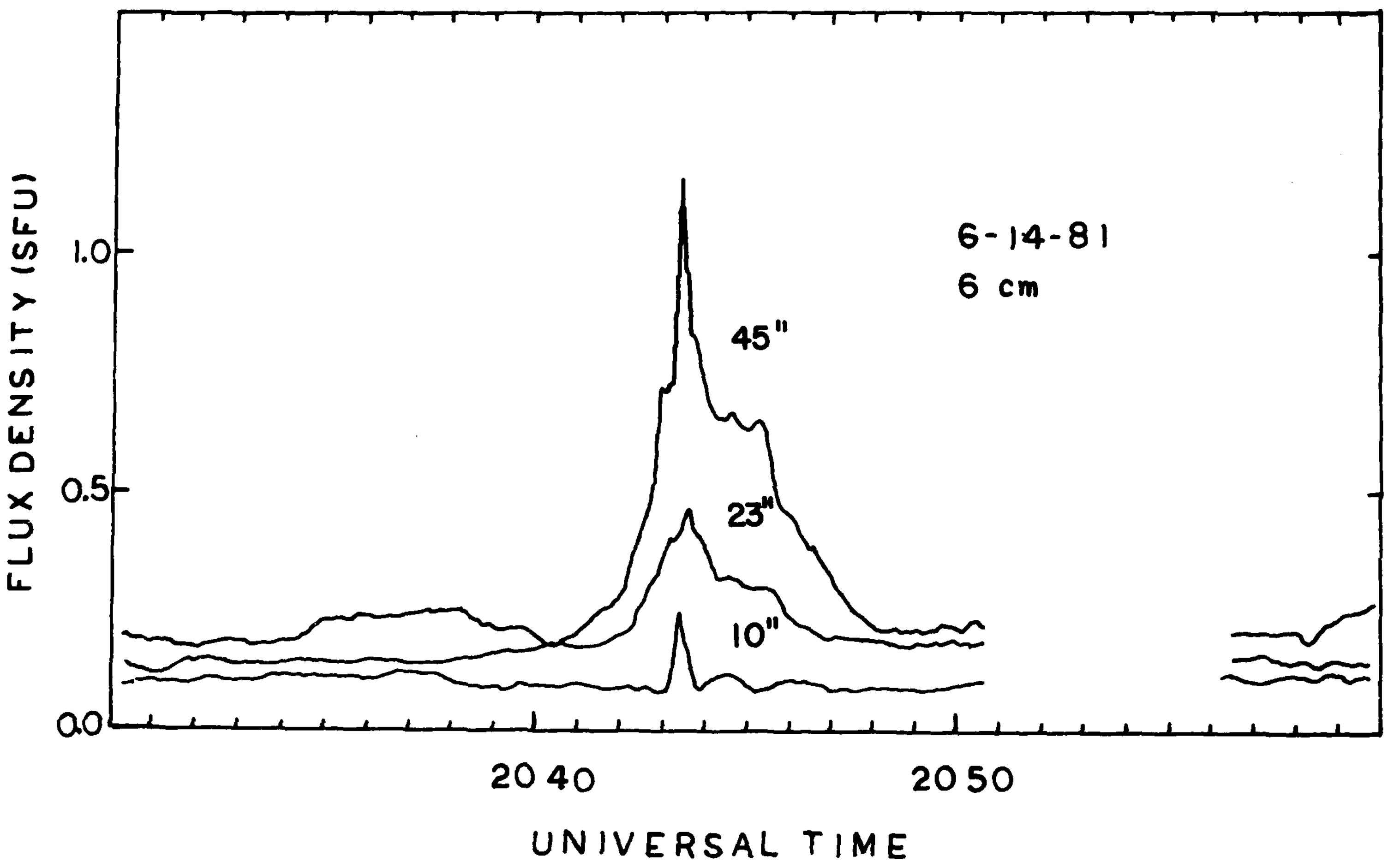

Figure 27. The fringe amplitude of the total intensity, I, versus time for a burst detected at 6 cm wavelength with the V.L.A. on June 14, 1981. The angular resolution of each interferometer pair is given next to the time profile. The visibility data from 325 interferometer pairs were used to construct the two-dimensional synthesis maps of the burst, shown in Figure 28.

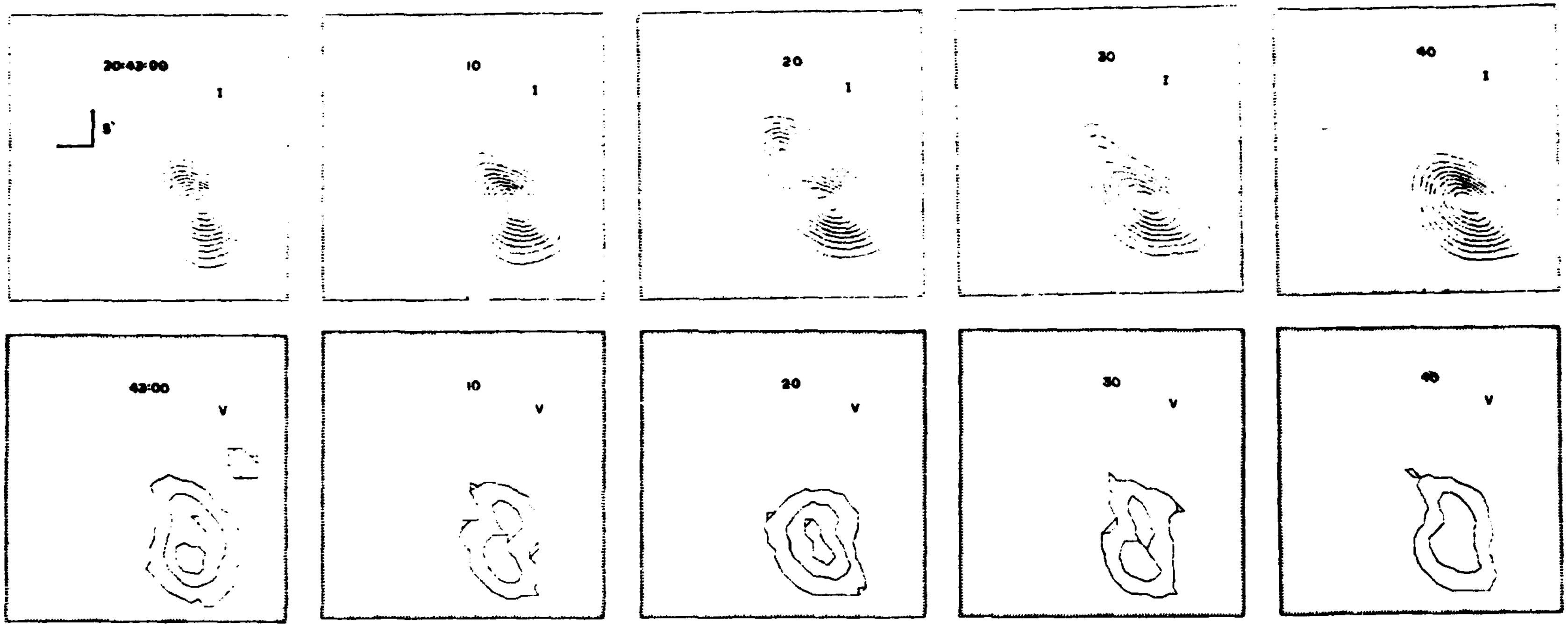

Figure 28, A series of 10 s V.L.A. snapshot maps of the total intensity, I (top), and circular polarization, V (bottom) for a burst detected at 6 cm wavelength on June 14, 1981. The contours of the I maps mark levels of equal brightness temperature and correspond to 2.8×10^6, $5.5 \times 10^6 \ldots 2.5 \times 10^7$ K. The contours of the V maps also mark levels of equal brightness temperature and are drawn at 2.8×10^6, $5.5 \times 10^6 \ldots 8.3 \times 10^6$ K. Note especially the spatial separation of the impulsive and gradual components of the burst at 20:43:20 U.T..

Hα pictures taken at the Big Bear Observatory showed that the optical emission originated closer to the large sunspot shown in Figure 26 and developed in the northeastward direction, roughly coinciding with the elongation of the radio image. The absence of circular polarization in the impulsive component suggests that this source is located near the apex of the loop where the longitudinal component of the magnetic field is small, whereas the polarization detected in the gradual decay component suggests an origin in a predominantly longitudinal magnetic field of one polarity, most likely in one leg of the loop.

In Figure 29 we have superimposed a 10 s snapshot map of a 20 cm burst on a magnetogram (provided by Jean Rayrole of the Meudon Observatory) showing the longitudinal component of the magnetic field in the underlying photosphere. The radio burst is located between the regions of opposite magnetic polarity and extends along the magnetic neutral line. A 20 cm synthesis map of the active region made fr four hours of observation on the same day shows a hot ($\sim 10^6$ K), looplike stru re which connects the regions of opposite polarity. The apex of this 20 cm coron loop coincides with the location of the burst. We found no detectable preflar heating of the coronal loop before this burst. The maximum brightness tempera of the preflare active region was $\sim 2.5 \times 10^6$ K and did not vary by more than ∿ 25% on timescales of a few minutes to several hours before the burst occurred.

In Figure 30 we show the time profile of a multiple-component 6 cm burst whose individual components had durations of 20 to 60 seconds. In order to separate the burst structure from that of the quiescent active region we first subtracted the preburst visibility function from the burst data. Maps were then constructed from a 1.0 s average of the corrected visibility function obtained from the 40 available baselines. Because the W.S.R.T. is a linear array, these maps gave the one-dimensional brightness distribution of the source integrated perpendicular to a line with a position angle of ∿ 5° east of north on the sky. In Figure 31 we display these maps at various times throughout the burst. The data indicate that all the burst components originate from a single source of about 10" in size whose position remains constant to within a few arc seconds. This is similar to the observations of Lang, Felli and Willson[8], which indicated that the size, position and circular polarization remained constant during the emission of successive 20 cm events in the same burst. A comparison of the 6 cm burst position with a Kitt Peak magnetogram indicated that the radio burst was located within ±5" of the neutral line of the active region. This is consistent with the absence of circular polarization throughout the 6 cm burst, which suggests that the source was located in a region of weak longitudinal magnetic field.

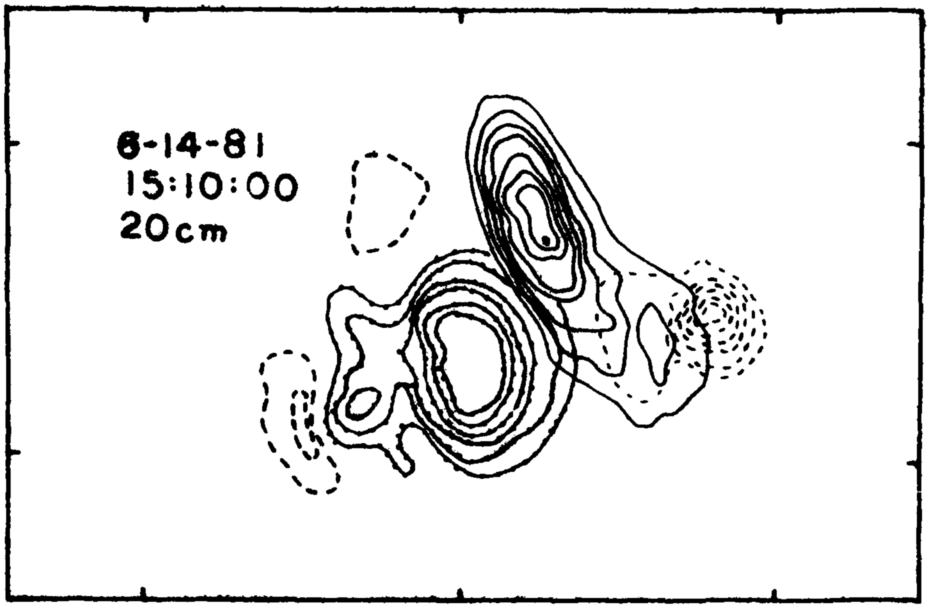

Figure 29. A V.L.A. snapshot map of the total intensity, I, of a burst detected at 20 cm wavelength on June 14, 1981, superimposed on a magnetogram showing the longitudinal component of the magnetic field in the underlying photosphere. Here, the angular scale is denoted by the 60" spacing between the fiducial marks on the axes. The contours of the radio map mark levels of equal brightness temperature and are drawn at 1.2×10^7, $1.8 \times 10^7 \ldots 5.5 \times 10^7$ K. The dashed contours of the magnetogram denote levels of negative longitudinal field and are drawn at -200, -400, -600, -800, -1000 and -1500 gauss. The dotted contours of the magnetogram denote levels of positive field and are drawn at 100, 200, 400, 600, 800, 1000 and 1500 gauss.

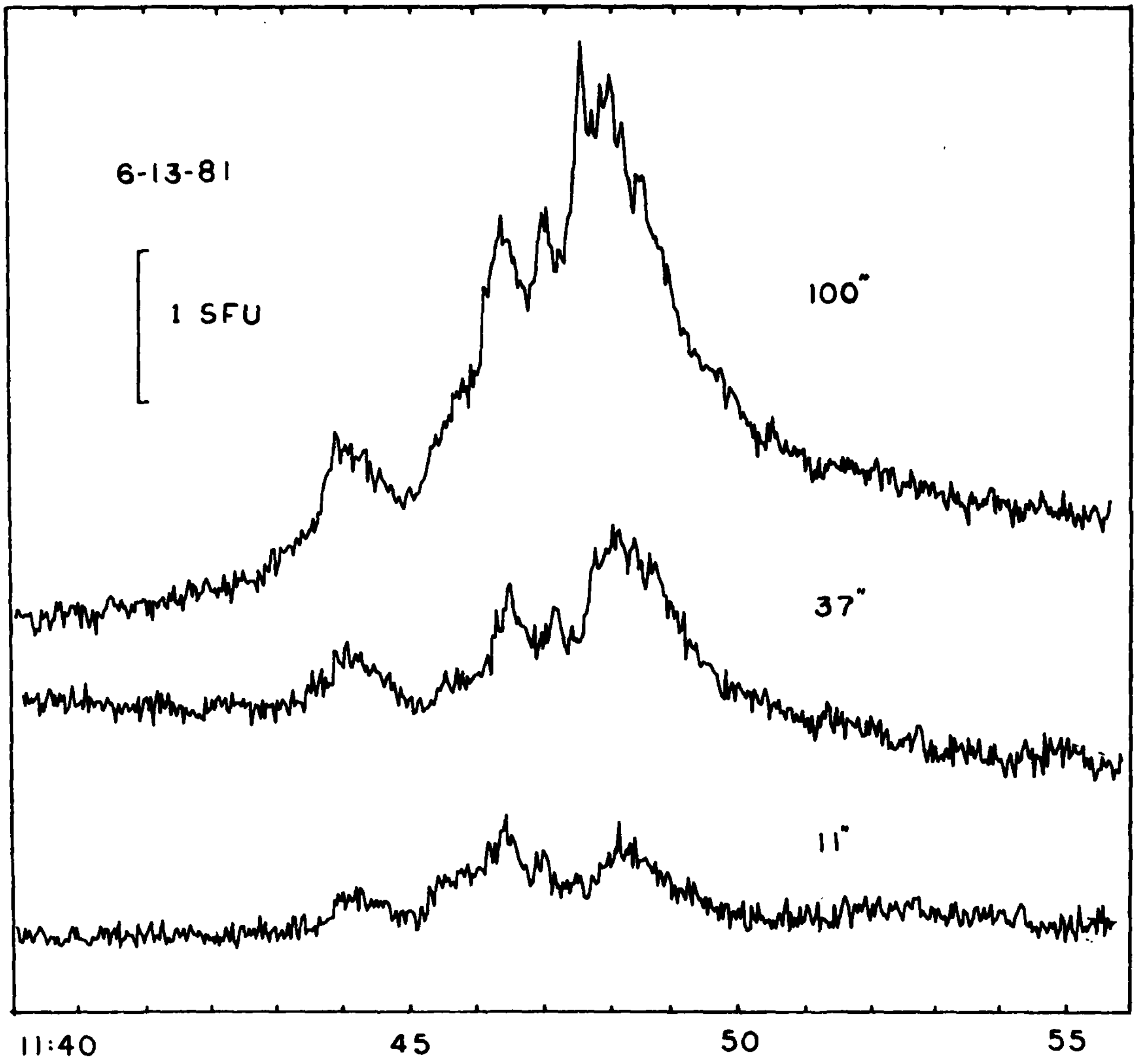

Figure 30. The time profiles of a complex burst observed at 6 cm wavelength with the W.S.R.T. on June 13, 1981. Each profile was detected with one interferometer pair whose angular resolution is given next to the profile. The combined fringe visibilities of 40 interferometer pairs were used to construct one-dimensional snapshot maps throughout the burst.

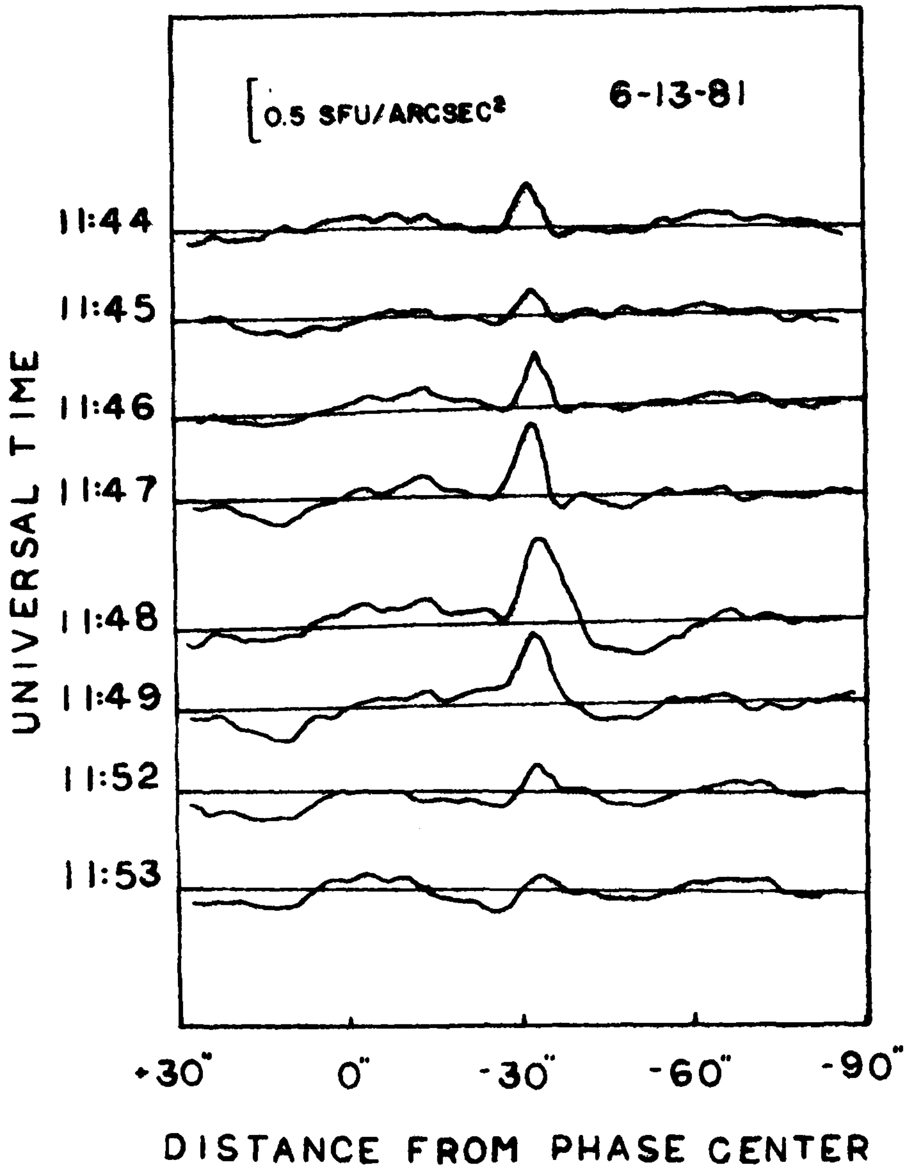

Figure 31. A sequence of one dimensional fan beam scans of the total intensity, I, for a burst detected at 6 cm wavelength with the W.S.R.T. on June 13, 1981. Each scan was constructed from a 1 s average of the visibility data from 40 interferometer pairs. The scans indicate that the burst originates from a source of about 10" in size, whose position remains constant to within a few arc seconds.

3.2.4 Polarization Changes

High resolution radio interferometric observations have led to the discovery of a high degree of circular polarization for both the slowly varying component and the burst component of active regions. The high polarization is attributed to either propagation effects or to gyroemission of energetic electrons. Both mechanisms require strong magnetic fields of several hundred gauss in strength. The high brightness temperatures of the radio emission ($\sim 10^6$ K) indicates that the relevant magnetic fields are in the low solar corona. Previous studies of the evolution of the magnetic fields in the underlying photosphere suggest that some change in the magnetic field topology triggers the emission of solar bursts; but it is probably the coronal magnetic field which supplies the energy for solar bursts. Lang[30] has, for example, shown that the degree of circular polarization of the coronal radioemission can increase to 100% about 10 minutes to one hour before the eruption of solar bursts. Kundu et al.[117,118,119] have similarly detected dramatic changes in circular polarization before and during a complex flare observed at 6 cm with the V.L.A.. About 10 minutes before the onset of the impulsive phase, the magnetic structure changed from a simple bipolar region to a more complicated quadrupolar configuration, suggesting the appearance of a new system of coronal loops accompanied by the generation of additional magnetic flux.

The time profiles of the total intensity, I, and circular polarization, $\rho_c = V/I$, of a 20 cm burst are given in Figure 32. It consists of three impulsive spikes, each of 10 to 20 s duration, superimposed on a more gradual burst lasting about 12 minutes. The lower part of the figure shows that the first impulsive spike is highly right circularly polarized while the other two impulsive spikes are highly left circularly polarized. In Figures 33 and 34 we display a series of snapshot maps of both I and V made at 10 s intervals. Near the beginning of the burst at 13:40:00 U.T., the slowly varying source has a size of $\sim$ 30" and is $\sim$ 25% left circularly polarized in the eastern half of the source. The polarized structure changes dramatically during the first impulsive spike, becoming about 90% right circularly polarized in the western half of the region, then reverting back to its unpolarized pre-impulsive state 10 s later. The polarization structure changes again at 13:40:50 and 13:42.50 U.T. when the source becomes more elongated and develops two left circularly polarized spikes ($\rho_c \sim$ 50-60%) which bracket the previously right circularly polarized spike located near the center of the region. The maximum brightness temperature of the three impulsive spikes ranged from 7×10^7 to 10×10^7 K, whereas the brightness temperature of the more slowly varying source was $\sim 3.5 \times 10^7$ K.

These rapid polarization changes are difficult to explain in terms of a simple

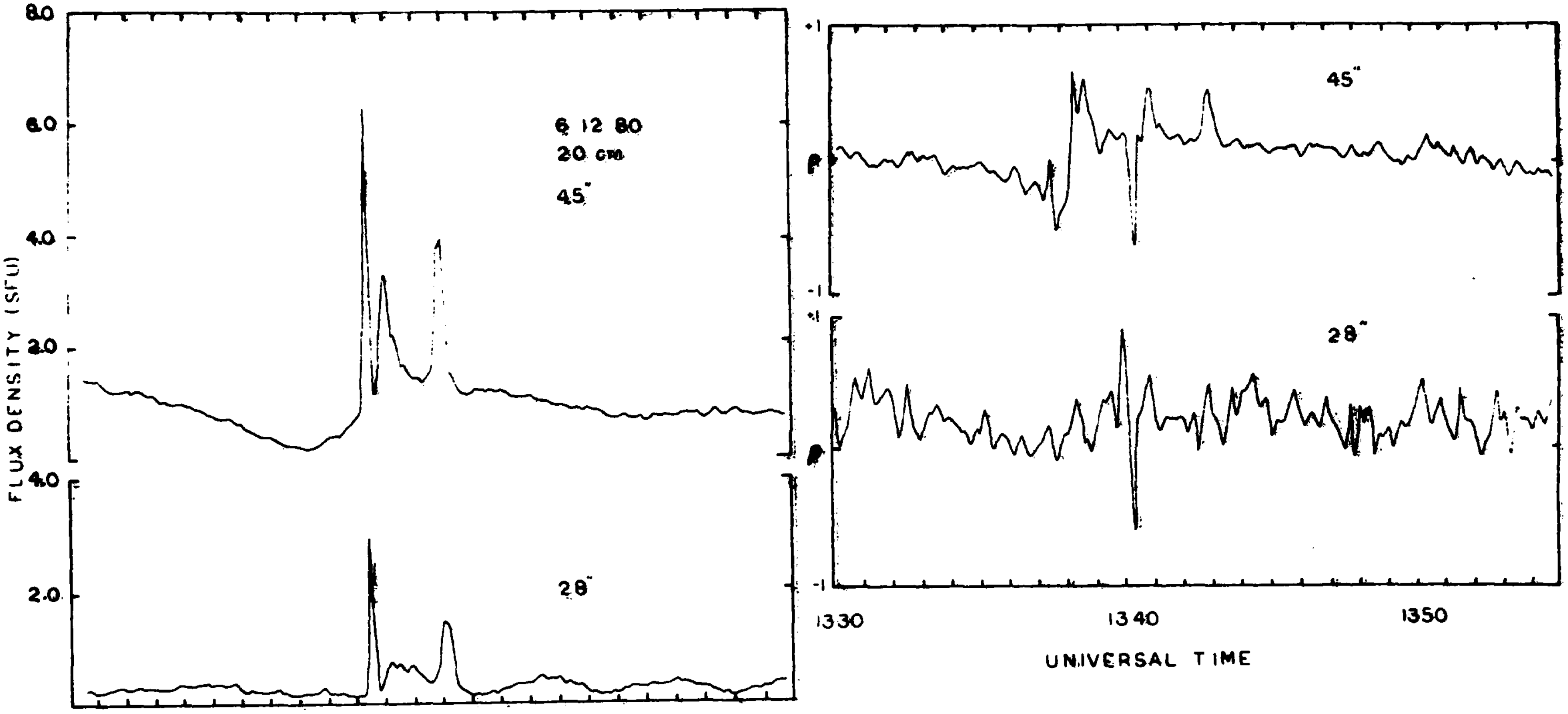

Figure 32. The time profiles of a multiple spike burst detected at 20 cm wavelength with the V.L.A. on June 12, 1980. Here, both the total intensity, I (left), and the circular polarization, p (right), are plotted for two interferometer pairs whose angular resolutions are given above each profile. Note especially the rapid changes in the circular polarization during the impulsive bursts.

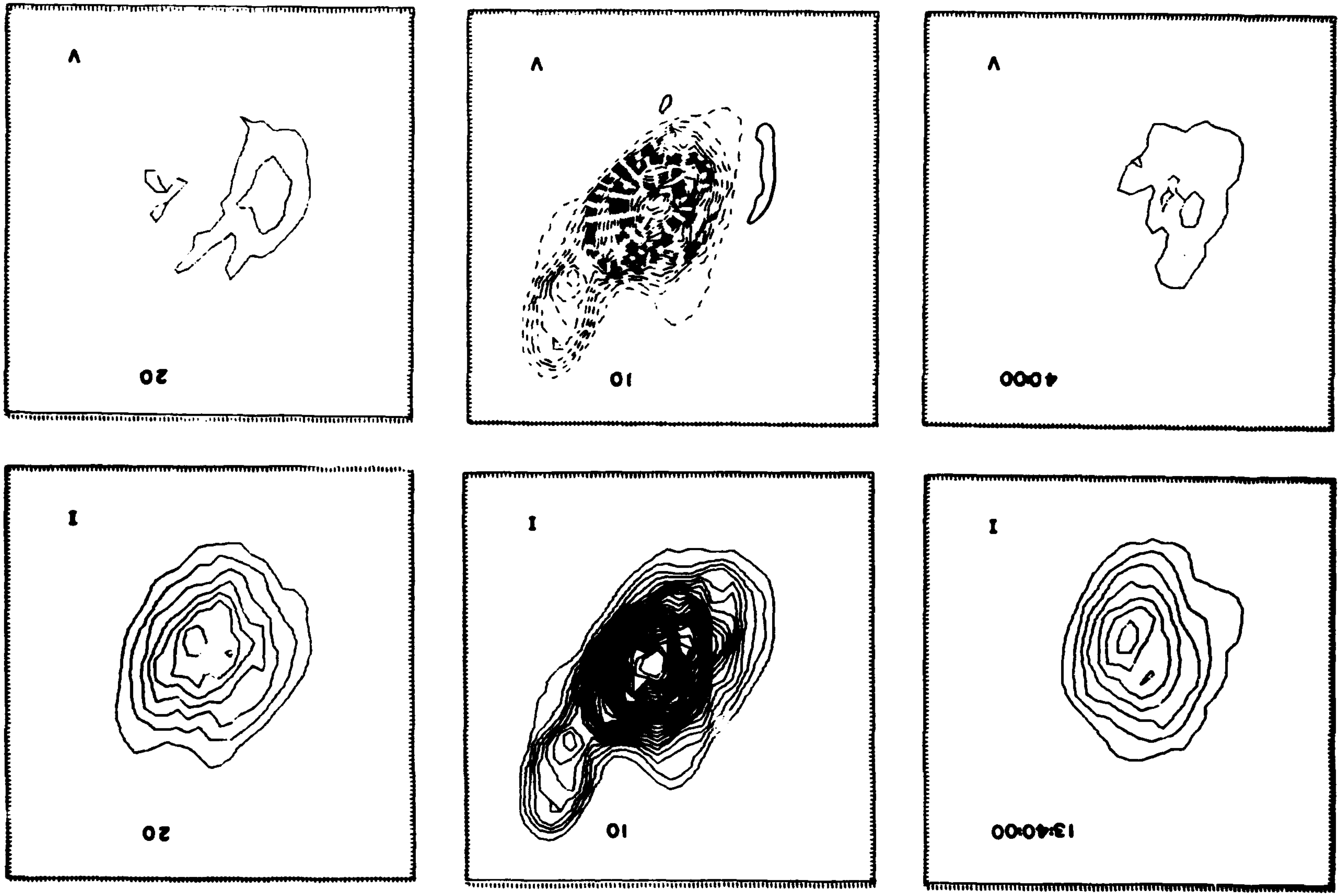

Figure 33. A series of 10 s snapshot maps of both total intensity, I (top), and circular polarization, V (bottom), for a burst observed at 20 cm wavelength with the V.L.A. on June 12, 1980. The contours of the maps mark levels of equal brightness temperature, where the solid and dashed contours of the V maps denote positive and negative values of V, respectively. For both sets of maps the outermost contour and the contour interval are equal to 6.2×10^6 K.

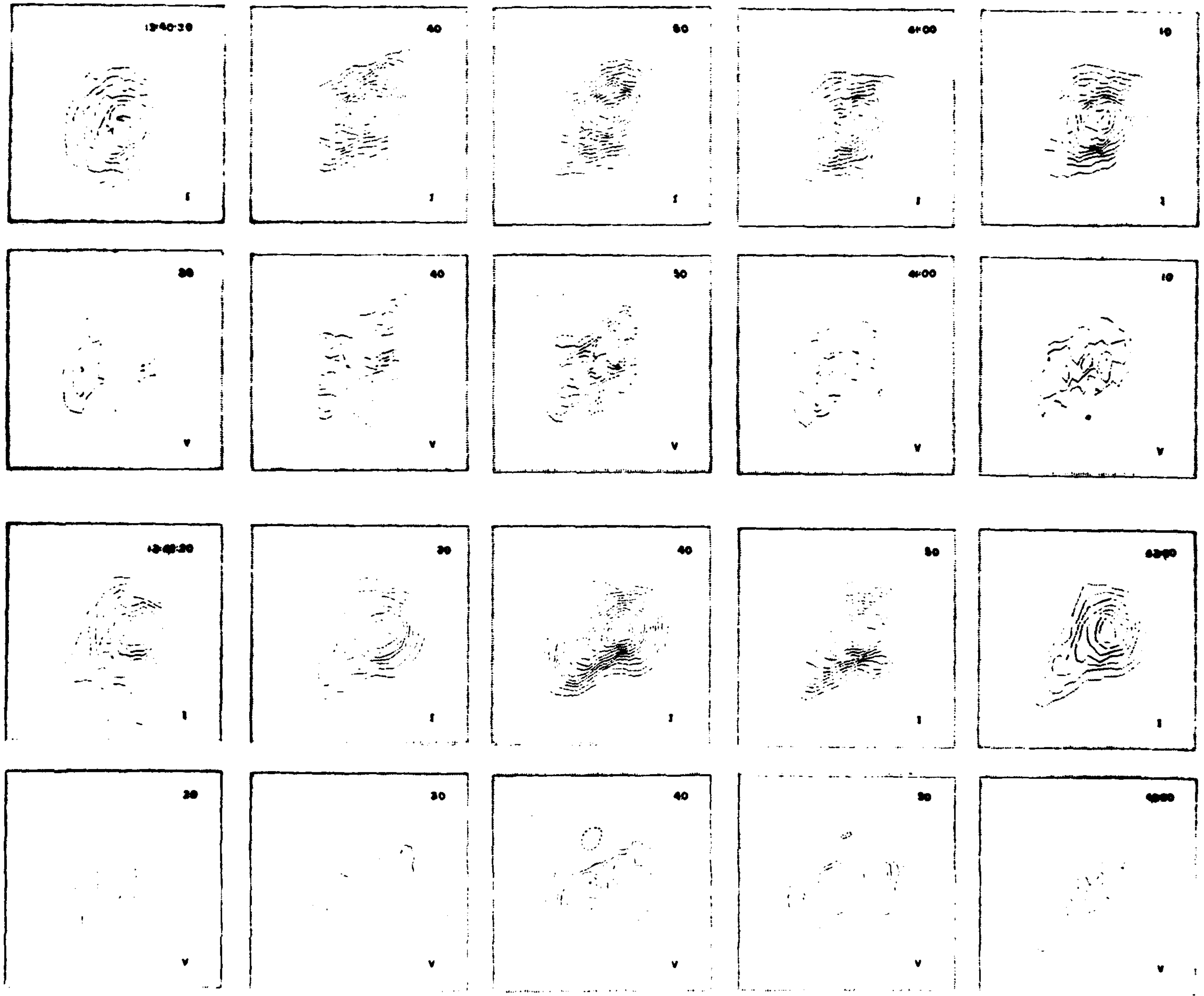

Figure 34. The continuation of Figure 33.

bipolar loop model of the flaring region. Although we do not have any magnetograms with which to compare these changes, it is unlikely that the magnetic structure of the underlying photosphere can change so rapidly. The high degree of circular polarization implies that the burst emission is optically thin. If the emission is due to thermal bremsstrahlung in a region of 30" in size, then the optical depth $\tau_B \sim 0.14$ at 20 cm wavelength for an electron density $N_e \lesssim 2.5 \times 10^{10}$ cm^{-3}. For larger electron densities, the plasma frequency would exceed 1.4 GHz, and the 20 cm radiation would not propagate though the solar atmosphere. For an optically thin condition the observed brightness temperatures of $T_B \sim 10^8$ K imply electron temperatures of $T_e \geq 10^8$ K. The optical depth due to gyroresonant absorption with $T_e \sim 10^8$ K, a magnetic scale length of $L_H \sim 10^9$ cm, and electron densities of $N_e = 10^9$ to 10^{10} cm^{-3} exceeds unity for all harmonics unless the angle, θ, between the magnetic field and the line of sight is less than 10°.[41] We therefore conclude that unless θ is unusually small, the gyroemission will be optically thick, and that the high polarization is probably due to propagation effects of the thermal bremsstrahlung. The observed degrees of circular polarization of 50 to 90% indicate magnetic field strengths of H = 300 to 400 gauss. These values are consistent with those obtained by Felli, Lang and Willson[3] who inferred $H \sim 250$ gauss for the 2×10^6 K plage-associated component of 6 cm radio emission above active regions.

We next attempt to explain the rapid changes in circular polarization which were observed during the impulsive spikes. One explanation involves frequency-dependent propagation effects which change the magnetoionic mode as the radiation passes through a plasma. Another more straightforward explanation involves the release of energy at different locations within the magnetic loop complex, or the generation of new magnetic flux at coronal levels where the radio emission originates. Cohen[129] has described the situation in which radiation of predominantly one magnetoionic component passes through a quasi-transverse region where the longitudinal component of the magnetic field changes sign. At frequencies above some transitional frequency, ν_T, the wave is unaffected by the reversal of the longitudinal field, whereas below ν_T, the two magnetoionic modes will be interchanged, resulting in a reversal in the sense of the circular polarization. The transition frequency is given by[129] $\nu_T^4 = 10^{17} N_e L_H H^3$, where N_e is the electron density, L_H is the scale length of the magnetic field, and H is the magnetic field strength. Assuming $N_e = 10^{10}$ cm^{-3}, $L_H = 10^9$ cm and $\nu_T \geq 1.42 \times 10^9$ Hz, we find $H \geq 2$ gauss. The required magnetic field strength is relatively insensitive to changes in the electron density and the scale length. If the coronal plasma is to be confined within loop-

---

129. Cohen, M.H. (1960), Microwave polarization and coronal magnetic fields, Ap. J. 133:978-1013.

like structures by the ambient magnetic field, however, then the local magnetic pressure must exceed the gas pressure, i.e. $H^2/8\pi \geq 2N_e kT$. This requires $H \geq 20$ to 120 gauss for $T_e = 5$ to 10×10^7 K and $N_e = 10^9$ to 10^{10} cm^{-3}. This indicates that the transitional frequency actually exceeds 1.4 GHz, and that this effect cannot explain the observed polarization changes.

The sense of circular polarization can also change if the source becomes self-absorbed so that only one of the magnetoionic modes becomes optically thick. The frequency of maximum emission, ν_{Sa}, resulting from self-absorption of a nonthermal source is given by[130,131] $\nu_{Sa} \sim 10^{12.5} I_m^{2/5} H^{1/5}$, where I_m is the maximum brightness, expressed in erg cm^{-2}sec^{-1}Hz^{-1}ster^{-1}, and H is the magnetic field strength perpendicular to the line of sight. For $\nu < \nu_{Sa}$, the extraordinary mode is optically thick and the radiation is polarized in the ordinary mode, while for $\nu > \nu_{Sa}$, the source is optically thin and polarized in the extraordinary mode. Such effects could explain our observations if, for example, the number of electrons accelerated during the impulsive phase was different at the sites of the three impulsive bursts, causing one of the burst sources to be self-absorbed. With $I_m = 0.7 \times 10^{-10}$ erg cm^{-2}sec^{-1} Hz^{-1}ster^{-1}, corresponding to $T_B = 1 \times 10^8$ K and with $\nu_{Sa} \geq 1.4 \times 10^9$ Hz, we find $H \geq 3{,}700$ Gauss. Because this lower limit is many times higher than expected for coronal magnetic fields we also conclude that self-absorption cannot explain the observed changes in circular polarization.

One interpretation of the complicated polarization structure is that the burst occurred within a magnetically complicated region containing a number of coronal loops, and that the unipolar nature of the bursts is due to emission from different legs of the loops which have different magnetic polarity. As suggested by Kundu et al.[117,118,119], the polarization changes could also be explained if the coronal magnetic field undergoes variations on timescales of about one minute. Because both gyroresonant absorption and thermal bremsstrahlung depend on the local value of the magnetic field strength, such variations would also modulate the polarization. Alternatively, the rapid variations could be caused by the generation of new magnetic flux at coronal levels. Several modes of burst emission have in fact been proposed in which loops of magnetic flux emerge from below the photosphere to interact with the overlying magnetic field to ultimately produce bursts[122].

3.2.5 Conclusions About Centimeter Wavelength Solar Bursts

We have used the V.L.A. and the W.S.R.T. to construct synthesis maps of eight solar bursts at 2, 6 or 20 cm wavelength. The observations have shown that the flares

---

130. Slish, V.I. (1963), Angular size of radio stars, Nature 199:682.

131. Ramaty, R. and Petrosian, V. (1972), Free-free absorption of gyrosynchrotron radiation in solar microwave bursts, Ap. J. 178:241-249.

are resolved with angular sizes between 5" and 30", brightness temperatures between 2×10^7 and 1×10^8 K, and circular polarizations of up to 90%. Superpositions of the radio images on available Hα photographs or magnetograms show that the impulsive phases of the bursts are usually located between the Hα kernels or close to the magnetic neutral line. These results suggest that the impulsive sources are located near the tops of coronal loops which connect underlying regions of opposite magnetic polarity. A sequence of 10 s snapshot maps for one 6 cm burst revealed that the impulsive source was spatially separated from the component associated with the rise and decay phase of the flare.

We also found evidence for pre-flare heating of a coronal loops minutes before the onset of one burst observed at 6 cm. The brightness temperatures of the pre-burst emission peaks were $\sim 5 \times 10^6$ K, about a factor of two larger than the temperature found one hour earlier. These peaks of enhanced emission were located closer to the underlying Hα footpoints than was the actual burst suggesting that the heating occurred in a region below the site of primary energy release.

The structure of a multiple spike burst detected at 20 cm wavelength exhibited remarkable changes in circular polarization of up to 90% on timescales of 10 to 20 seconds. The polarized emission can be explained as either gyroresonant radiation for which the magnetic field $H \leq 100$ gauss and for which the angle between the field and the line of sight is ≤ 10°, or as the bremsstrahlung of a hot, optically thin plasma with a temperature $T_e \sim 10^8$ K and an electron density $\sim 2 \times 10^9$ cm^{-3}. The bremsstrahlung requires polarization due to propagation effects at frequencies near the gyrofrequency in magnetic fields of strength $H \sim 300$-400 gauss. The most likely explanations for these reversals in polarization are either that the impulsive sources originated at different locations within a magnetically complicated region or that the coronal magnetic topology itself underwent drastic changes during the burst.

REFERENCES

1. Lang, K.R. (1982), Very large array observations of solar active regions, Proc. S.M.Y. Workshop - Crimean Ap. Obs. 1:39-56.
2. Felli, M., Lang, K.R. and Willson, R.F. (1981), Very large array observations of solar active regions I. The slowly varying component, Ap. J. 247:325-337.
3. Lang, K.R. and Willson, R.F. (1982), Polarized horseshoes around sunspots at 6 cm wavelength, Ap. J. Lett. 255:L111-L117.
4. Lang, K.R. and Willson, R.F. (1983), Multiple wavelength observations of flaring active regions, to be published, Proc. XXIV COSPAR.
5. Chiuderi-Drago, F. et al., (1982), Multiple wavelength observations of a solar active region, Solar Phys. 80:71-85.
6. Lang, K.R., Willson, R.F. and Gaizauskas, V. (1983), Very large array observations of solar active regions III. Multiple wavelength observations, to be published Ap. J., April 1983.
7. Lang, K.R., Willson, R.F. and Rayrole, J. (1982), Very large array observations of coronal loops at 20 cm wavelength, Ap. J. 258:384-387.
8. Lang, K.R., Willson, R.F. and Felli, M. (1981), Very large array observations of solar active regions II. Solar bursts, Ap. J. 247:338-347.
9. Willson, R.F. (1983), High resolution observations of solar bursts at 2 cm, 6 cm and 20 cm wavelength, to be published, Solar Phys.
10. Waldmeier, M. and Müller, H. (1950), Die sonnenstrahlung im gebiet von λ = 10 cm, Zs. f. Ap. 27:58-72.
11. Waldmeier, M. (1956), Analyse einer koronalen kondensation, Zs. f. Ap. 40: 221-235.
12. Piddington, J.H. and Minnett, H.C. (1951), Solar radio-frequency emission from localized regions at very high temperatures, Austr. J. Sci. Res. A4:131-157.
13. Newkirk, G. (1961), The solar corona in active regions and the thermal origin of the slowly varying component of solar radiation, Ap. J. 133:983-1013.

14. Covington, A.E. (1949), Circularly polarized solar radiation at 10.7 cm, Proc. I.R.E. 37:407-410.

15. Lehany, F.J. and Yabsley, D.E. (1949), Solar radiation at 1200 mc/s, 600 mc/s and 200 mc/s, Austr. J. Sci. Res. A2:48-62.

16. Denisse, J.F. (1950), Contribution à l'étude des émissions radioelectriques solaires, Ann. d'Ap. 13:181-202.

17. Gelfreikh, G., Korol'kov, D., Rishkov, N. and Soboleva, N. (1959), On the regions over sunspots as studied by polarization observations on centimeter wavelengths, Paris Symposium on Radio Astronomy, R.N. Bracewell, Ed., Stanford University Press, Stanford, pp.125-129.

18. Christiansen, W.N. and Mathewson, D.S. (1959), The origin of the slowly varying component, Paris Symposium on Radio Astronomy, R.N. Bracewell, Ed., Stanford University Press, Stanford, pp.108-117.

19. Christiansen, W.N. et al. (1960), A study of a solar active region using combined optical and radio techniques, Ann. d'Ap. 23:75-101.

20. Stepanov, K.N. (1958), On the damping of electromagnetic waves in a plasma situated in a magnetic field, Soviet Phys.-JETP 8:195-196.

21. Ginzburg, V.L. and Zheleznyakov, V.V. (1959), On the propagation of electromagnetic waves in the solar corona taking into account the influence of the magnetic field, Sov. Astr.-AJ 3:235-246.

22. Zheleznyakov, V.V. (1962), The origin of the slowly varying component of solar radio emission, Sov. Astr. AJ 6:3-9.

23. Kundu, M.R. (1959a), Structures et propriétés des sources d'activité solaire sur ondes centimètriques, Ann. d'Ap. 22:1-100.

24. Kundu, M.R. (1959b), Étude interferometrique des sources d'activité solaire sur 3 cm de longueur d'onde, Paris Symposium on Radio Astronomy, R.N. Bracewell, Ed., Stanford University Press, Stanford, pp.222-236.

25. Kakinuma, T. and Swarup, G. (1962), A model for the sources of slowly varying components of solar radiation, Ap. J. 136:975-994.

26. Lantos, P. (1968), A model for thermal gyromagnetic radio emission from solar active regions, Ann. d'Ap. 31:105-113.

27. Zlotnik, E. Ya. (1968a), Theory of the slowly changing component of solar radio emission I, Sov. Astr. AJ 12: 245-253.

28. Zlotnik, E. Ya. (1968b), Theory of the slowly changing component of solar radio emission II, Sov. Astr. AJ 12:464-472.

29. Zheleznyakov, V.V. (1970), Radio Emission from the Sun and Planets, Pergamon, New York.

30. Lang, K.R. (1974a), High resolution interferometry of the sun at 3.7 cm wavelength, Solar Phys. 36:351-367.

31. Felli, M., Pampaloni, P. and Tofani, G. (1974), Fine structure of a very bright active region at a wavelength of 2.8 cm, Solar Phys. 37:395-402.

32. Felli, M., Tofani, G., Fürst, E. and Hirth, W. (1975), On the nature of some active regions in the microwave region, Solar Phys. 42:377-390.

33. Kundu, M.R. and Alissandrakis, C.E. (1975), Observations at 6 cm of the solar active region, Nature 257:465-467.

34. Kundu, M.R., Alissandrakis, C.E., Bregman, J.D. and Hin, A.C. (1978), Six centimeter observations of solar active regions with six arc second resolution, Ap. J. 213:278-295.

35. Alissandrakis, C.E., Kundu, M.R. and Lantos, P. (1981), A model for sunspot associated emission at 6 cm wavelength, Astr. Ap. 82:30-40.

36. Pallavicini, R., Vaiana, G.S., Tofani, G. and Felli, M. (1979), The coronal atmosphere above solar active regions: comparison of high spatial resolution soft X-ray and centimetric observations, Ap. J. 229:375-386.

37. Pallavicini, R., Sakurai, T. and Vaiana, G.S. (1981), X-ray, e.u.v. and centimetric observations of solar active regions: an empirical model for bright radio sources, Astr. Ap. 98:316-327.

38. Lang, K.R. and Willson, R.F. (1979), Very large array observations of solar active regions, Nature 278:24-28.

39. Lang, K.R. and Willson, R.F.(1980), Very large array (V.L.A.) observations of solar active regions", I.A.U. Symposium No. 86: Radio Physics of the Sun, M.R. Kundu and T.E. Gergely, Eds., Reidel, Dordrecht.

40. Lang, K.R. (1974b), Astrophysical Formulae, Springer Verlag, New York.

41. Lang, K.R. (1980), Astrophysical Formulae, 2nd Edition, Springer Verlag, New York.

42. Ginzburg, V.L. (1961), Propagation of Electromagnetic Waves in Plasma, Gordon and Breach, New York.

43. Ginzburg, V.L. (1967), Propagation of Electromagnetic Waves in Plasma, 2nd edition, Gordon and Breach, New York.

44. Krüger, A. (1979), Introduction to Solar Radio Astronomy and Radio Physics, Reidel, Dordrecht.

45. Landini, M., Monsignori Fossi, B.C., Krieger, A. and Vaiana, G.S. (1975), The coronal structure of active regions, Solar Phys. 44:69-82.

46. Vaiana, G.S. (1976), The X-ray corona from Skylab, Phil. Trans. Roy. Soc. London 281:365-374.

47. Vaiana, G.S., Krieger, A.S., Timothy, A.F. and Zombeck, M. (1976), ATM observations, X-ray results, Ap. Space Sci. 39:75-101.

48. Vaiana, G.S. and Rosner, R. (1978), Recent advances in coronal physics, Ann. Rev. Astron. Ap. 16:393-428.

49. Ratcliffe, J.A. (1962), The Magneto-Ionic Theory, Cambridge University Press, Cambridge.

50. Gel'freikh, G.B. and Lubyshev, B.I. (1979), Structure of local sources of the S component of solar radio emission, Sov. Astr. AJ 23:316-322.

51. Kundu, M.R., Schmahl, E.J. and Rao, A.P. (1981), V.L.A. observations of solar active regions at six cm wavelength, Astr. Ap. 94:72-79.

52. Foukal, P.V. (1975), The temperature structure and pressure balance of magnetic loops in active regions, Solar Phys. 43:327-336.

53. Foukal, P.V. (1976), The pressure and energy balance of the cool corona over sunspots, Ap. J. 210:575-581.

54. Foukal, P.V. (1978), Magnetic loops, downflows, and convection in the solar corona, Ap. J. 223:1046-1050.

55. Alissandrakis, C.E. and Kundu, M.R. (1981), Observations of ring structure in a sunspot associated source at six centimeter wavelength, Ap. J. Lett. 253: L49-L51.

56. Bregman, J.D. (1980), Netherlands Foundation for Radio Astronomy Report No. 330, Westerbork.

57. Brombozcz, G. et al. (1981), Report to the Crimean solar maximum year workshop.

58. Sheeley, N.R. (1980), Temporal variations of loop structures in the solar atmosphere, Solar Phys. 66:79-87.

59. Acton, L.W. et al. (1980), The soft X-ray polychromator for the solar maximum mission, Solar Phys. 65:53-71.

60. Akhmedov, S.B., Bogod, V.M. and Gel'freikh, G.B. (1981), The results of a study of local source of active region McMath 15974 on S.M.Y. program using Ratan-600, preprint.

61. Gel'freikh, G.B. et al. (1981), Simultaneous optical and radio observations of a coronal condensation off the limb on November 19, 1980, preprint.

62. Seaton, M.J. (1964), The spectrum of the solar corona, Planetary Space Sci. 12:55-74.

63. Pottasch, S.R. (1964), On the interpretation of the solar ultraviolet emission line spectrum, Space Sci. Rev. 3:816-855.

64. Mewe, R. (1972), Calculated solar X-radiation from 1 to 60 Å, Solar Phys. 22:459-491.

65. Jordan, P. (1969), The ionization equilibrium of elements between carbon and nickel, M.N.R.A.S. 142:501-521.

66. Allen, J.W. and Dupree, A.K. (1969), Calculations of ionization equilibria for oxygen,neon, silicon and iron, Ap. J. 155:27-36.

67. Woolfson, C.J. (1981), Report to the Crimean solar maximum year workshop.

68. Severnyi, A.B. (1966), Magnetic fields at various depths in the solar atmosphere, Sov. Astr. AJ. 10:367-379.

69. Bogod, V.M. and Gel'freikh, G.B. (1980), Measurements of the magnetic field and the gradient of temperature in the solar atmosphere above a flocculus using radio observations, Solar Phys. 67:29-46.

70. Noyes, R.W. (1971), Ultraviolet studies of the solar atmosphere, Ann. Rev. Astr. Ap. 9:209-235.

71. Levine, R.H. and Withbroe, G.L. (1977), Physics of an active region loop system, Solar Phys. 51:83-101.

72. Clark, B.G. (1980), An efficient implementation of the algorith clean, Astr. Ap. 89:377-381.

73. Rosner, R., Tucker, W.H. and Vaiana, G.S. (1978), Dynamics of the quiescent corona, Ap. J. 220:643-665.

74. Velusamy, T. and Kundu, M.R. (1980), Observations of solar active regions at 2 and 6 cm wavelengths with three arc second resolution, I.A.U. Symposium No.86: Radio Physics of the Sun, M.R. Kundu and T.E. Gergely, Eds., Reidel, Dordrecht, pp.105-108.

75. Kundu, M.R. and Velusamy, T. (1980), Observation with the V.L.A. of a stationary loop structure in the sun at six cm wavelength, Ap. J. Lett. 240:L63-L67.

76. Waldmeier, M. (1940), Variation der koronaform, Zs. f. Ap. 20:195-213.

77. Lyot, B. (1944), Le filtre monochromatique polarisant et ses applications en physique solaire, Ann. d'Ap. 7:31-49.

78. Van de Hulst, H.C. (1953), The chromosphere and the corona, The Sun, G.P. Kuiper, Ed., University of Chicago Press, Chicago, pp.203-321.

79. Christiansen, W.N., Warburton, J.A. and Davies, R.D. (1957), The distribution of radio brightness over the solar disk at a wavelength of 20 centimeters, Austr. J. Phys. 10:491-514.

80. Chiuderi-Drago, F., Felli, M. and Tofani, G. (1977), High resolution intensity and polarization structure of the sun at 21 cm, Astr. Ap. 61:79-91.

81. Craig, I.J.D., McClymont, A.N. and Underwood, J.H. (1978), The temperature and density structure of active region coronal loops, Astr. Ap. 70:1-11.

82. Vesecky, J.F., Antiochos, S.K. and Underwood, J.H. (1979), Numerical modeling of quasi-static coronal loops, Ap. J. 233:987-997.

83. Serio, S., Peres, G., Vaiana, G.S., Golub, L. and Rosner, R. (1981), Closed coronal structures II. Generalized hydrostatic model, Ap. J. 243:288-300.

84. Pallavicini, R., Peres, G., Serio, S., Vaiana, G.S., Golub, L. and Rosner, R. (1981), Closed coronal structures III. Comparison of static models with X-ray, e.u.v. and radio observations, Ap. J. 247:692-706.

85. Syrovatskii, S.I. and Kuznetsov, V.D. (1980), On the possibility of radio observations of current sheets on the Sun, I.A.U. Symposium No. 86: Radio Physics of the Sun, M.R. Kundu and T.E. Gergely, Eds., Reidel, Dordrecht.

86. Zheleznyakov, V.V. and Zlotnik, E. Ya. (1980a), Thermal cyclotron radio emission of neutral current sheets in the solar corona, Solar Phys. 68: 317-326.

87. Zheleznyakov, V.V. and Zlotnik, E. Ya. (1980b), Fine structure of microwave solar radio emission from solar activity centers, Sov. Astr. AJ 24:448-454.

88. Zheleznyakov, V.V. and Zlotnik, E. Ya. (1980c), Thermal cyclotron radiation from solar active regions, I.A.U. Symposium No. 86: Radio Physics of the Sun, M.R. Kundu and T. Gergely, Eds., Reidel, Dordrecht.

89. Cheng, C.C. and Widing, K.G. (1975), Spatial distribution of XUV emission in solar flares, Ap. J. 201: 735-739.

90. Widing, K.G. (1975), Fe XXIII 263 Å and Fe XXIV emission in solar flares, Ap. J. Lett. 197: L33-L35.

91. Brueckner, G.E. (1976), ATM observations on the XUV emission from solar flares, Phil. Trans. Roy. Soc. London, A281: 443-459.

92. Moore, R.L. et al. (1978), The thermal X-ray plasma. Big Bear Solar Obs. Rpt. 0180.

93. Kahler, S.W., Krieger, A.S. and Vaiana, G.S. (1975). Morphological evolution of X-ray flare structures from the rise through the decay phase, Ap. J. Lett. 199: L57-L61.

94. Svestka, Z. (1976), Solar flares Dordrecht, Reidel .

95. de Feiter, L.D. and de Jager, C. (1973), Superthermal plasma nodules and their relation to solar flares, Solar Phys. 28: 183-186.

96. Alissandrakis, C.E. and Kundu, M.R. (1978) 6 centimeter observations of solar bursts with 6" resolution, Ap. J. 222: 342-356.

97. Marsh, K.A., Zirin, H. and Hurford, G.J. (1979), VLA observations of solar flares, interpreted with optical, X-ray and other microwave data, Ap. J. 228: 610-615.

98. Frost, K.J. (1969), Rapid fine structure in a burst of hard solar X-rays observed by OSO-5, Ap. J. Lett. 158: L159-L163.

99. Parks, G.K. and Winckler, J.R. (1969) Sixteen-second periodic pulsations observed in the correlated microwave and energetic X-ray emissions from a solar flare, Ap. J. Lett. 155: L117-L120.

100. Janssens, T.J. and White, K.P. (1970), Description of mass motions and brightenings in a class 2b flare, August 8, 1968, Solar Phys. 11: 299-309.

101. van Beek, H.F., deFeiter, L.D. and deJager, C. (1974), Space Research XIV, M.J. Rycroft and R.D. Reasenberg (Eds.) Akademie Verlag , Berlin, p.447.

102. van Beek, H.F., deFeiter, L.D. and deJager, C. (1976), Space Research XVI, M.J. Rycroft (Ed.), Akademie Verlag, Berlin, p. 819.

103. deJager, C. and deJonge, G. (1978), Properties of elementary flare bursts, Solar Phys. 58: 127-137.

104. deJager, C. (1967), The hard solar X-ray burst of 18 September 1963, Solar Phys. 2: 327-346.

105. Vorpahl, J. and Zirin, H. (1970), Identification of the hard X-ray pulse in the flare of September 11-12, 1978, Solar Phys. 11: 285-290.

106. Vorpahl, J. (1972), X-radiation ($E > 10$ KeV), $H\alpha$ and microwave emission during the impulsive phase of solar flares, Solar Phys. 26: 397-413.

107. deJager, C. (1979), On the seats of elementary flare bursts, Solar Phys. 64: 135-141.

108. Young, C.W., Spencer, C.L., Moreton, G.E. and Roberts, J.A. (1961), A preliminary study of the dynamic spectra of solar radio bursts in the frequency range 500-950 Mc/s, Ap. J. 133: 243-257.

109. deGroot, T. (1970) Solar radio spectra between 160 and 320 MHz, Solar Phys. 14: 176-189.

110. Gotwols, B.L. (1972), Quasi-periodic solar radio pulsations at decimetric wavelengths, Solar Phys. 25: 232-236.

111. Kaufman, P. (1976), Fast time structures superimposed to impulsive solar microwave bursts with slowly varying or stationary polarization degree, Solar Phys. 60: 367-381.

112. Elgaroy, O. and Sveen, O.P. (1979),Drifting spikes - a new species of solar radio bursts, Nature 278: 626-627.

113. Cribbens, W., and Matthews, P.A. (1969), Periodic structure in solar radio bursts and its relation to burst energy, Nature 222: 158-159.

114. Maxwell, A. and Fitzwilliam, J. (1973), Microwave pulsations from solar flares, Ap. Letters. 13: 237-242.

115. Cliver, E.W., Hurst, M.D., Wefer, F.L. and Bleiweiss, M.P. (1976), Quasi-periodic burst structure at 28 GHz and its relationship to burst morphological parameters, Solar Phys. 48: 307-320.

116. Marsh, K.A. and Hurford, G.J. (1980), Two-dimensional VLA maps of solar bursts at 15 and 23 GHz with arcsec resolution, Ap. J. Lett. 240: L111-L114.

117. Kundu, M.R., Bobrowsky, M. and Velusamy, T. (1982), VLA observations of positions of 6 centimeter burst peaks associated with hard X-ray burst spikes, Ap. J. 251: 342-351.

118. Kundu, M.R., Schmahl, E., Velusamy, T. and Vlahos, L. (1982), Radio imaging of solar flares using the Very Large Array: new insights into the flare process, Astr. Ap. 108:188-194.

119. Kundu, M.R., Schmahl, E. and Velusamy, T. (1982), Magnetic structure of a flaring region producing impulsive microwave and hard X-ray bursts, Ap. J. 253: 963-974.

120. Kattenberg, A. (1981), Solar radio bursts and their relation to coronal magnetic structures, Ph.D. Thesis, University of Utrecht, The Netherlands.

121. Gold, T. and Hoyle, F. (1960), On the origin of solar flares, M.N.R.A.S. 120: 89-105.

122. Heyvaerts, J., Priest, E.R. and Rust, D.M. (1977), An emerging flux model for the solar flare phenomenon, Ap. J. 216:123-137.

123. Rust, D.M. (1972), Flares and changing magnetic fields, Solar Phys. 25: 141-157.

124. Rust, D.M. (1976), An active role for magnetic fields in solar flares, Solar Phys. 47:21-40.

125. Vlahos, L. and Papadopoulos, K. (1979), Collective plasma effects associated with the continuous injection model of solar flare particle streams, Ap. J. 233:717-726.

126. Emslie, A.G. and Vlahos, L. (1980), Radiation signatures from a locally energized flaring loop, Ap. J. 242:359-373.

127. Petrosian, V. (1982), Structure of the impulsive phase of solar flares from microwave observations, Ap. J. Lett. 255:L85-L89,

128. Holman, G.D., Kundu, M.R. and Papadopoulos, K. (1982), Electron pitch angle scattering and the impulsive phase microwave and hard X-ray emission from solar flares, Ap. J. 257:354-360.

129. Cohen, M.H. (1960), Microwave polarization and coronal magnetic fields, Ap. J. 133:978-1013.

130. Slish, V.I. (1963), Angular size of radio stars, Nature 199:682.

131. Ramaty, R. and Petrosian, V. (1972), Free-free absorption of gyrosynchrotron radiation in solar microwave bursts, Ap. J. 178:241-249.

5. LIST OF INVITED LECTURES RESULTING FROM WORK SUPPORTED BY THIS CONTRACT

1981, June	"Very Large Array Observations of Solar Active Regions", Sterrekundig Instituut, Rijksunivesiteit Utrecht, Fulbright Commission, The Netherlands.
1981, June	"Very Large Array Observations of Solar Active Regions", Netherlands Foundation for Radio Astronomy, Dwingeloo.
1981, October	"Very Large Array Observations of Solar Bursts", Solar Maximum Year Workshop, Annecy, France.
1982, May	"Multiple Wavelength Observations of Flaring Active Regions, Symposium on the Solar Maximum Year, XXIVth COSPAR Meeting, Ottawa, Canada.
1982, July	"Very Large Array Observations of Solar Active Regions, Academy of Sciences, USSR, Leningrad and Moscow.
1982, August	"Radio Wavelength Observations: Structure, Strength, and Variability of Magnetic Fields in the Transition Region and the Solar Corona", International Astronomical Union Symposium No. 102 - Solar and Stellar Magnetic Fields, Zurich, Switzerland.
1982, August	"Multiple Wavelength Observations of Flaring Active Regions", International Astronomical Union Colloquium No. 71 - Activity in Red Dwarf Stars, Catania, Italy.

6. LIST OF PUBLICATIONS RESULTING FROM WORK SUPPORTED BY THIS CONTRACT

"V.L.A. Observations of Solar Active Regions I. The Slowly Varying Component", by Marcello Felli, Kenneth R. Lang and Robert F. Willson, Astrophysical Journal 247, 325-337 (1981).

"V.L.A. Observations of Solar Active Regions II. Solar Bursts", by Kenneth R. Lang, Robert F. Willson and Marcello Felli, Astrophysical Journal 247, 338-347 (1981).

"Multiple Wavelength Observations of a Solar Active Region", by Franca Chiuderi-Drago, Rino Bandiera, Roberto Falciani, Ester Antonucci, Kenneth R. Lang, Robert F. Willson, Kyoto Shibasaki, and Cornelius Slottje, to be published in Solar Physics.

"Very Large Array (V.L.A.) Observations of Solar Active Regions", by Kenneth R. Lang. Proceedings of the Solar Maximum Year Workshop - Crimean Astrophysical Observatory (Moscow: Academy of Sciences of the U.S.S.R., 1982) pp. 39-56.

"Polarized Horseshoes Around Sunspots at 6 Centimeter Wavelength", By Kenneth R. Lang and Robert F. Willson, Astrophysical Journal (Letters), 255, L111-L117 (1982).

"Very Large Array Observations of Coronal Loops at 20 Centimeter Wavelength", by Kenneth R. Lang, Robert F. Willson and Jean Rayrole, Astrophysical Journal 258, 384-387 (1982).

"Very Large Array Observations of Solar Active Regions III. Multiple Wavelength Observations", by Kenneth R. Lang, Robert F. Willson and Victor Gaizauskas, to be published in Astrophysical Journal (1982).

"High Resolution Observations of Solar Bursts at 2 cm, 6 cm and 20 cm Wavelength", by Robert F. Willson, to be published in Solar Physics (1982).

"Multiple Wavelength Observations of Flaring Active Regions", by Kenneth R. Lang, to be published in Proceedings of the XXIV COSPAR Meeting (1982).

"Radio Wavelength Observations, Structure, Strength and Variability of Magnetic Fields in the Transition Region and the Solar Corona", by Kenneth R. Lang, to be published in Solar and Stellar Magnetic Fields: Origin and Coronal Effects, International Astronomical Union Symposium No. 102 (1983).

"Multiple Wavelength Observations of Solar Active Regions", by Kenneth R. Lang, to be published in Activity in Red Dwarf Stars, International Astronomical Union Colloquium No. 71 (1983).

FILME

5-8